OAK RIDGE
NATIONAL LABORATORY

MANAGED BY UT-BATTELLE
FOR THE DEPARTMENT OF ENERGY

ORNL/TM-2009/234

ORNL Quasi-Static Mechanical Characterization and Analysis: FY09 Annual Report to TARDEC

A. A. Wereszczak,* T. P. Kirkland,
K. T. Strong, Jr., and T. J. Holmquist**
Ceramic Science and Technology Group
Materials Science and Technology Division
Oak Ridge National Laboratory
Oak Ridge, TN 37831-6068

* Principal Investigator
wereszczakaa@ornl.gov

** Southwest Research Institute
Minneapolis, MN 55416

Publication Date: December 2009

Prepared by the
OAK RIDGE NATIONAL LABORATORY
Oak Ridge, Tennessee 37831
managed by
UT-BATTELLE, LLC
for the
U.S. DEPARTMENT OF ENERGY
Under contract DE-AC05-00OR22725

UT-BATTELLE

ORNL-27 (4-00)

US ARMY TARDEC
DISTRIBUTION STATEMENT A.
Approved for public release; distribution unlimited.

DOCUMENT AVAILABILITY

Reports produced after January 1, 1996, are generally available free via the U.S. Department of Energy (DOE) Information Bridge:

Web site: http://www.osti.gov/bridge

Reports produced before January 1, 1996, may be purchased by members of the public from the following source:

National Technical Information Service
5285 Port Royal Road
Springfield, VA 22161
Telephone: 703-605-6000 (1-800-553-6847)
TDD: 703-487-4639
Fax: 703-605-6900
E-mail: info@ntis.fedworld.gov
Web site: http://www.ntis.gov/support/ordernowabout.htm

Reports are available to DOE employees, DOE contractors, Energy Technology Data Exchange (ETDE) representatives, and International Nuclear Information System (INIS) representatives from the following source:

Office of Scientific and Technical Information
P.O. Box 62
Oak Ridge, TN 37831
Telephone: 865-576-8401
Fax: 865-576-5728
E-mail: reports@osti.gov
Web site: http://www.osti.gov/contact.html

This report was prepared as an account of work sponsored by an agency of the United States Government. Neither the United States government nor any agency thereof, nor any of their employees, makes any warranty, express or implied, or assumes any legal liability or responsibility for the accuracy, completeness, or usefulness of any information, apparatus, product, or process disclosed, or represents that its use would not infringe privately owned rights. Reference herein to any specific commercial product, process, or service by trade name, trademark, manufacturer, or otherwise, does not necessarily constitute or imply its endorsement, recommendation, or favoring by the United States Government or any agency thereof. The views and opinions of authors expressed herein do not necessarily state or reflect those of the United States Government or any agency thereof.

TABLE OF CONTENTS

TABLE OF CONTENTS
(CONTINUED)

Page

LIST OF FIGURES

LIST OF FIGURES
(Continued)

LIST OF FIGURES
(Continued)

LIST OF FIGURES
(Continued)

Figure **Page**

LIST OF FIGURES
(Continued)

LIST OF FIGURES
(Continued)

LIST OF TABLES

Table **Page**

EXECUTIVE SUMMARY

This report summarizes TARDEC-sponsored work at Oak Ridge National Laboratory (ORNL) during the FY09 involving quasi-static mechanical characterization and analysis. The testing and evaluation of candidate glasses for transparent armor served as a primary goal. Other armor ceramics were evaluated too, in support of the development of innovative test methods, whose use will ultimately help in the improvement of armor ceramics or help in better predicting their ballistic performance.

The following summarizes this report and this year's work:

1. The elastic properties of a spherical indenter affect the forces necessary to initiate fracture in a target ceramics. The lower the elastic modulus of an indenter material, the easier (i.e., lower forces required) it is to initiate fracture. *This implies the fracture initiation of an armor ceramic will depend on the elastic properties of a projectile material, and that this effect, represented by the Dundurs Parameter, can be managed to guide improvement of both armor and projectile materials.*

2. The largest flaws in a population dictate both contact damage and fracture initiations. *This implies the ballistic response of armor ceramics will improve if those large flaws are precluded from appearing in the materials during their processing.*

3. Failure stress dependence on effective area for Hertzian indentation was developed. *Such analysis is adaptable to predict ballistically produced fracture initiation as a function of projectile material and projectile size.*

4. A simple, quick, and inexpensive test method was developed to measure the apparent yield stress of armor ceramics. *This is significant because yield stress is used as input in ballistic models, and yield stress is traditionally measured using (complex, time-consuming, and expensive) shock physics experiments.*

5. Radial confinement increases the necessary indentation forces to initiate fracture and yield-like responses in ceramics. *Ballistic improvement of an armor ceramic will occur if the ceramic can be compressively pre-stressed.*

6. The median crack produced by a Hertzian indent is associated with a dramatic increase in target ceramic compliance. More so than any other produced damage mechanism. *This suggests that a ballistically induced median crack in an armor ceramic may be associated with the dwell penetration event.*

7. Glass exhibits tensile strength that is very much dependent on the amount of material, the side being tested (air versus tin if a float glass), and where it is being tensile stressed (in the middle or near an edge). *The management of these effects will improve ballistic resistance of transparent armor (or any ceramic armor that is undergoing deflection as a consequence of a ballistic impact).*

8. Plasma-arc heat treatment is a quick and relatively inexpensive method to improve the strength of glass. It is implementable into the production line for the mass production of glass. *Increased strain-to-failure and bending deflections are concomitant with increased strength, and therefore, ballistic resistance is improvable using this method.*

9. The Hertzian stress field at high contact stresses is very similar to the stress field from a ballistic impact. *This is significant because the results from Hertzian indentation measurements have the prospect of being used as input in ballistic models to predict dwell conditions.*

10. The understanding of glass densification and fragmentation behaviors are aided by piezo-Raman spectroscopy and quasi-static, high-energy fracture. *Continued refinement of these test methods will improve the understanding of glass impact resistance.*

11. In addition to glass, strength-size scaling was evident in SiC and B_4C. *Previously proposed strength dependencies on rate from shock experiments may instead be explained by this strength-size scaling effect.*

12. The quantification of strength-size scaling in armor ceramics clearly shows there is no single strength value that can be used to describe that ceramic. *A ballistic modeler can therefore use more appropriate failure stress value(s) as input to predict deflection and expanding cavity responses in the ceramic target.*

These follow-on efforts are recommended based on the above statements:

- Dynamic Hertzian indentation using a dynamic hardness tester
- Quantify flaw population size in strategic armor ceramics
- Refine and increase robustness of apparent yield stress measurement
- Quantify fracture and yield processed in armor ceramics as a function of confined stress
- Develop test method to accurately measure stress condition of median crack formation
- Measure strength-size scaling in glass ceramic candidates for transparent armor
- Refine plasma-arc heat treating to maximize strengthening of glasses and glass ceramics
- Refine ballistic modeling analysis to improve adaptability of Hertzian indentation results
- Refine densification and fragmentation test methods and interpretations
- Predict ballistically-induced armor deflection and expanding cavity performance using strength-size scaling results

INTRODUCTION

TARDEC sponsored quasi-static mechanical characterization and analysis work at ORNL in FY09, and this report summarizes those efforts and results. Seven sections are used to group the efforts performed, and they are: Hertzian indention and contact damage, glass strength characterization, glass surface modification using plasma-arc heating, threshold pressure modeling, phase changes in glass, crush fragmentation of glass, and a last section that supports the primary findings with additional, related studies.

1. HERTZIAN INDENTATION AND CONTACT DAMAGE

1.1. Basis for Inquiry

Hertzian or spherical indentation of brittle materials can be a useful way to test for contact-induced fracture initiation. This is important because it includes armor ceramics, and the improved understanding will enable improved armor ceramics.

Understanding the conditions that cause this damage mechanism is important in many brittle material applications (e.g., bearings, armor, dental, etc.). Ring crack initiation is the first fracture mechanism that occurs during a Hertzian contact fracture event provided the material is responding linear elastically [1.1]. Ring cracking is caused by the radial tensile stress that builds on the edge of the circular contact area between the indenter and target material. During Hertzian loading the spherical indenter contacts the flat target surface causing displacements of the surfaces to occur radially inward. This causes a region of compression to build in the center of the contact circle surrounded by a region of radial tension - the latter promotes ring crack initiation if the tensile stress is sufficiently large.

An electromechanical test frame was used for the Hertzian indentation ring crack initiation testing. An acoustic emission (AE) sensor was used to identify the acoustic event of ring crack initiation and its associated force (RCIF) during indentation. An illustration of the test setup is shown in Fig. 1.1. The AE sensor's signal was consistently the most sensitive to acoustic activity when it was mounted on the surface of the target material. In preliminary testing, a threshold of 40 dB was found to be sufficiently high to eliminate background noise yet low enough to reliably detect the initiation of a ring crack. Indents were examined in an optical microscope with differential interference contrast (DIC or Nomarski) imaging to confirm that a detected acoustic event was actually the initiation of a ring crack. Ultraviolet optical microscopy with a dye penetrant was performed when optically hard to see ring cracks were present.

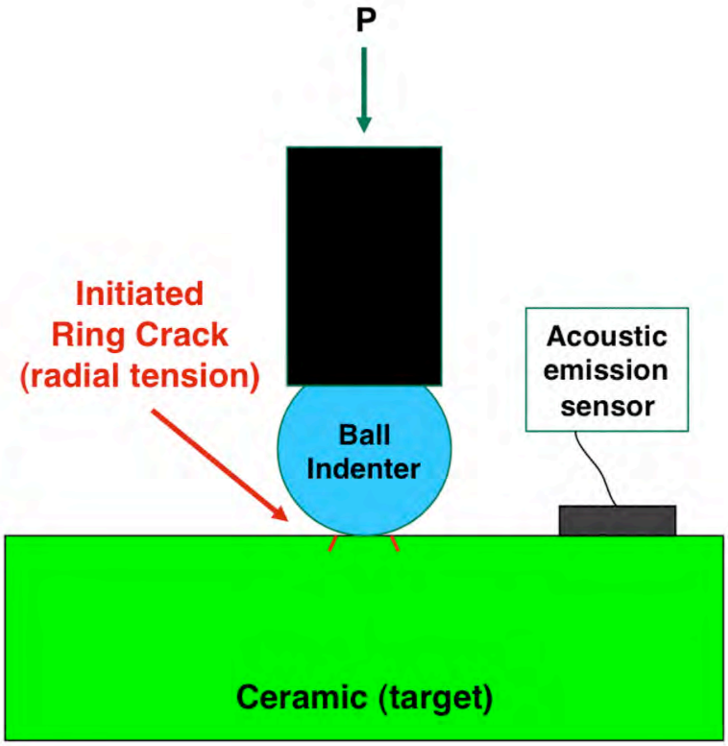

Figure 1.1. Schematic drawing of the ring crack initiation test configuration. An acoustic emission sensor was used to detect an acoustic event that was then linked to the ring crack initiation force.

Considering a frictionless case between the indenter and target material (i.e., their surfaces exhibit only mutual slip), the radial stress where ring cracking initiates can be calculated (i.e. strength of the brittle material) using the classical Hertzian equation

$$\sigma_{rad-\max} = \frac{1-2\nu}{2}\frac{P_F}{\pi a^2} \quad , \tag{1.1}$$

where P_F is the ring crack initiation force and ν is Poisson's ratio of the target material. Eq. 1.1 is illustrated in Fig. 1.2. The parameter a is the contact radius given by

$$a = \left(\frac{4}{3}\frac{kPR}{E_T}\right)^{1/3} \quad , \tag{1.2}$$

where R is the sphere radius, P is the applied compressive force, E_T is the target elastic modulus, and

$$k = \frac{9}{16}\left[\left(1-\nu_T^{\,2}\right)+\left(1-\nu_i^{\,2}\right)\frac{E_T}{E_i}\right] \quad , \tag{1.3}$$

where ν is Poisson's ratio and the subscripts T and i represent the target and indenter, respectively [1.2].

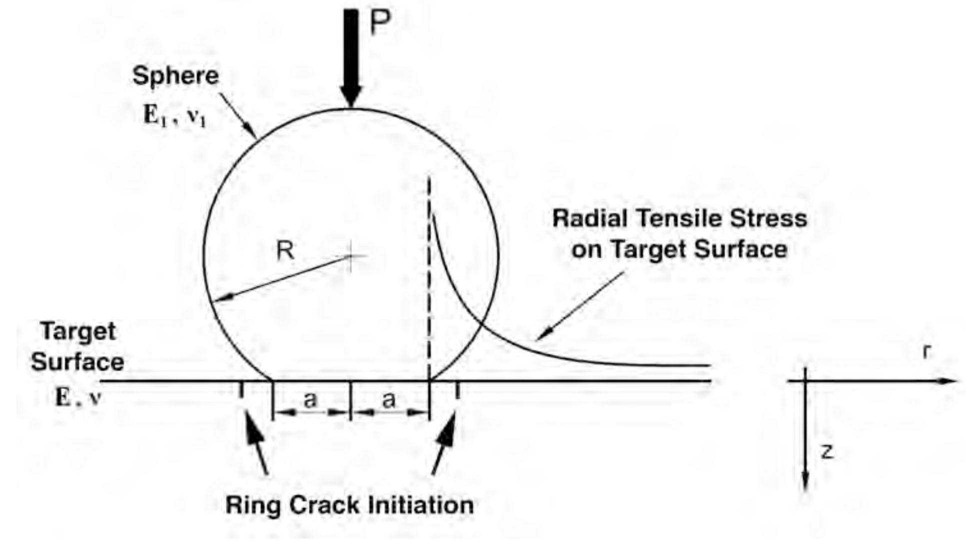

Figure 1.2. Frictionless radial tensile stress profile of Hertzian contact.

The classical Hertzian equation assumes a frictionless contact surface exists between the indenter and target material. However, friction indeed is present whenever there is a mismatch in elastic properties between the indenter and target materials (i.e., whenever they are different materials). Traction will occur on the target's surface and it will act radially outward when it is more compliant and radially inward when it is more rigid in comparison to the indenter material.

A convenient way to examine the relative differences of the stiffness or compliance of the target or indenter is through the use of the Dundurs Parameter (β)

$$\beta = \frac{(1-2\nu_T)/G_T - (1-2\nu_i)/G_i}{2((1-\nu_T)/G_T + (1-\nu_i)/G_i)} \quad , \tag{1.4}$$

where G is the shear modulus [1.3]. Values of the Dundurs parameter fall into one of three domains as shown in Fig. 1.3. A positive, zero, and negative β represent the case when the indenter is stiffer, has the same stiffness, or is less stiff than the target material, respectively. In all cases considered, the target material is assumed to be isotropic and homogeneous. As will be seen, the ring cracking response of the target material is dependent on the elastic properties of the indenter, so for meaningful interpretation of ring crack initiation, the role that the indenter properties play should always be accounted for.

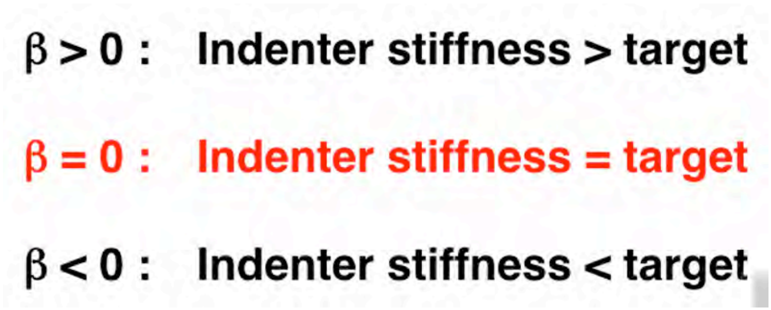

$\beta > 0$: Indenter stiffness > target

$\beta = 0$: Indenter stiffness = target

$\beta < 0$: Indenter stiffness < target

Figure 1.3. The three cases of the Dundurs parameter and Hertzian indentation.

The mismatch effect on ring cracking was experimentally shown on glass materials by Johnson [1.4]. If the coefficient of friction was known, then the tensile stress of ring crack initiation could be calculated. Warren proposed that, during indentation when the spherical indenter contacts the target surface, the materials initially adhere to each other causing an area of stick in the center of the contact circle. An annular area of slip then surrounds this area of stick. If these areas can be measured then it is theorized that the coefficient of friction can be calculated and thus so can the strength of the material [1.5]. The measurement of the coefficient was not examined during this investigation but will be considered in future work.

For all Hertzian ring crack initiation testing, a displacement rate of 0.1 μm/s was used to press the spherical indenter against the target specimen until initiation of a ring crack was detected. The indenter was then rapidly unloaded. At least 20 indents were conducted for each target – indenter material combination. Commercial statistical software was used to fit the RCIFs to a two-parameter Weibull distribution using maximum likelihood estimation.

A set of indenters with a range of elastic properties was chosen to test for, and observe, the mismatch effect between the indenter and target materials [1.6]. The specific diameters were chosen to ideally produce the same contact areas between the indenter and target material based on their respective elastic properties. Si_3N_4 was designated as a reference material and a diameter of 3.00 mm was chosen as a reference size. The remaining indenter sizes were chosen with respect to the Si_3N_4 ball according to Eqs. 1.5-1.6

$$R_1\left[\frac{1-\nu_1}{G_1}+\frac{1-\nu_{TAR}}{G_{TAR}}\right]=R_2\left[\frac{1-\nu_2}{G_2}+\frac{1-\nu_{TAR}}{G_{TAR}}\right] \tag{1.5}$$

or

$$\frac{R_2}{R_1}=\frac{\dfrac{1-\nu_1}{G_1}+\dfrac{1-\nu_T}{G_T}}{\dfrac{1-\nu_2}{G_2}+\dfrac{1-\nu_T}{G_T}}\quad , \tag{1.6}$$

where R is indenter radius, ν is Poisson's ratio, G is shear modulus (or $G=E/2(1+\nu)$), and the subscripts 1, 2, and TAR correspond to indenter ball material 1, indenter ball material 2, and the target material, respectively. Target properties used are listed in Table 1.1. The rationale behind this normalization method and Eqs. 1.5-1.6 is the use of balls of dissimilar materials, adhering to the ratio of R_2/R_1, will produce the same contact area for the same applied compressive force, and in turn will produce the same maximum radial tensile stress, and the same average axial contact stress. This is important because it enables confident comparison between ring crack initiations generated by balls made from dissimilar materials. Namely, *the target material should ring crack at the same applied compressive force with ball materials of those two radii if there is sustained frictionless Hertzian contact and if both the indenter and target materials remain linearly elastic up to that force.*

1.2. Ring Cracking and Indenter/Target Property Mismatch; Comparison When Target is SiC, Si_3N_4, or Glass

The target materials chosen for testing were a hot-pressed silicon carbide (SiC), a hot-pressed silicon nitride (Si_3N_4) and a borosilicate glass. Each material's respective elastic properties are displayed in Table 1.1. It should be noted that the size of the Hertzian contact areas in comparison to the grain sizes of the materials is large; therefore, these measurements sample a bulk material response. Like the ball indenter materials, the target materials were chosen for this study because their elastic moduli spanned a wide range of values.

Table 1.1. Elastic properties of the SiC, Si_3N_4, and glass target materials.

Target Material	**Elastic Modulus -E- (GPa)**	**Shear Modulus -G- (GPa)**	**Poisson's Ratio -ν-**
SiC	451	192	0.170
Si_3N_4	318	125	0.273
Borosilicate	62	96	0.199

The indenter materials used for the ring crack testing, with their respective sizes and elastic properties (which closely adhere to Eq. 1.6), are displayed in Fig. 1.4.

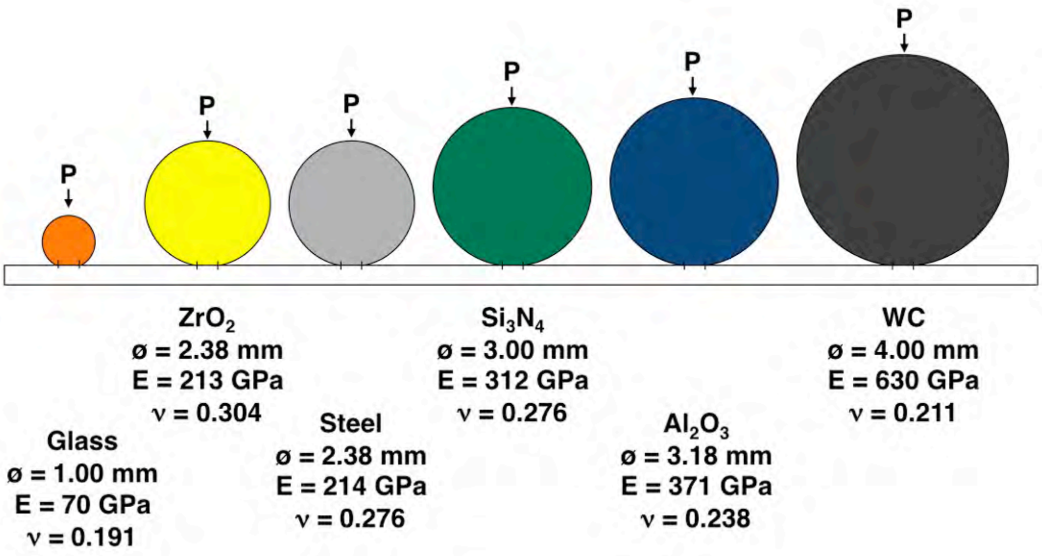

Figure 1.4. Schematic drawing showing the indenter materials and diameters used for testing [1.6] described in Section 1.2.

The results showed friction was operative in this testing because of the elastic mismatch between indenter and target materials. The characteristic RCIFs are plotted as a function of the indenter elastic modulus and Dundurs Parameter β in Figs. 1.5 and 1.6, respectively. The drawn trend lines are fitted to the balls that remain linear elastic throughout testing. The RCIF increases as the indenter modulus and Dundurs Parameter increases. This is due to friction. The forces that initiate ring cracking should be the same for all ball materials if the classical Hertzian theory were obeyed; namely, the fitted curves in Figs. 1.5 and 1.6 should be horizontal if there were no friction.

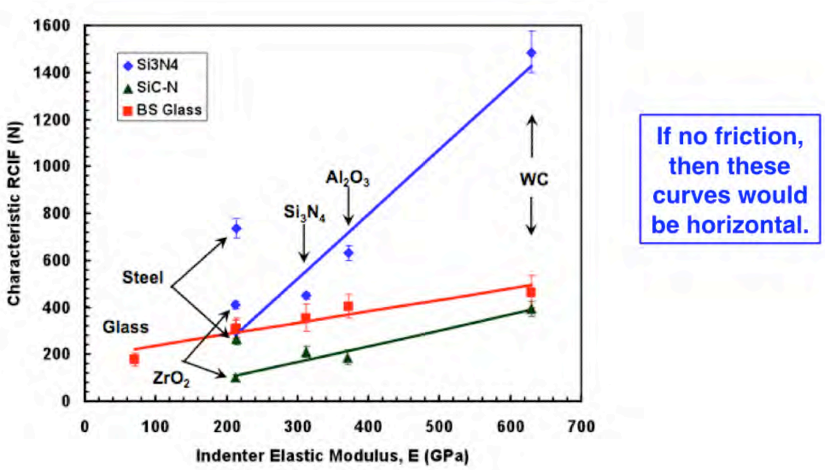

Figure 1.5. Characteristic ring crack initiation force in Si_3N_4, SiC, and borosilicate glass as a function of indenter elastic modulus.

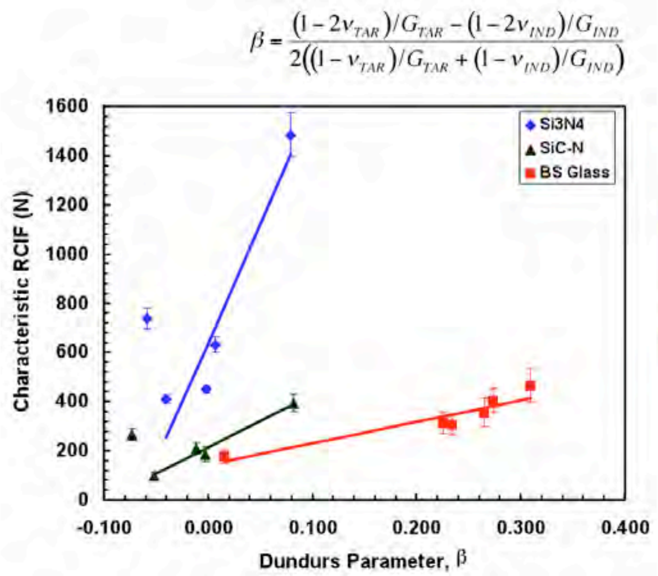

$$\beta = \frac{(1-2\nu_{TAR})/G_{TAR} - (1-2\nu_{IND})/G_{IND}}{2\left((1-\nu_{TAR})/G_{TAR} + (1-\nu_{IND})/G_{IND}\right)}$$

If no friction, then these curves would be horizontal.

Figure 1.6. Characteristic ring crack initiation force in Si_3N_4, SiC, and borosilicate glass as a function of Dundurs parameter.

The data points for the steel indenters against the SiC and Si_3N_4 target materials do not fall on the linear trends drawn in Figs. 1.5 and 1.6. This is due to the steel ball yielding during indentation whereas the other balls remained linear elastic. However, it overlaps the ZrO_2 indenter data on the borosilicate glass target, which could be expected since ZrO_2 and steel have similar elastic properties. Finite element analysis (FEA) was conducted for the case of the steel indenter on all three target materials at the characteristic RCIF. A linear elastic case was considered and the maximum von Mises stress was determined in the steel ball. For the case of the Si_3N_4 and SiC, the von Mises stress in the steel ball was 2x and 3x larger than that of the yield stress of the steel ball material (2.03 GPa). The borosilicate glass caused a maximum von Mises stress in the steel ball only slightly above that of its yield stress. The Hertzian indentation with steel balls creates extra complications in the target ring crack initiation analysis because of its potential to yield (and its consequential change in radius of curvature).

The Si_3N_4-indenter on Si_3N_4-target and glass-indenter on glass-target test cases are special cases because their elastic properties are matched. For only this case, the contact surfaces are believed to exhibit only slip, or the classical Hertzian case [1.4]. From Figs. 1.5 and 1.6, when the indenter material is more rigid than the target material, higher RCIFs result. Whereas lower RCIFs result when then indenter is more compliant.

The observed elastic mismatch effect on RCIFs is due to the effect of friction on the radial tensile stress on the target material's surface. Maximum radial tensile stress decreases as the indenter elastic modulus increases as Johnson and Warren showed [1.4-1.5]. For more rigid indenters, higher forces are necessary to raise the tensile stress to a value where ring cracking occurs, alternatively for a more compliant indenter, lower forces are necessary.

Summarizing Section 1.2

Characteristic RCIFs of a hot-pressed SiC, a hot-pressed Si_3N_4, and a borosilicate glass were measured using different indenter materials and specially chosen diameters. The results showed that an elastic mismatch effect between the indenter and target material was operative, and consequential frictional forces affected the radial tensile stresses that in turn affected the forces of ring crack initiation. With respect to any target material tested, a more rigid indenter caused higher RCIF whereas a more compliant indenter lowered it.

1.3. Ring Cracking Response of Two Microstructurally Different SiCs

Interest existed in the subtask to examine ring-crack-dependence on indenter elastic modulus in two hot-pressed SiCs having equivalent elastic properties but different failure-stress-limiting flaw populations. Confident comparisons of ring crack initiation responses were sought by conducting numerous tests per condition to produce statistical significance. Lastly, by using several different ball materials, a desire existed to identify one that works efficiently with SiC owing to the limitation that SiC balls are not commercially available.

Two hot-pressed SiCs, designated as SiC-N and SiC-HPN by their manufacturer (BAE Systems, Advanced Ceramics Division, Vista, CA), were evaluated in this study. A comparison of their measured properties is shown in Table 1.2 [1.7]. The densities and fracture toughnesses of the two SiCs were equivalent whereas the SiC-N had a slightly larger elastic modulus and Poisson's ratio but a lower Knoop hardness at 1 kg (9.8 N).

Table 1.2. Material properties of the SiC-N and SiC-HPN. ± values are one standard deviation.

SiC Grade	Density (g/cm^3)	Elastic Modulus (GPa)	Poisson's Ratio	Fracture Toughness ($MPa\sqrt{m}$)	Knoop Hardness at 9.8 N (GPa)
SiC-N	3.21 ± 0.01	454 ± 4	0.171 ± 0.012	4.49 ± 0.12	19.4 ± 0.4
SiC-HPN	3.19 ± 0.03	443 ± 1	0.155 ± 0.003	4.45 ± 0.03	21.3 ± 0.4

Cylinders of each material, 20 mm in diameter by 20 mm in length, were sectioned into 3-mm-thick disks, their flats ground parallel, and then one side polished to a 1-μm finish for the Hertzian ring crack initiation force measurements. All disks of both SiCs were polished at the same time.

Grain size distributions were quantified with both SiCs using image analysis of scanning electronic microscopy (SEM) images of polished surfaces. Examples of the microstructures of the two SiCs are shown in Fig. 1.7. Resulting cumulative percent finer than curves are shown in Fig. 1.8 and show that SiC-HPN has a finer microstructure. Approximately 20% of the grains in SiC-N are larger than the largest grains in SiC-HPN. The observation of the larger grain sizes in the SiC-N is important because it is later discussed to explain the observed differences in ring crack initiation between the two SiCs.

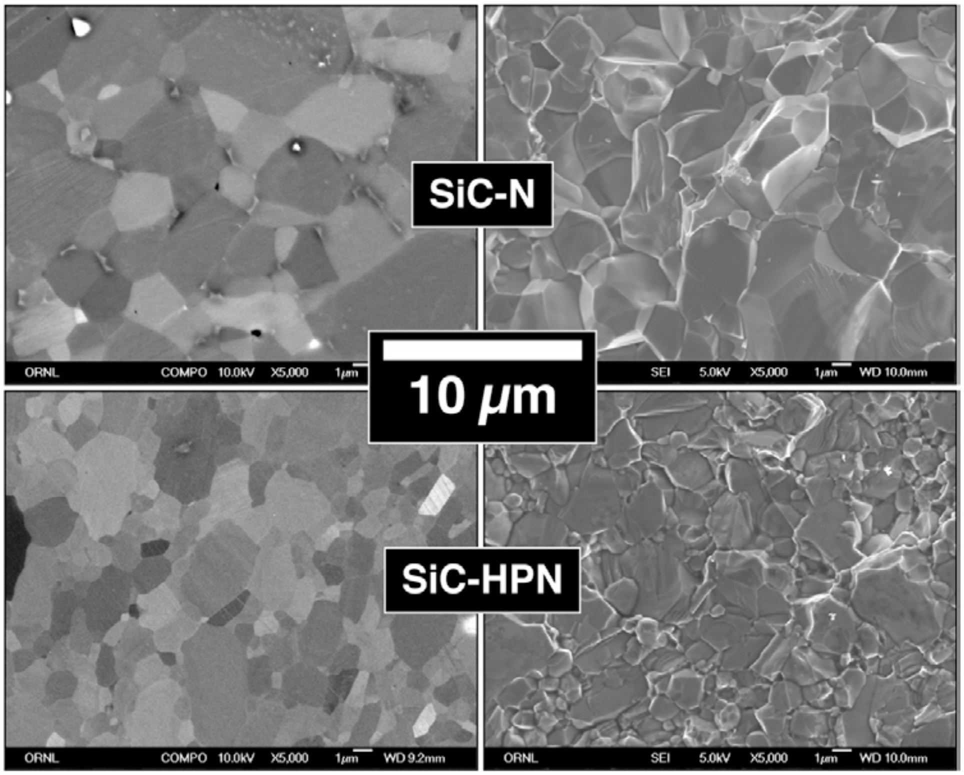

Figure 1.7. Scanning electron microscope images of microstructures on companion polished (left) and fracture (right) surfaces of SiC-N and SiC-HPN.

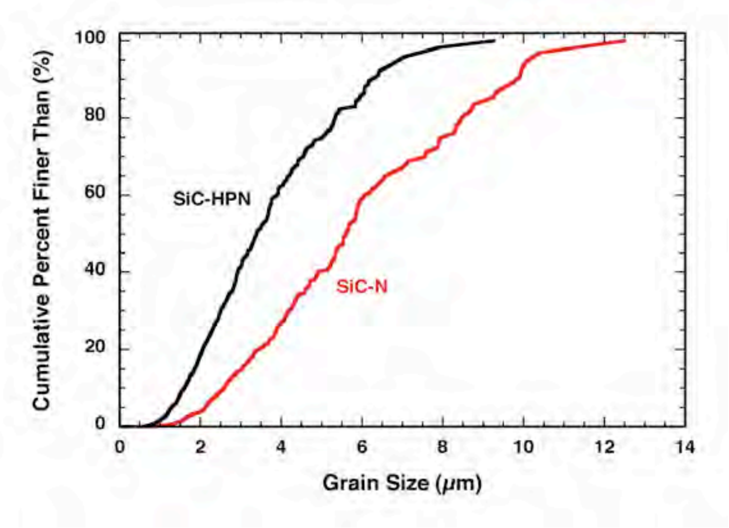

Figure 1.8. Grain size distributions of SiC-N and SiC-HPN. 335 and 846 grains comprise the measured distributions for SiC-N and SiC-HPN. Both cover an area of approximately 2800 μm^2. Approximately 20% of the SiC-N is comprised of grains larger than SiC-HPN's largest grains.

Balls were chosen whose material elastic moduli spanned a wide range, and that were either stiffer ($E_{IND} > E_{TAR}$) or more compliant ($E_{IND} < E_{TAR}$) than the target SiC materials ($E_{TAR} \sim 450$ GPa), and that were commercially available in a variety of diameters. Zirconium oxide or zirconia (ZrO_2), steel, silicon nitride (Si_3N_4), aluminum oxide or alumina (Al_2O_3), and tungsten carbide (WC) balls were selected. Properties are given in Table 1.3 and their relative diameters are illustrated in Fig. 1.9.

Table 1.3. Elastic properties of ball indenters, the idealized ball diameter, and the actual ball diameters used.

Ball Material	**Elastic Modulus - *E* - (GPa)**	**Poisson's Ratio - *ν* –**	**Shear Modulus - *G* - (GPa)**	**Ideal Ball Dia. - *2R* - (mm)**	**Used Ball Dia. - *2R* - (mm)**	**Dundurs Parameter* - *β* - (unitless)**
ZrO_2	213	0.276	82	2.39	2.38	-0.074
Steel	214	0.304	84	2.37	2.38	-0.053
Si_3N_4	312	0.276	122	3.00	3.00	-0.011
Al_2O_3	371	0.238	150	3.27	3.18	-0.003
Hot-Pressed SiC (Flat Target)	*450*	*0.170*	*192*	*3.56*		*0.000*
WC - 8%Co	629	0.211	260	4.18	4.00	+0.082
Diamond	1141	0.07	530	5.07		+0.150

* Calculated using Eq. 1.6 for the "used ball diameter" against hot-pressed SiC.

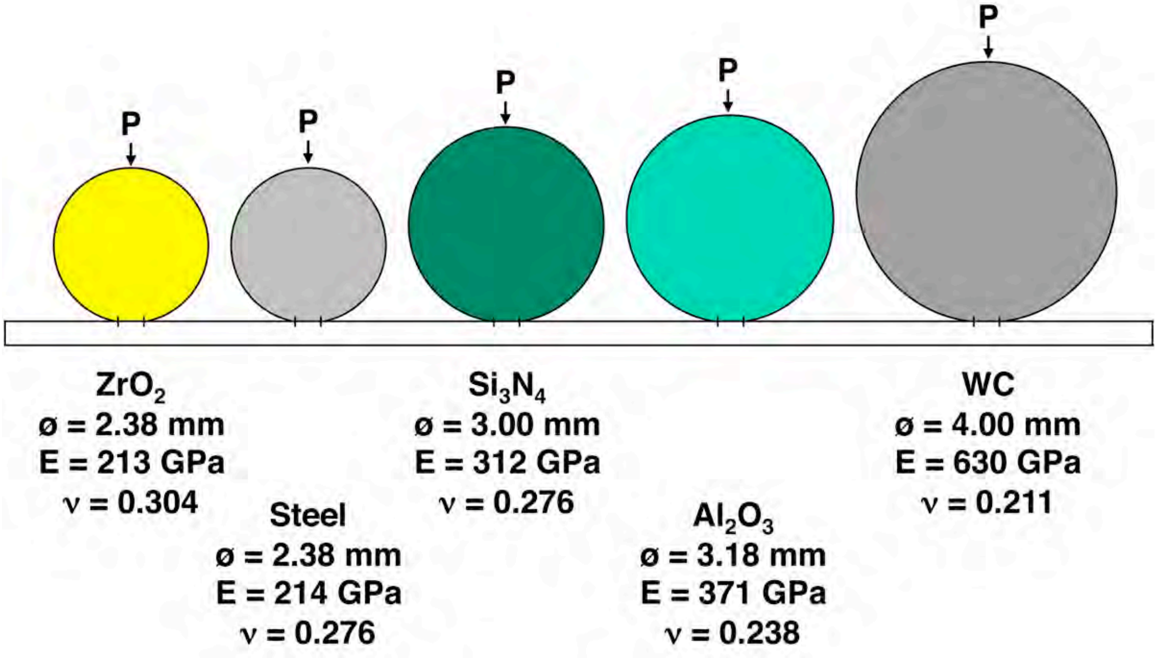

Figure 1.9. Schematic drawing showing the contrast of the indenter materials and (scaled) diameters used against a SiC target (E ~ 450 GPa and a ν ~ 0.17). With these, approximately the same contact area, average contact pressure, and maximum radial tensile stress are produced in the SiC for the same compressive force (P).

Decreasing the indenter elastic modulus consistently resulted in lower ring crack initiation forces for both SiCs. Their decreases are statistically significant. The portrayal of this is shown in Figs. 1.10-1.11 as a function of indenter elastic modulus, and Dundurs parameter, respectively. Using the Dundurs parameter with the measured RCIF is a thorough way to represent the elastic response of indentation as it represents two (i.e., shear modulus and Poisson's ratio according to Eq. 1.6) of the three elastic properties (elastic modulus being the third) of both the indenter and target, whereas the use of indenter elastic modulus or indenter shear modulus by themselves do not portray the elastic response of the target. However it still remains convenient to portray RCIF as a function of indenter elastic modulus too, as the significance of the *E* is familiar to most (unlike the Dundurs parameter).

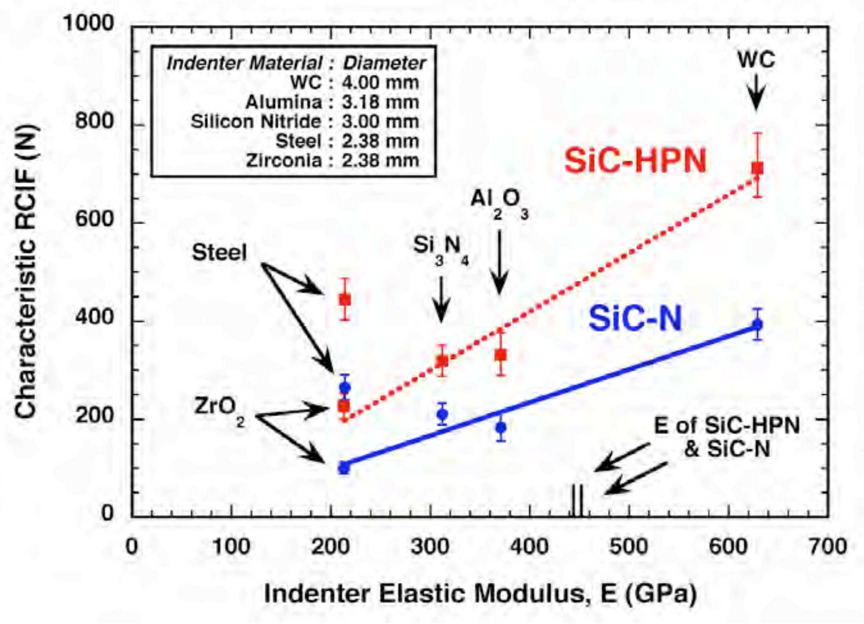

Figure 1.10. Average ring crack initiation force (RCIF) as a function of indenter elastic modulus. Vertical bars represent ± 95% confidence bands.

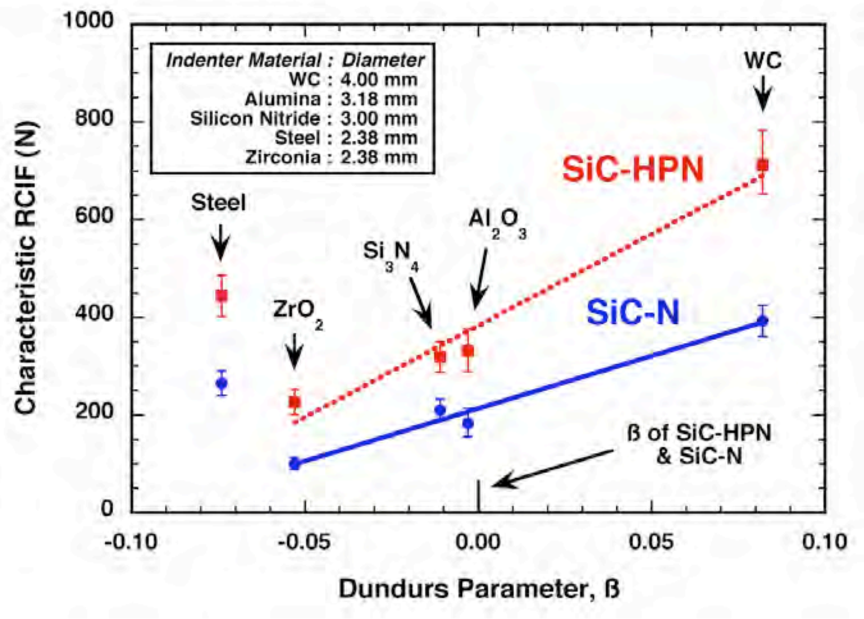

Figure 1.11. Average ring crack initiation force (RCIF) as a function of Dundurs Parameter. Vertical bars represent ± 95% confidence bands. $\beta < 0$ represents the case where an indenter material is more compliant than the target material, $\beta = 0$ for when indenter and target material properties are matched, and $\beta > 0$ represents the case of a stiffer indenter.

The steel balls yielded during ring crack initiation testing so the RCIF results they produced are interpreted differently than those produced with the ZrO_2, Si_3N_4, Al_2O_3, and WC balls (which sustained linear elasticity). This is why the RCIFs produced by the steel are so dissimilar from those produced by the ZrO_2 even though their elastic moduli are equivalent. The steel and ZrO_2 differences are most pronounced upon consideration of the Dundurs parameter as shown in Fig. 1.11. Finite element analysis was conducted for the case of the steel indenter against SiC-HPN (i.e., the SiC with the higher RCIF). A linear elastic model of the Hertzian contact was constructed and the maximum von Mises stress was estimated in the steel ball. The maximum equivalent stress was approximately three times larger than the yield stress (~ 2.0 GPa) of the steel ball material. Therefore, Hertzian indentation with steel balls created extra complications in the target ring crack initiation analysis of these SiCs because it yielded and produced a consequential unknown change in radius of curvature therefore consideration for the remaining analysis was dismissed. Consequently, the linear regressed fits shown in Figs. 1.10-1.11 are only for the RCIF data generated with the ZrO_2, Si_3N_4, Al_2O_3, and WC balls.

The state of the target material's microstructure also affects RCIF. Though the RCIF for both SiCs decreased with decreasing indenter elastic modulus (or Dundurs parameter), the RCIF for the SiC-N consistently occurred at lower forces with any indenter as shown in Figs. 1.10-1.11. SiC-HPN's RCIF superiority over SiC-N's was observed in another study involving three (1.0, 1.6, and 2.5 mm) diameter diamond indenters [1.7], so SiC-HPN's superiority in the present study is consistent with other Hertzian RCIF testing.

This difference in RCIF for the same indenter E or β means that differences in the microstructures (i.e., failure-stress-limiting flaw size) of the two SiCs affects RCIF because the two SiCs have equivalent elastic moduli (~ 450 GPa).

To better interpret the relationship between microstructure and ring crack initiation, the RCIF results were used to estimate ring crack initiation failure stresses. Such stresses are in the form of radial tensile stresses located on the target surface just (radially) beyond the Hertzian contact area (or radius). The study of the relationship between (tensile) failure stress and microstructural scale (or size) conveniently enables an interpretation involving Griffith theory.

Accurately estimating a ring crack initiation failure stress with confidence is not trivial. The classical Hertzian expression to relate ring crack initiation force to a maximum radial tensile stress, though a simple expression, is based on the assumption that zero friction (i.e., complete slip only) exists at the contact interface. However, friction was non-zero in Hertzian testing as shown in Figs. 1.10-1.11. Therefore, using this study's RCIF in the classical Hertzian expression to estimate a ring crack initiation failure stress could produce misleading or incorrect results, but one would not know how misleading or incorrect the results are because the coefficient of friction value is an unknown.

This issue can be circumvented or managed by considering the different maximum radial tensile stresses at the two extremes of friction (i.e., zero and infinite friction). The actual (unknown) coefficient of friction obviously must be between those two bounds, and in turn, its associated maximum radial tensile stress must be between the tensile stresses of those two friction bounds. As will be shown, those bounds are attractively very narrow when the elastic properties of the indenter and target material are similar, and the estimation of a ring crack initiation failure stress can be made accurately and with confidence.

For the frictionless bound, the relationship between Hertzian contact force, indenter size, elastic properties of the indenter and target, and the resulting contact radius was shown in Eq. 1.1.

For the infinite friction (complete stick or stiction) bound, whenever there is a mismatch in elastic properties between the indenter and target materials (i.e., $\beta \neq 0$), traction will occur on the target's surface and it will act radially outward when it is more compliant than the indenter and radially inward when it is more rigid [1.4]. The radial stress profile for infinite friction ($\sigma_{rad\text{-}max,\mu=\infty}$) at the force of ring crack initiation is represented by

$$\sigma_{rad-\max,\mu=\infty} = -\left(\frac{4\beta P_F}{3\pi}\right)\left[(2+\nu_{TAR})\left(\rho-\sqrt{\rho^2-1}\right)+\frac{(1-\nu_{TAR})\sin^{-1}\left(\frac{1}{\rho}\right)-\left(\rho^2-1\right)}{\rho^2}\right] \tag{1.7}$$

where ρ is r/a, and r is radial position for $r \geq 1$.

When the target material is more compliant than the indenter material (e.g., WC spherical indenter on SiC), β is positive and the radial stress is compressive for all radial positions beyond the contact radius. The sum of the radial tension is thereby reduced and its maximum value occurs at progressively greater radii as β increases. This has been shown elsewhere [1.4-1.5]. Additionally, Warren and Hills [1.5] also showed a stiffer indenter acts to suppress Mode I cracking so the influence of Mode II loading becomes more important. This effect is represented by the sum of the classical Hertzian and no-slip stresses in Fig. 1.12. Conversely, when the target surface is stiffer (e.g., Si_3N_4 spherical indenter on SiC), the radial tensile stress is tensile and adds to the maximum radial tension at $\rho = 1$ as shown in Fig. 1.13. The actual friction coefficient will obviously be greater than zero (frictionless) and less than infinity (no-slip), so the actual radial stress profile will be between the classical Hertzian Theory and Net Radial Stress curves in Figs. 1.12-1.13. The total contact area comprises the sum of a central contact area experiencing complete stick plus an annular region surrounding that circle that is experiencing slip [1.8-1.9].

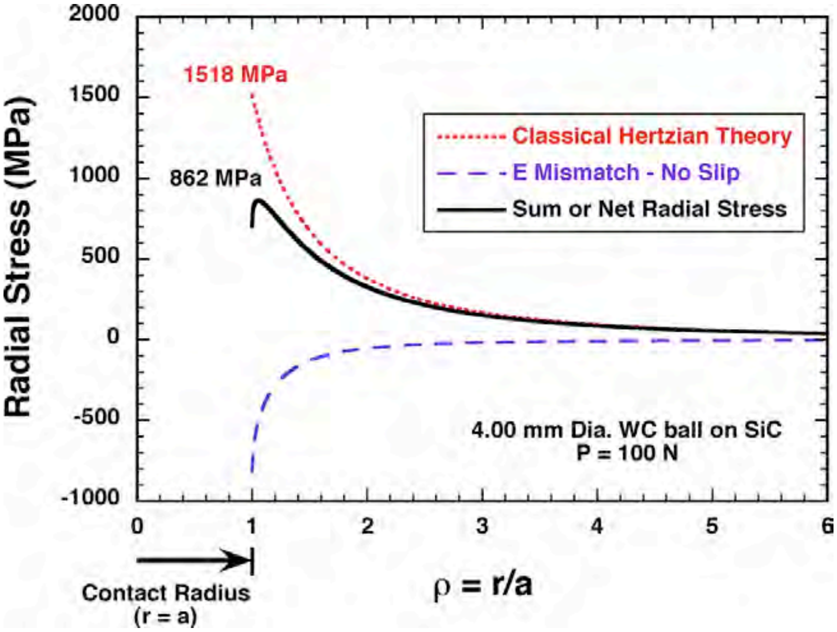

Figure 1.12. Comparisons of radial stress fields for classical Hertzian theory and net radial stress for no-slip contact for β greater than zero (WC indenter on SiC target).

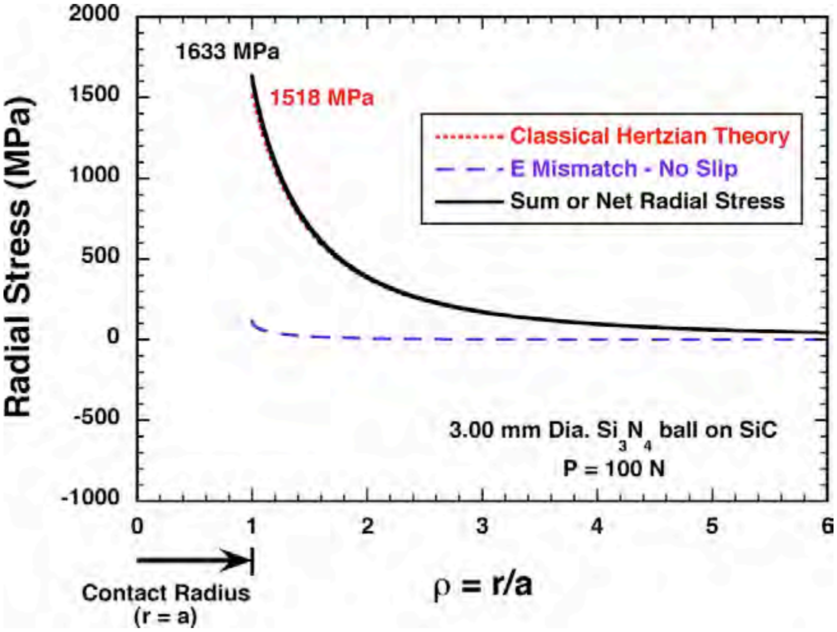

Figure 1.13. Comparisons of radial stress fields for classical Hertzian theory and net radial stress for no-slip contact for β less than zero (Si_3N_4 indenter on SiC target).

The net radial stress profiles for various indenter materials in contact with a SiC target under a no-slip condition are shown in Fig. 1.14. Maximum radial tensile stress decreases as the indenter elastic modulus increases as Johnson [1.4] and Warren [1.5] have previously showed. The experimental results shown in Fig. 1.10-1.11 are consistent with this trend illustrated in Fig. 1.14; namely, as the indenter elastic modulus increases, the net radial stress in the target SiC decreases, so a higher compressive force is necessary to reach some critical failure stress in the SiC.

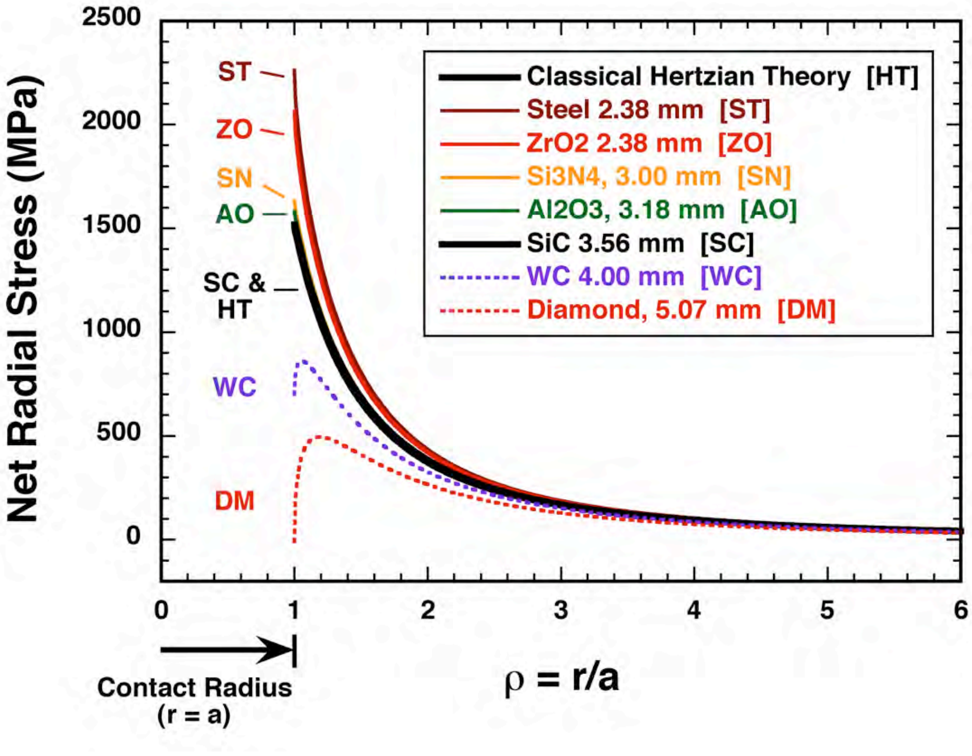

Figure 1.14. Comparison of radial stress profiles for different indenter materials in 100-N-contact with SiC under conditions of infinite friction (or no-slip or stiction). Shown diameters and force generate the same net radial tensile stress for a frictionless or "HT" condition.

The determinations of the bounding maximum radial tensile stresses for frictionless and infinite friction conditions are useful because they enable interpretations about choosing an appropriate indenter material, strength-size-scaling of the target material, and the relationship between stress and flaw size in the target material. A two-parameter Weibull characteristic radial-tensile-failure-stress and modulus were determined for both bounds. In turn, the effective area bounds for both zero and infinite friction were estimated using methods described in Section 1.4. The resulting relationships between characteristic failure stress and effective area for the two SiCs and for all coefficients of friction are shown in Fig. 1.15. 95% confidence ratio rings are shown for each of the eight indenter-material-target-SiC combinations.

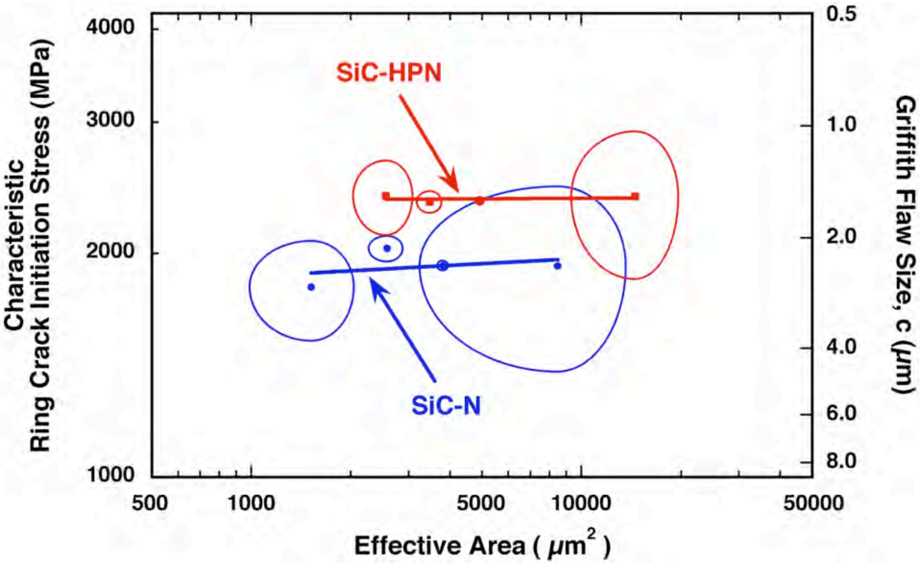

Figure 1.15. The ring-crack-initiation failure stress is higher for SiC-HPN than SiC-N. 95% confidence ratio rings shown for, left to right, ZrO_2, Si_3N_4, Al_2O_3, and WC ball indenters against both SiCs. Greater confidence in the estimation of ring crack initiation failure stress results when the indenter material has similar elastic properties to those of the target material; namely Al_2O_3 balls pressed against SiC in this case. The nearly horizontal lines are representative of no significant size scaling of ring crack initiation failure stress for the shown range of effective area.

Using an indenter material whose elastic modulus is similar to that of the target results in very narrow confidence bands and produces estimations of ring crack initiation stresses that have accuracy and confidence. The 95% confidence ratio ring for the Al_2O_3 indenter used with both the SiC-N and SiC-HPN is very small indicating that the failure stress is insensitive to the coefficient of friction because the elastic properties of the Al_2O_3 are not too dissimilar to that of the target SiCs. The 95% confidence bands grow in size as the elastic properties get more dissimilar, particularly when the indenter is stiffer or when $\beta > 0$. The confidence ratio ring for the WC balls are quite large and their elastic modulus is about 40% greater than that for SiC while the bounds for the ZrO_2 (while still relatively large) are smaller and its elastic modulus is about 50% lower than that of SiC. WC balls are a common choice for Hertzian indentation in the literature, and the herein described results show that that choice of WC can produce a large uncertainty, and that uncertainty of ring crack initiation stress only gets worse as the difference between the target material and WC elastic moduli becomes larger. The use of WC balls to characterize ring crack initiation stress in a WC target would produce very confident estimates of ring crack initiation stress whereas the confidence in that stress estimation would be poor if, for example, WC balls were used to characterize ring crack initiation behavior in glass (E ~ 70 GPa).

There is little or no failure-stress size scaling between 1500-15000 µm^2 as evidenced by the horizontal nature of both lines for both SiCs shown in Fig. 1.15. The regressed fits of both those lines actually produce a high-valued negative Weibull modulus that can be interpreted to physically mean there is no size scaling in failure stress in this range of effective areas. This means that the strength-limiting flaw size that limits ring crack initiation failure stress in both these SiCs is quite narrow *in this effective area range*, and that narrow strength-limiting flaw size in the SiC-HPN is smaller because its ring crack initiation failure stresses are consistently larger.

There are larger grains in the SiC-N than in the SiC-HPN, larger grains in both material's grain-size-distributions could act as Griffith flaws, so a lower failure stress of ring crack initiation should occur in the SiC-N than in SiC-HPN as a consequence. As was shown in Fig. 1.8, approximately 20% of the grains in SiC-N's microstructure are larger than the largest grains (~ 9 µm) in SiC-HPN's. Both materials had equivalent fracture toughnesses (K_{Ic} ~ 4.45 MPa√m, see Table 1.2). If one assumes a crack correction factor (Y) of 1.5, then Griffith flaws sizes can be estimated using the failure stress values shown in Fig. 1.15 according to $\sigma = K_{Ic} \bullet Y^{-1} \bullet c^{-1/2}$. Those sizes are plotted in Fig. 1.15 on the right-hand axis. The Griffith flaw size range in Fig. 1.15 is similar to the grain size distributions shown for both SiCs in Fig. 1.8. The largest grains in SiC-N were approximately 13 µm whereas they were approximately 9 µm in SiC-HPN. For SiC-HPN, the maximum stress is ~ 1400 MPa for a flaw size of 4.5 microns (grain size = 2c = 9 µm), and the maximum stress is ~ 1151 MPa for SiC-N for a flaw size of 6.5 microns (grain size = 13 µm). The estimated failure stress from those largest flaws illustrated in Fig. 1.8 shows that that stress for SiC-N is about 80-85% that of SiC-HPN. Comparing the characteristic stresses in Fig. 8 reveals that SiC-N is about 80% that of SiC-HPN. Therefore, it is believed that the larger grains in SiC-N are associated with it consistently having a lower failure stress (and ring crack initiation force) for any choice of indenter.

Summarizing Section 1.3

- Ring cracking in hot-pressed SiC initiated at lower Hertzian indentation forces as the elastic modulus of a spherical indenter decreased. This occurred due to friction. While the coefficient of friction was an unknown and may be experimentally intractable, the determination and interpretation of the ring crack initiation stress can still occur through the simple consideration of frictionless (complete slip) and infinite (complete stick or stiction) friction bounding conditions. Ring crack initiation consistently occurred at lower forces on the SiC having coarser microstructure independent of the test indenter material.

- Simpler interpretation and estimation of ring crack initiation stresses with greater fidelity and usefulness will be outcomes if the selected spherical indenter material has the same or similar elastic modulus as that of the target or material. Such "elastic property matching" serves to circumvent the complexities that a ubiquitously unknown coefficient of friction introduces in the estimation of Hertzian ring crack initiation stress.

1.4. Ring Cracking and Effective Area Analysis

The understanding of spherical or Hertzian contact-induced fracture initiation is important to the development of improved engineered ceramics for applications involving contact, wear, abrasives, rolling contact, and impact. Controlled Hertzian indentation conducted in the laboratory can be used to assess such contact damage and compare performances of candidate ceramics. Unlike indentation that uses pyramidal-shaped indenters (e.g., Knoop, Vickers, Berkovich, cube-corner), an advantage of Hertzian indentation is the target ceramic material first responds linear elastically before permanent contact damage (cracking or yielding) ever begins. This enables the estimation of a maximum radial tensile stress at the compressive force that causes ring crack initiation.[1]

The effective area is an important parameter used in several applications. It is necessary for computing the Weibull scale parameter that is used to determine the reliability of structural ceramics when surface-type flaws are the strength-limiter. Additionally, the effective area (A_e) is used to scale the strength of one component to that of another (made from the same material) and failing from the same flaw type [1.10-1.11]:

$$\left(\frac{\sigma_{f1}}{\sigma_{f2}}\right) = \left(\frac{A_{e2}}{A_{e1}}\right)^{1/m} \tag{1.8}$$

where σ_{f1} and σ_{f2} are the mean or characteristic strengths for arbitrary components 1 and 2, A_{e1} and A_{e2} are the effective areas for these two components, and m is the Weibull modulus. The effective area for a given component can be thought of as the equivalent area of a tensile specimen subjected to uniform stress equal to the maximum stress in the component resulting in the same probability of failure. In other words, a component with surface area A is equivalent to a tensile specimen with surface area A_e [1.11].

Strength-scaling using Eq. 1.8 involves an inherent assumption that crack propagation initiates at the tip of a critically loaded flaw in an isotropic and homogeneous material. Depending on the material microstructure, the highly stressed annular region due to Hertzian loading could be small enough to traverse a finite number of grains, in turn causing crystallographic anisotropy to dictate the fracture behavior. The effective area analysis introduced in this work does not take anisotropy into account and assume the fracture to be unaffected by the microstructure of the material.

Under Hertzian indentation, the maximum tensile stresses occur at the surface within an annular region outside the contact zone. Therefore effective area, rather than effective volume, expressions are of focus here because surface-type or surface-located flaws cause Hertzian ring crack fracture initiation when subjected to peak stresses.

---

[1] Ring crack initiation occurs at lower compressive forces than yield initiation with relatively large diameter indenters. Yielding initiates at lower compressive forces than ring cracking with relatively small indenters. The analysis performed in this study only pertains to the former case.

Friction affects the maximum radial tensile stress during Hertzian contact. The coefficient of friction in Hertzian indentation is complex[2], likely intractable, is not known *a priori*, and may not even be constant throughout the loading history.

Therefore, the objective was to derive the effective area expression for a target material under spherical Hertzian indentation for the two extreme or bounding cases (which enables circumventing the problem of not knowing the coefficient of friction):

1) Classic Hertzian indentation with no friction where complete slip occurs, and
2) All slip prevented, or complete stiction, or where infinite friction exists.

A schematic diagram for the Hertzian indentation test is shown in Fig. 1.16. The derived effective area (A_e) will be that at the surface of the target material where z = 0.

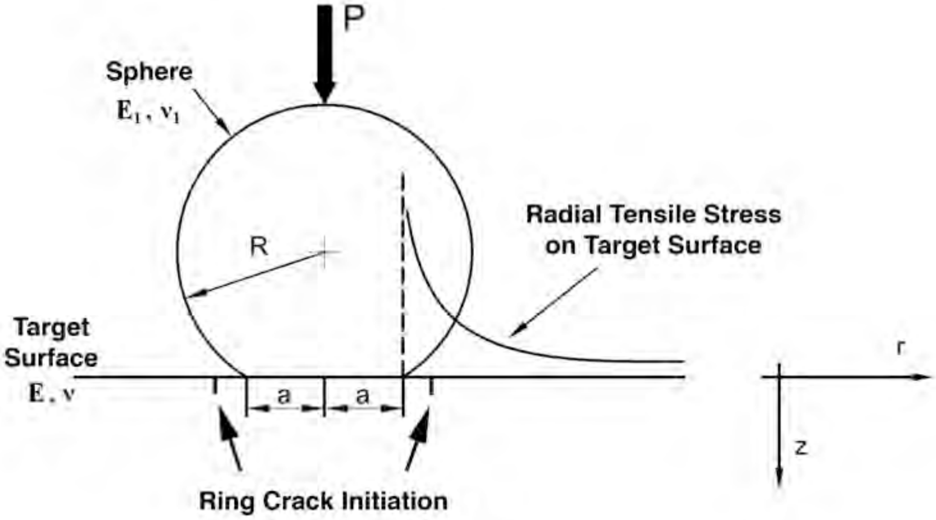

Figure 1.16. Schematic diagram for Hertzian indentation and ring crack initiation. P is applied compressive force, E and ν are Young's modulus and Poisson's ratio, R is sphere radius, a is contact radius, r is radial position on the target surface, and z is axial position into the target's bulk.

The A_e corresponds to the region where tensile stresses occur at the surface. This region only exists outside the contact area. Hence, the A_e is derived for the following conditions:

$$r \geq a \quad \text{and} \quad z = 0 \tag{1.9}$$

---

[2] Friction in this effective area analysis is considered to *only* be due to elastic property mismatch between spherical indenter and flat target material. Other contributing factors (e.g., those due to surface roughness) are not considered.

where a is the radius of the Hertzian contact circle. The principal stress distributions (σ_1 and σ_3) at the surface and outside the contact zone are given by [1.12-1.13]:

$$\sigma_1 = \sigma_r = \frac{P(1-2\nu)}{2\pi r^2}, \text{ and} \tag{1.10}$$

$$\sigma_3 = \sigma_\theta = -\sigma_r \quad . \tag{1.11}$$

The second principal stress is zero ($\sigma_2 = 0$). The effective area for this biaxial stress state is

$$A_e = \int \left[\left(\frac{\sigma_1}{\sigma_{1,\max}} \right)^m + \left(\frac{\sigma_3}{\sigma_{3,\max}} \right)^m \right] dA \quad , \tag{1.12}$$

where $dA = r\,dr\,d\theta$. Since σ_3 is compressive, it drops out of Eq. 1.11 and becomes

$$A_e = \int \left(\frac{\sigma_1}{\sigma_{1,\max}} \right)^m rdrd\theta \quad . \tag{1.13}$$

From Eq. 1.10, $\sigma_{1,\max}$ occurs at $r = a$. Hence,

$$\sigma_{1,\max} = \frac{P(1-2\nu)}{2\pi a^2} \quad \text{, and} \tag{1.14}$$

$$\frac{\sigma_1}{\sigma_{1,\max}} = \frac{a^2}{r^2} \quad . \tag{1.15}$$

Substituting Eq. 1.15 into Eq. 1.13 we obtain

$$A_e = \int_a^\infty \int_0^{2\pi} \left(\frac{a}{r} \right)^{2m} rdrd\theta \quad , \tag{1.16}$$

where $a^3 = 4kPR/3E$ = constant, R is the indenter radius, P the compressive force, E the elastic modulus, $k = (9/16)\,[(1-\nu^2) + (1-\nu_1^2)\,E/E_1]$, ν is Poisson's ratio, and subscript 1 corresponds to the indenter material (see Fig 1.16).

Integrating and solving Eq. 1.16,

$$A_e = a^{2m} \int_a^\infty \int_0^{2\pi} \frac{1}{r^{2m-1}}\, drd\theta \quad \text{, and} \tag{1.17}$$

$$A_e = 2\pi a^{2m} \int_a^\infty r^{1-2m}\, dr \quad \text{, and} \tag{1.18}$$

$$A_e = \frac{2\pi a^{2m}}{2-2m} r^{2-2m} |_a^\infty \quad \text{, and} \tag{1.19}$$

$$A_e = \frac{\pi a^{2m}}{1-m} r^{2(1-m)} |_a^\infty \quad \text{, and} \tag{1.20}$$

$$A_e = \frac{\pi a^{2m}}{1-m} \left[0 - a^{2(1-m)}\right] \quad . \tag{1.21}$$

Simplifying yields the following expression for the classic (frictionless) Hertzian effective area:

$$A_e = \frac{\pi a^2}{m-1} \quad . \tag{1.22}$$

The effective area is therefore a function of the Weibull modulus *and* any of the above parameters that affect the size of the contact radius *a*.

In cases where the spherical indenter and target materials have different elastic properties, frictional forces are likely to develop at the contact interface resulting in a modified Hertzian stress distribution. Johnson *et.al.*, [1.4] studied this effect theoretically and experimentally. They determined when the indenter is more rigid than the target surface the material appears stronger (i.e., withstands higher compressive forces), while a less rigid indenter has the opposite effect.

The classic, frictionless, Hertzian theory predicts radial ring cracking to initiate at the edge of the contact zone between the indenter and material surface, corresponding to the maximum radial stress location. When the indenter has a lower elastic modulus than the target material and friction is non-zero, the maximum radial tensile stress is still at this location, but has a higher magnitude. However, when the indenter material has a higher elastic modulus than the target material and friction is non-zero, the existence of friction alters the stress distribution and causes the location of the maximum radial tensile stress to move radially outward from the Hertzian contact circle. This is illustrated in Fig. 1.17. Johnson *et. al.* [1.4], Warren and Hills [1.5], and Section 1.2 showed this experimentally.

Johnson *et al.*, [1.4] modified the Hertzian radial stress distribution by adding a radial stress term that develops due to friction

$$\sigma_r = (\sigma_r)_p + (\sigma_r)_q \tag{1.23}$$

where $(\sigma_r)_p$ is the classic Hertzian radial stress component (Eq. 1.10), and $(\sigma_r)_q$ is the radial stress component due to friction. $(\sigma_r)_p$ and $(\sigma_r)_q$ can be written in terms of the maximum contact pressure, p_0, as

$$(\sigma_r)_p = \frac{(1-2\nu)p_0 a^2}{3r^2} \quad \text{, and} \tag{1.24}$$

$$(\sigma_r)_q = -\left(\frac{2}{3\pi}\right)\kappa p_0\left[(2+\nu)\left(\rho-(\rho^2-1)^{1/2}\right)+\left((1-\nu)\sin^{-1}\left(\frac{1}{\rho}\right)-(\rho^2-1)^{1/2}\right)/\rho^2\right] \quad , \tag{1.25}$$

and

$$\kappa = \frac{\left[(1-2\nu)/G\right]-\left[(1-2\nu_1)/G_1\right]}{\left[(1-\nu)/G\right]+\left[(1-\nu_1)/G_1\right]} \quad , \tag{1.26}$$

where $p_0 = 3P/(2\pi a^2)$, G is the shear modulus, and $\rho = r/a$. The parameter κ is a measure of dissimilarity of elastic constants between the indenter and the target materials. When the target material is more compliant than the indenter ($\kappa > 0$), the frictional radial stress $(\sigma_r)_q$ is compressive. This in turn decreases the radial tensile stress, and its maximum value shifts further away from the contact edge as κ increases [1.4]. Conversely, when the target material is more rigid ($\kappa < 0$), the frictional radial stress is tensile and adds to the classic Hertzian radial stress at $\rho = 1$.

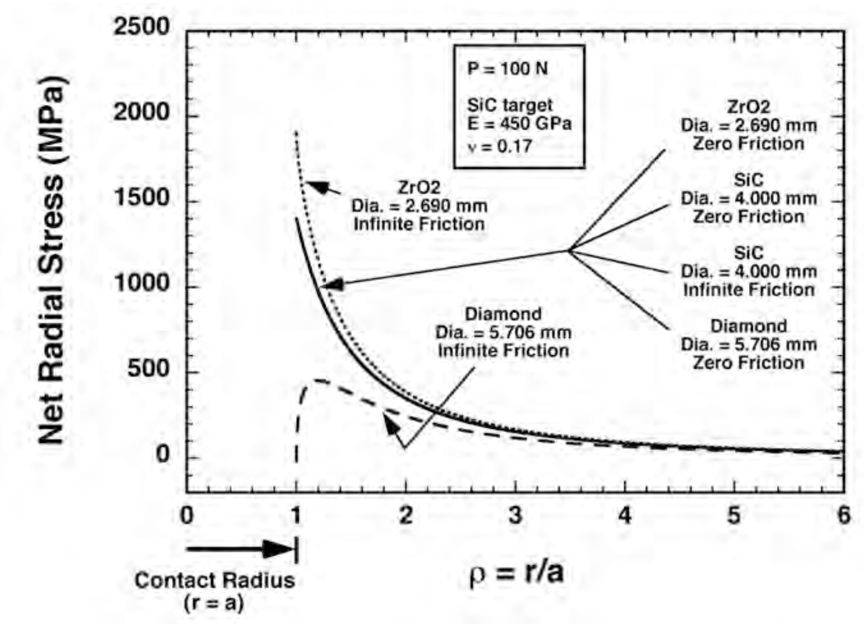

Figure 1.17. Net radial tensile stress as a function of radial position, indenter material, and friction condition against a SiC target for a Hertzian compressive force of 100 N. For no friction (Eq. 1.14), the specific shown diameters of the ZrO_2, SiC, and diamond indenters produce the same stress profile. However, for the infinite friction or complete stiction condition (Eq. 1.23), the ZrO_2 indenter causes the highest tensile stress and the diamond indenter the lowest.

The radial stress distribution per Eq. 1.23 is rather complicated and does not lend itself to deriving a closed form solution for the effective area term. Hence, numerical integration becomes necessary to evaluate the effective area for this case

$$A_e = \int \left(\frac{\sigma_r}{\sigma_{r,\max}} \right)^m rdrd\theta \tag{1.27}$$

where σ_r is Eq. 1.23, and $\sigma_{r,\max}$ corresponds to its maximum value that must be computed *a priori* by evaluating the maxima in this function.

The effective areas for the classic Hertzian frictionless and the infinite friction conditions for three different cases are compared in Figs. 1.18-1.20, and come from the stress profiles shown in Fig. 1.17. The cases are (1) target stiffer than the indenter ($\kappa < 0$), (2) indenter and target having the same stiffness ($\kappa = 0$), and (3) indenter stiffer than the target ($\kappa > 0$). The relative diameter sizes for each indenter material were chosen after Johnson *et. al.*, [1.4] where the same applied compressive force using their sizes produces the same average contact stress and the same maximum radial stress in the contact material (for the frictionless case).

The effective areas as a function of Weibull modulus for Case 1 is shown in Fig. 1.18 where a (more compliant) zirconia indenter is pressed against a SiC target. Here the frictional radial stress is tensile and adds to the classic Hertzian stress, leading to reduced effective area compared to that for the classic frictionless case. The difference in effective areas would increase as the difference in the indenter and target material elastic moduli increases. For example, the difference in frictionless and infinite friction effective areas would be greater than that of the herein described Case 1 if a zirconia indenter were to instead spherically indent tungsten carbide ($E \sim 630$ GPa, $\nu = 0.2$).

For the unique situation of Case 2, Fig. 1.19 shows that when the materials comprising an indenter and target are the same (SiC against SiC in this example), the infinite friction and frictionless cases produce equal effective areas.

The effective areas for Case 3 are compared in Fig. 1.20 where a (stiffer) diamond indenter is pressed against a SiC target. In this case the frictional radial stress is compressive and modifies the classic Hertzian stress distribution, leading to increased effective area compared to that for the classic frictionless case. The difference in effective areas would increase as the difference in the indenter and target material elastic moduli increases. For example, the difference in frictionless and infinite friction effective areas would be greater than that of the herein described Case 3 if a diamond indenter were used to instead spherically indent glass ($E \sim 70$ GPa, $\nu = 0.2$).

Perfect matching between the closed form solution of Eq. 1.22 and the numerical integration solution of Eq. 1.13 as a function of Weibull modulus are displayed in Figs. 1.18-1.20. This validates the derived expression of Eq. 1.22.

There are at least two advantages for determining the effective areas for both zero and infinite coefficients of friction. The first is they provide bounds to the effective area for any actual non-zero coefficient of friction. And second, even if the coefficient of friction is unknown or even very complex, that is not a problem because one knows that the effective area must be within the effective area bounds for the extreme cases of zero and infinite coefficients of friction.

The most dramatic effect among the three cases was Case 3 involving the stiffer indenter. The effective area for the infinite friction condition could be up to an order of magnitude greater than that for the frictionless classic Hertzian case as shown in Fig. 1.20. This difference would significantly skew Weibull strength-scaling if not taken into account. For example, using a Weibull modulus of 10 in Eq. 1.8 predicts the frictionless classic Hertzian ring crack initiation stress to be 20% higher than that for the case of infinite friction.

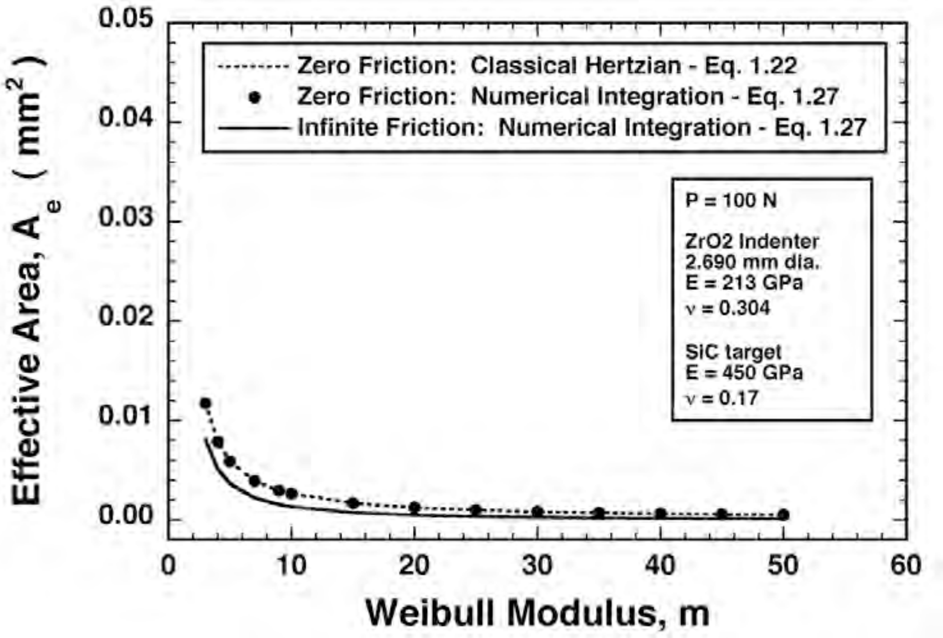

Figure 1.18. Target stiffer than indenter (κ < 0) or Case 1. Comparison between closed form solution for classic Hertzian effective area expression (Eq. 1.22), numerical integration for classic Hertzian effective area, and Hertzian effective area with infinite friction.

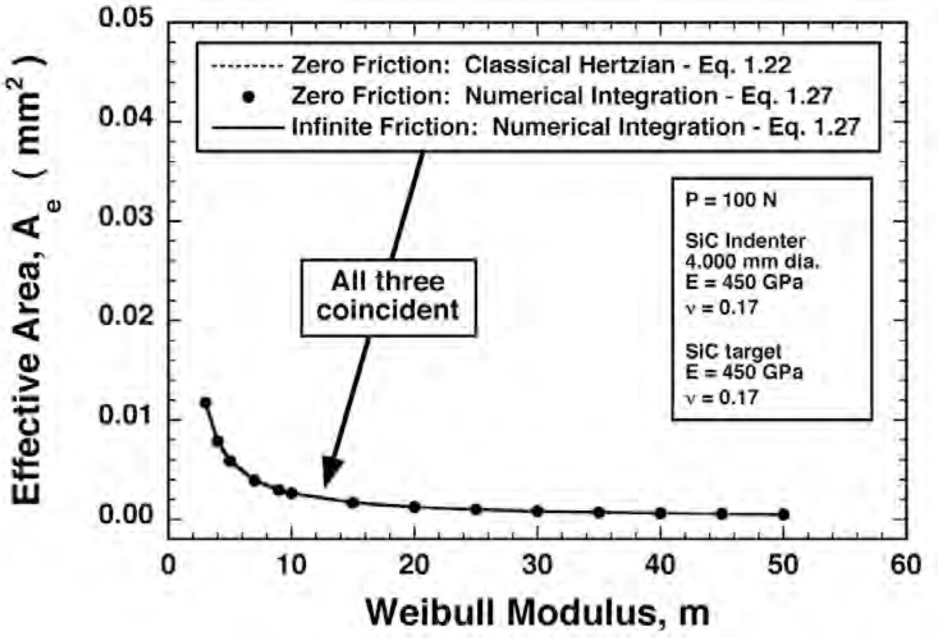

Figure 1.19. Indenter and target have same stiffness (κ = 0) or Case 2. Comparison between closed form solution for classic Hertzian effective area expression (Eq. 1.22), numerical integration for classic Hertzian effective area, and Hertzian effective area with infinite friction.

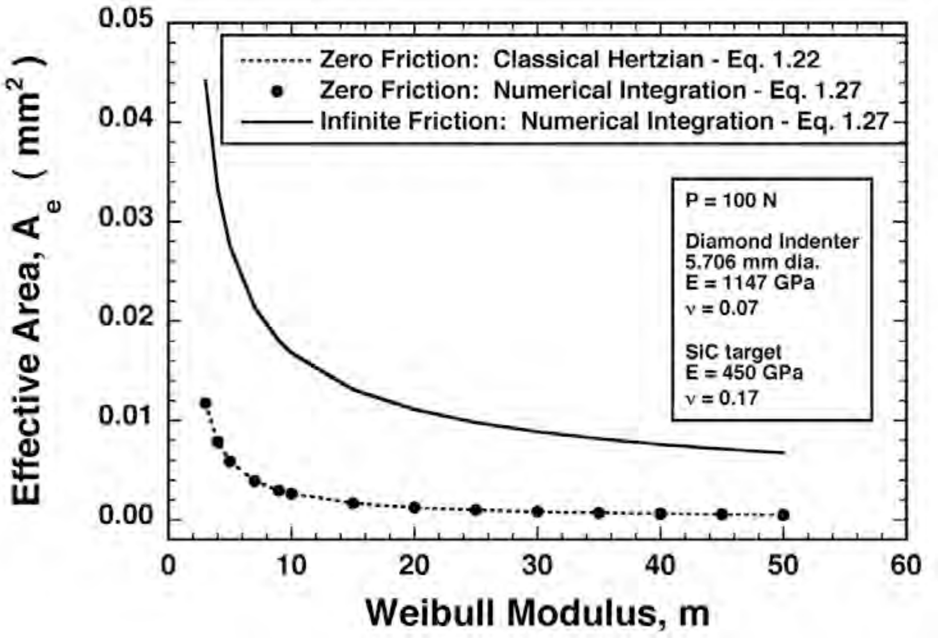

Figure 1.20. Indenter stiffer than target (κ > 0) or Case 3. Comparison between closed form solution for classic Hertzian effective area expression (Eq. 1.22), numerical integration for classic Hertzian effective area (Eq. 1.27), and Hertzian effective area with infinite friction.

As a last examination of the effective analysis, Hertzian ring crack initiation was performed when the ball and target materials were equivalent. Silicon nitride on silicon nitride was used. Six different ball diameters were used and they are illustrated in Fig. 1.21. The intent was to examine ring cracking in the absence of elastic property mismatch.

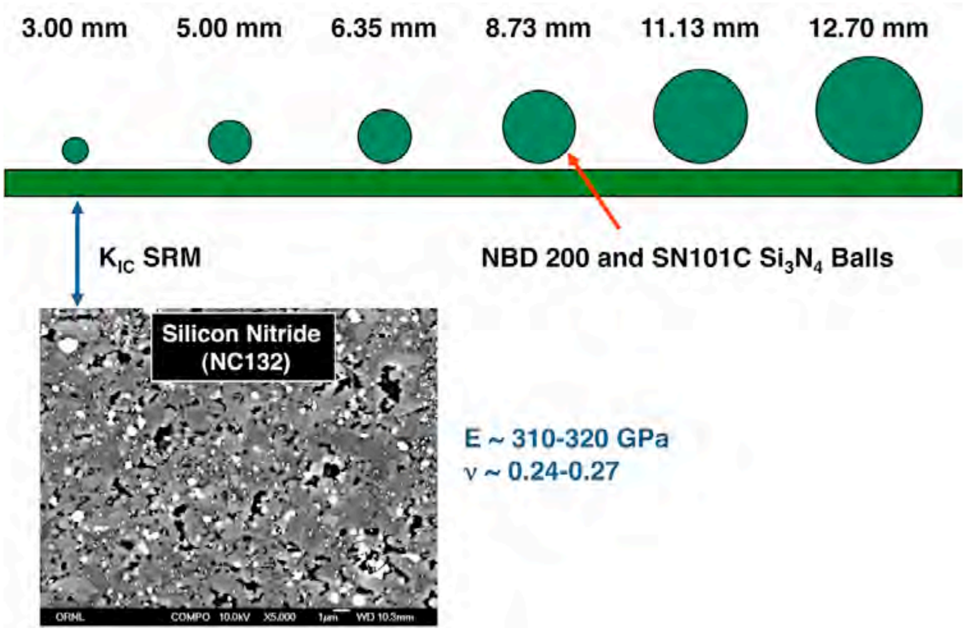

Figure 1.21. Six different silicon nitride ball diameters were used in ring crack initiation tests on a silicon nitride target. The intent was to examine ring cracking in the absence of elastic property mismatch.

The Auerbach relationship (ring crack force linear with indenter radius) for this set of ring crack initiation tests is shown in Fig. 1.22. A linear fit well represented the dependence of ring crack initiation force on indenter radius.

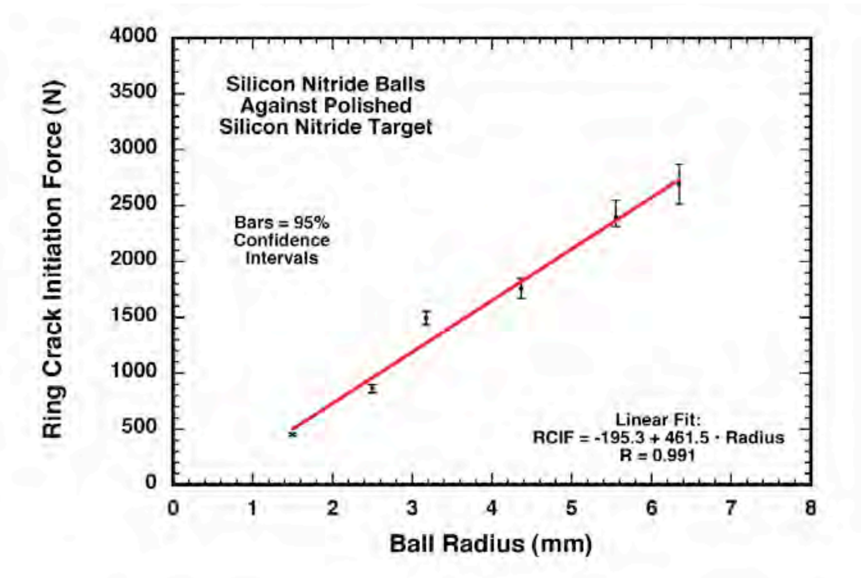

Figure 1.22. Ring crack initiation force as a function of ball radius for the silicon nitride on silicon nitride Hertzian testing. A linear relation was observed.

The relationship of characteristic failure stress as a function of effective area is shown in Fig. 1.23. Equation 1.8 represents that functionality with a Weibull modulus of 7.8 between effective areas of 2000-35000 um^2. Equation 1.22 (frictionless case) was used to estimate the effective area because the ball and target materials were equivalent.

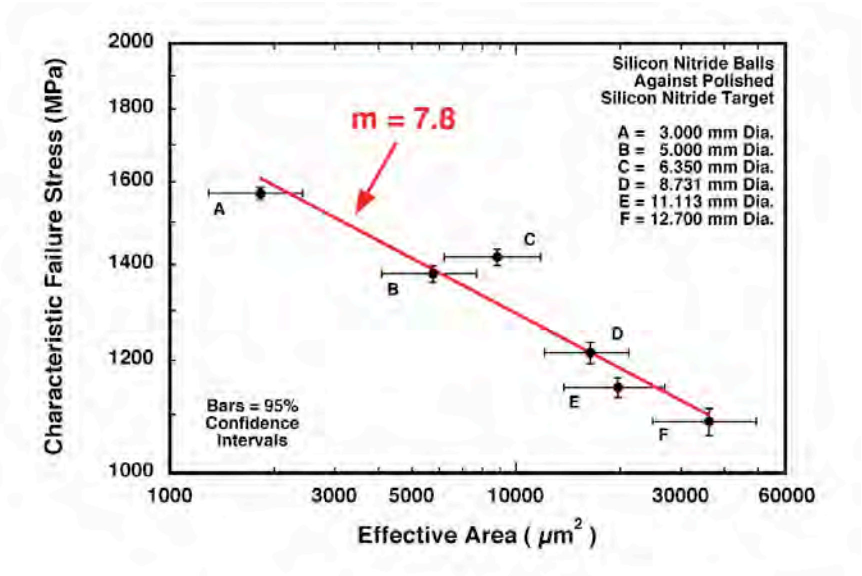

Figure 1.23. Characteristic force as a function of effective area for the six ball diameters. Strength-size scaling is evident among the effective areas produced by the six diameters, which is represented by a Weibull modulus of 7.8.

Summarizing Section 1.4

- A simple, closed-form solution for the effective area for classical spherical or Hertzian (i.e., frictionless or complete slip) indentation was derived. For the infinite friction case (i.e., no slip or complete stiction), an expression for the effective area is given but the integration has to be evaluated numerically.

- Friction with a more compliant spherical indenter will cause the effective area to be less in the target material compared to the frictionless case. That difference gets amplified as the difference in the elastic moduli of the (more compliant) indenter and target material increases. Friction does not affect the effective area when the spherical indenter and target are the same material. Friction with a stiffer spherical indenter will cause the effective area to be more than its frictionless counterpart. That difference gets amplified as the difference in the elastic moduli of the (stiffer) indenter and target material increases. These trends are independent of Weibull modulus.

- This analysis shows the importance of taking into account frictional forces during Hertzian indentation when the target and indenter materials are dissimilar, and gives bounds for the effective area even when the coefficient of friction is unknown.

1.5. Apparent Yield Stress Measurement

The apparent yield stresses (Y_{App}) of numerous ceramics and metals were estimated using diamond spherical or Hertzian indentation, the experimental method described in Daloz, Wereszczak, and Jadaan [1.14], and the estimation of the equivalent stress where maximum shear occurs under a Hertzian indent [1.2]. The measurement of yield stress is relevant because it is a property that is difficult to validly capture and is relevant to armor ceramics because it is an input parameter used in ballistic models. The method's key parts will be revisited here.

The compressive force necessary to initiate apparent yielding was identified postmortem using differential interference contrast (or Nomarski) imaging with an optical microscope. The results from this method are informative because they can show differences in equivalent materials even when their Knoop hardnesses do not [1.7].

Indentation testing was performed using a conventional hardness tester with a 500-µm-diameter diamond indenter. This size enables a large compressive stress to be produced (i.e., those that initiate yielding) at a modest compressive force prolonging the life of the expensive indenter. Larger diameter indenters are more likely to initiate ring cracks before apparent yielding, whereas smaller diameter indenters are more likely to initiate apparent yielding first. With further decreasing indenter size however, stresses can become very high even with small compressive forces. Confident identification of the apparent yield initiation is therefore difficult and often subjective to achieve. Thus, a 500 µm diameter size is an effective compromise for studying yielding behavior.

Each material's metallographically prepared specimen surface was first cleaned with acetone in order to remove any debris or oils that could interfere with indentation or mask identification of apparent yield initiation. Five indents were spaced 0.5 mm apart with increasing load increments of 4.5 N up to a maximum load between 22 to 40 N. The indents were then examined postmortem for indications of apparent yielding. The highest load without apparent yielding and the lowest load with apparent yielding were used to estimate the load at which apparent yielding had initiated. Once a load range was bracketed to +/- 4.5 N, another fifteen sets of five indents each were generated, this time in increments of 2.25 N about the previously determined yield range. For example, if the first test showed yielding at 31 N and no yielding at 26.5 N, then the following tests would be run varying loads from 24.5 N to 33 N at 2.25 N increments. Such finer bracketing resulted in better resolution of the identified yield initiation forces.

The onset of yielding was determined by direct microscopic observation of the indents in differential interference contrast (DIC or Nomarski) imaging using a standard metallographic microscope. With a clean and smooth surface, DIC microscopy allows straightforward imaging of the shallow residual dimples left when yielding has occurred.

Analysis described in Johnson [1.2] was used to estimate the location of maximum shear with respect the Hertzian indentation conditions and elastic properties of the indenter and target material, and that was combined with the load of apparent yielding to estimate the apparent yield stress. The results are summarized in Table 1.4.

Table 1.4. Summary of measured apparent yield stress for various materials.

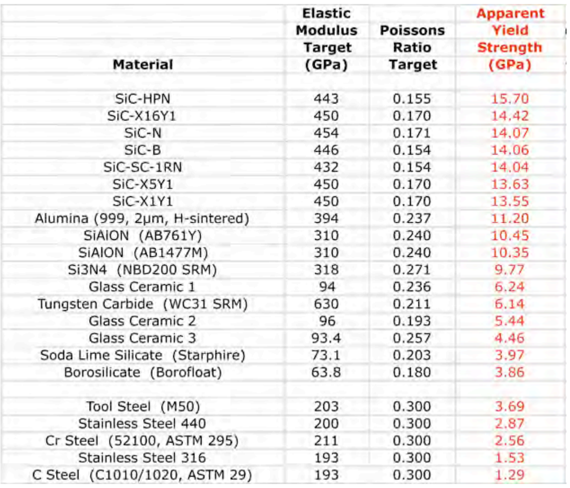

Material	Elastic Modulus Target (GPa)	Poissons Ratio Target	Apparent Yield Strength (GPa)
SiC-HPN	443	0.155	15.70
SiC-X16Y1	450	0.170	14.42
SiC-N	454	0.171	14.07
SiC-B	446	0.154	14.06
SiC-SC-1RN	432	0.154	14.04
SiC-X5Y1	450	0.170	13.63
SiC-X1Y1	450	0.170	13.55
Alumina (999, 2μm, H-sintered)	394	0.237	11.20
SiAlON (AB761Y)	310	0.240	10.45
SiAlON (AB1477M)	310	0.240	10.35
Si3N4 (NBD200 SRM)	318	0.271	9.77
Glass Ceramic 1	94	0.236	6.24
Tungsten Carbide (WC31 SRM)	630	0.211	6.14
Glass Ceramic 2	96	0.193	5.44
Glass Ceramic 3	93.4	0.257	4.46
Soda Lime Silicate (Starphire)	73.1	0.203	3.97
Borosilicate (Borofloat)	63.8	0.180	3.86
Tool Steel (M50)	203	0.300	3.69
Stainless Steel 440	200	0.300	2.87
Cr Steel (52100, ASTM 295)	211	0.300	2.56
Stainless Steel 316	193	0.300	1.53
C Steel (C1010/1020, ASTM 29)	193	0.300	1.29

BAE Advanced Ceramics: all shown SiCs, but SiC-X variants supplied by ARL's J. Campbell.
Ceradyne: 999 alumina.
Kennametal: both SiAlONs.
Corning or Schott: provided the three glass ceramics (which are generically referred to above).
Schott: Borofloat.
PPG: Starphire.
NIST: both standard reference materials (SRMs).
Steels acquired from McMaster-Carr.

1.6. Confinement

The study of the effect of radial confinement on the compressive Hertzian forces necessary to initiate ring cracking and apparent yielding in an alumina ceramic was sought. Finite element analysis results showed that the force needed to initiate both should increase with compressive force. This effect is illustrated in Fig. 1.24.

Uncertainty existed about how to measure the residual compressive (or confinement) stress, so 99.9% alumina was chosen because a residual stress can be quantified [1.15] using photo-stimulated luminescence spectroscopy (PSLS). Cylinders of the alumina (15 mm diameter x 15 mm length) were to be shrink-fitted by aluminum or steel rings. However, several attempts to shrink fit the rings onto the exterior of the alumina cylinder were unsuccessful due to a too-uneven surface finish. A minimum surface finish and cylindricity were determined and will be used if follow-on work occurs.

The ring cracking and apparent yield methods described in Sections 1.2-1.4 will be used with metallographic mounts of the confined alumina. PSLS will first measure the residual compressive stress on the surface of the polished and confined alumina. Hertzian testing responses for fracture initiation (ring cracking) and apparent yielding will then be contrasted against those for the unconfined alumina.

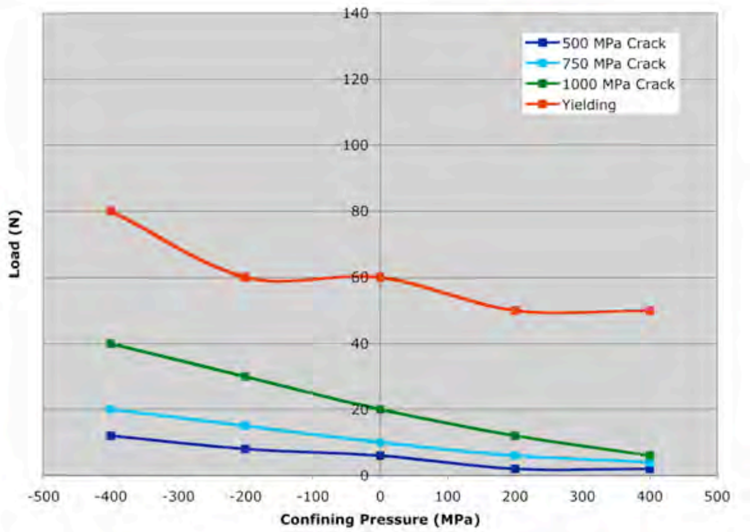

Figure 1.24. Radial confinement pressure increased the necessary compressive forces to initiate both ring cracking and yield-like behavior. However, ring crack initiation is still likely to occur at lower forces than yield-like behavior even under confinement.

1.7. Median Cracking

The many damage mechanisms that can occur during a Hertzian load sequence are schematically shown in Fig. 1.25. The testings of the ring crack and quasi-plasticity mechanisms were described in Sections 1.2-1.5. But among those, the formation of the median crack could be one of the most important in a ballistic event, so the study of it was sought as it is insufficiently studied with Hertzian indentation.

Though other damage mechanisms are, or can be, initiated at lower Hertzian compressive forces, the median crack is important because it is the first to form under the indenter that the indenter "senses" as a significant compliance increase in the target material. This is potentially applicable to the condition where ballistic dwell is overcome and target penetration initiates. Ring and cone cracking forms outside the Hertzian contact area, and though they represent a compliance increase in the target material, the target material is still elastic under the indenter/target Hertzian contact area so the indenter does not "sense" the overall compliance increase in the target material. The formation of the quasi-plastic zone is associated with dimple formation (Section 1.4), and increases the compliance of the target material; however, that zone is confined, and therefore, the indenter does not sense that as a substantial compliance increase.

As shown in Fig. 1.26, quasi-plasticity is a prerequisite for median crack formation. The confined quasi-plastic damage zone, when it gets to a sufficient size from a sufficiently high applied contact stress, creates a sufficiently high first principal tensile stress under the quasi-plastic zone, and a median crack forms. This crack is perpendicular to the target surface and additional loading amounts to driving a wedge though the target material.

This subtask sought to experimentally quantify the conditions for the median crack formation. Displacement-controlled Hertzian indentation using 0.25 and 0.30 mm diameter diamond indenters. Though median cracking was promoted (as evidenced by refracturing tests of the target material), several tests consistently showed it was difficult to identify the load where it initiated. Future tests for median formation will be pursued using force-controlled testing with the indent to promote rapid compliance increase in the target, and facilitate the ability to identify the force where median crack formation initiates.

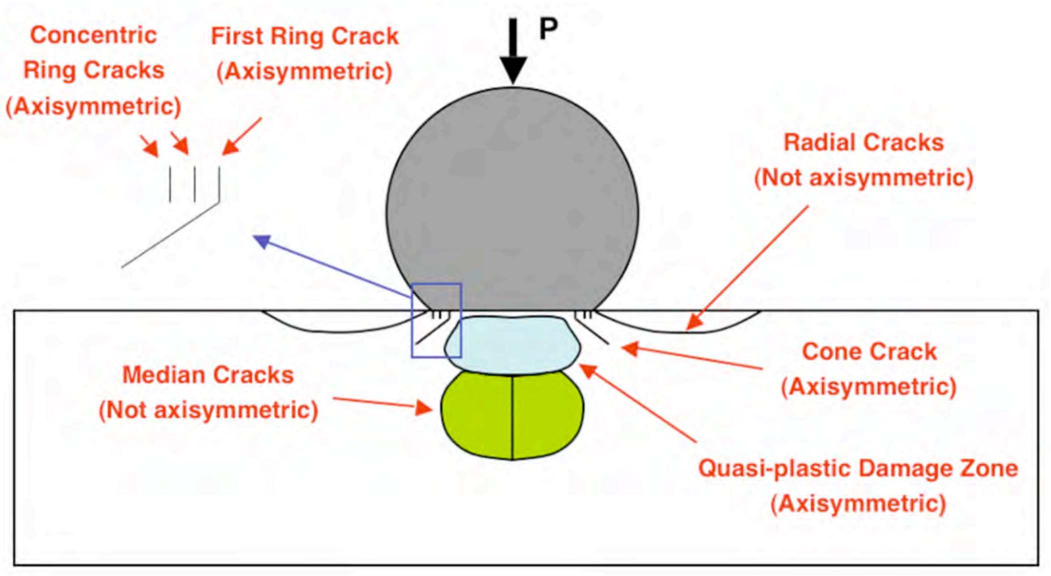

Figure 1.25. The median crack, though not the first to form overall, is the first damage mechanism under the indenter to form that is associated with a large compliance increase in the target material.

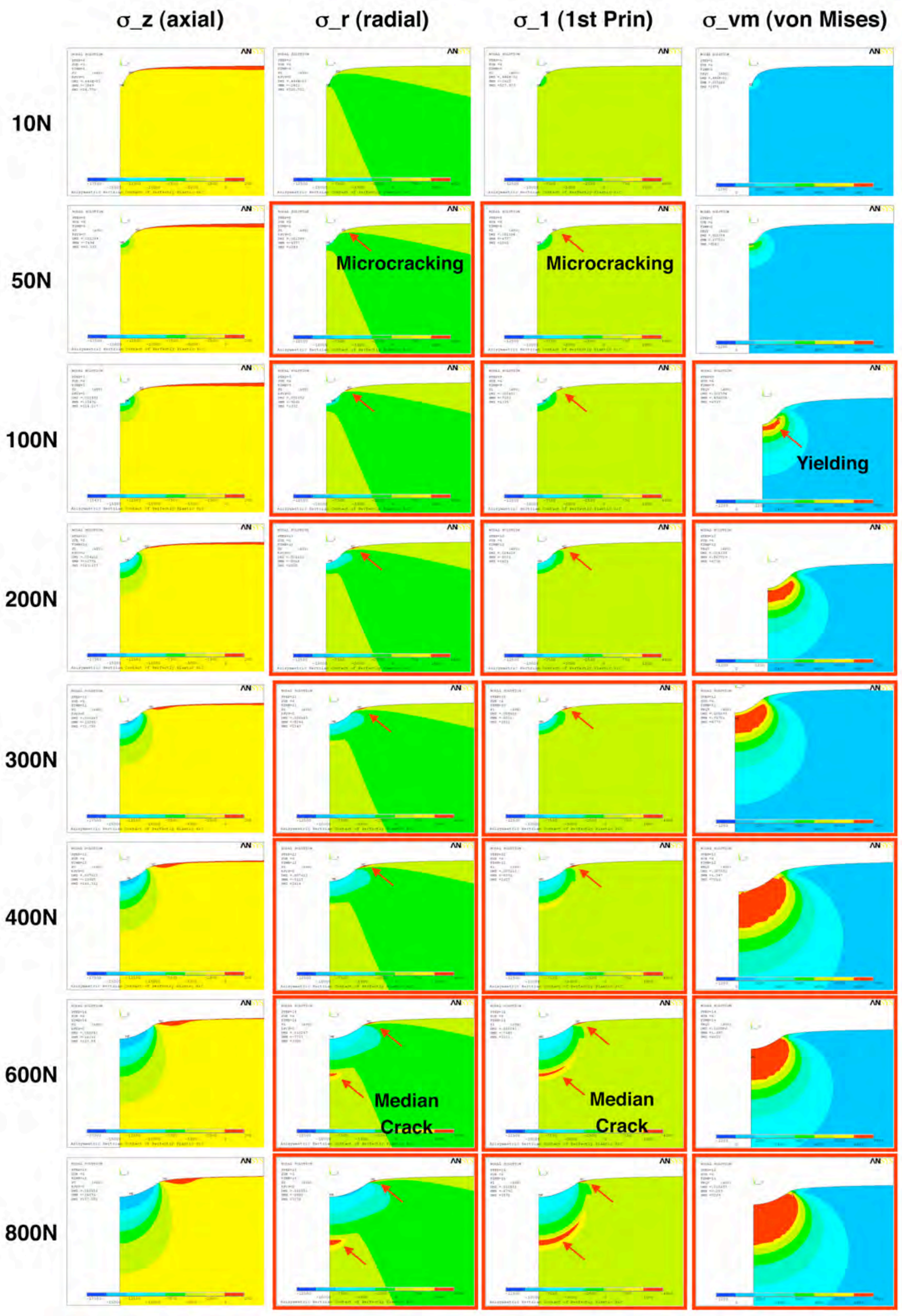

Figure 1.26. Axisymmetric stress profiles as a function of compressive force. 2.0 mm diameter diamond ball diameter against SiC. Ring crack initiation is occurs at the lowest force, followed by yield-like initiation at higher loads, and then median crack formation at higher loads.

1.8. Summary

Characteristic RCIFs of a hot-pressed SiC, a hot-pressed Si_3N_4, and a borosilicate glass were measured using different indenter materials and specially chosen diameters. The results showed that an elastic mismatch effect between the indenter and target material was operative, and consequential frictional forces affected the radial tensile stresses that in turn affected the forces of ring crack initiation. With respect to any target material tested, a more rigid indenter caused higher RCIFs whereas a more compliant indenter lowered it.

Ring cracking in hot-pressed SiC initiated at lower Hertzian indentation forces as the elastic modulus of a spherical indenter decreased. This occurred due to friction. While the coefficient of friction was an unknown and may be experimentally intractable, the determination and interpretation of the ring crack initiation stress can still occur through the simple consideration of frictionless (complete slip) and infinite (complete stick or stiction) friction bounding conditions. Ring crack initiation consistently occurred at lower forces on the SiC having coarser microstructure independent of the test indenter material.

Simpler interpretation and estimation of ring crack initiation stresses with greater fidelity and usefulness will be outcomes if the selected spherical indenter material has the same or similar elastic modulus as that of the target or material. That "elastic property matching" serves to circumvent the complexities that a ubiquitously unknown coefficient of friction introduces in the estimation of Hertzian ring crack initiation stress.

1.9. References

[1.1] R. Mouginot, “Blunt or Sharp Indenters: A Size Transition Analysis,” *J. Am. Ceram. Soc.*, 71:658-661 (1988).

[1.2] K. L. Johnson, *Contact Mechanics*, Cambridge University Press, Cambridge, United Kingdom, 1985.

[1.3] J. Dundurs, “Edge-Bonded Dissimilar Orthogonal Elastic Wedges Under Normal and Shear Loading,” *J. Appl. Mech.*, 36:650-652 (1969).

[1.4] K. L. Johnson, J. J. O’Connor, and A. C. Woodward, “The Effect of the Indenter Elasticity on the Hertzian Fracture of Brittle Materials,” *Proc. R. Soc. Lond.*, 334:95-117 (1973).

[1.5] P. D. Warren and D. A. Hills, “The Influence of Elastic Mismatch Between Indenter and Substrate on Hertzian Fracture,” *J. Mat. Sci.*, 29:2860-2866 (1994).

[1.6] K. T. Strong, Jr., A. A. Wereszczak, W. L. Daloz, and O. M. Jadaan, "Indenter Elastic Modulus and Hertzian Ring Crack Initiation," *Ceramic Engineering and Science Proceedings*, 30, [5] 83-90 (2009).

[1.7] A. A. Wereszczak, K. E. Johanns, and O. M. Jadaan, “Hertzian Ring Crack Initiation in Hot-Pressed Silicon Carbides,” *J. Am. Ceram. Soc.*, 92:1788-1796 (2009).

[1.8] L. E. Goodman, “Contact Stress Analysis of Normally Loaded Rough Spheres,” *J. Appl. Mech.*, 29:515-522 (1962).

[1.9] D. A. Spence, “The Hertz Contact Problem with Finite Friction,” *J. Elasticity*, 5:297-319 (1975).

[1.10] W. Weibull, “A Statistical Distribution Function of Wide Applicability,” *Ingenioersvetens Kapskad. Handl.*, 151:1-45 (1939).

[1.11] G. D. Quinn, “Weibull Strength Scaling for Standardized Rectangular Flexure Specimens,” *J. Am. Ceram. Soc.*, 86:508-10 (2003).

[1.12] B. R. Lawn, “Indentation of Ceramics with Spheres: A Century after Hertz,” *J. Am. Ceram. Soc.,* 81:1977-94 (1998).

[1.13] Anthony Fischer-Cripps, Introduction to Contact Mechanics, Chapter 5, pp. 87-90, Springer-Verlag, 2000.

[1.14] W. L. Daloz, A. A. Wereszczak, and O. M. Jadaan, “Apparent Yield Strength of Hot-Pressed SiCs,” *Cer. Eng. Sci. Proc.*, [6], 29:107-118 (2008).

[1.15] K. E. Johanns, A. A. Wereszczak, and M. J. Lance, "Damage and Residual Stress Fields About Indents inn Different Grain-Sized Aluminas," poster presented at 2006 ICACC, Cocoa Beach, FL, January 2006.

2. GLASS STRENGTH CHARACTERIZATION

2.1. Basis for Inquiry

The goal of the work described in this subsection was to characterize the (tensile) failure stress of candidate transparent armor ceramics using bend testing. This included measuring failure stress as a function of: size or scale, air versus tin side, and location where fracture initiates at the surface or at an edge. The improved understanding of these are important to improving transparent armor because deflection and side-dependencies are active during a ballistic impact.

The glasses examined in this subsection are listed in Table 2.1. P. Patel of the US Army Research Laboratory provided all glass tiles for this subsection. Elastic modulus and Poisson's ratio were measured using resonance ultrasound spectroscopy using a method described elsewhere [2.1].

Table 2.1. Properties of the evaluated glasses.

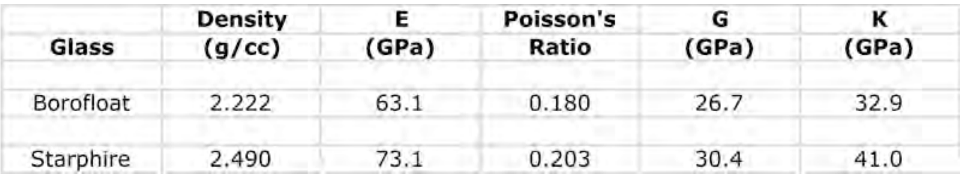

Glass	Density (g/cc)	E (GPa)	Poisson's Ratio	G (GPa)	K (GPa)
Borofloat	2.222	63.1	0.180	26.7	32.9
Starphire	2.490	73.1	0.203	30.4	41.0

2.2. Surface-Located Tensile Failure Stress as a Function of Size

The test matrix for the strength-size scaling study is shown in Table 2.2. Only the Starphire soda lime silicate glass was tested in this matrix. It is comprised of Hertzian ring crack initiation, ball-on-ring (BoR), and ring-on-ring (RoR) testing that samples a wide range of effective areas from the very small (Hertzian ring crack initiation) to the very large (RoR).

Table 2.2. Starphire strength-size scaling test matrix.

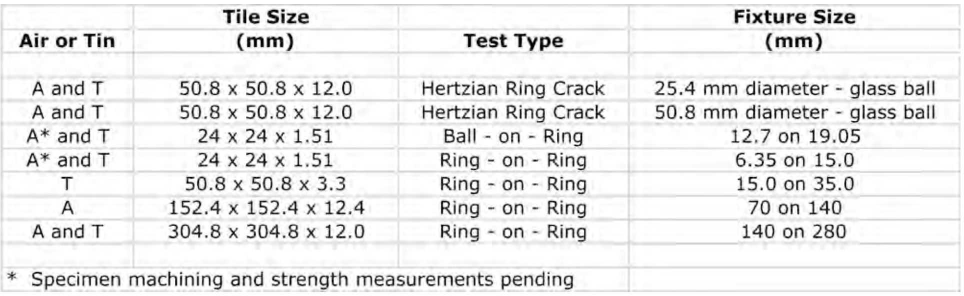

Air or Tin	Tile Size (mm)	Test Type	Fixture Size (mm)
A and T	50.8 x 50.8 x 12.0	Hertzian Ring Crack	25.4 mm diameter - glass ball
A and T	50.8 x 50.8 x 12.0	Hertzian Ring Crack	50.8 mm diameter - glass ball
A* and T	24 x 24 x 1.51	Ball - on - Ring	12.7 on 19.05
A* and T	24 x 24 x 1.51	Ring - on - Ring	6.35 on 15.0
T	50.8 x 50.8 x 3.3	Ring - on - Ring	15.0 on 35.0
A	152.4 x 152.4 x 12.4	Ring - on - Ring	70 on 140
A and T	304.8 x 304.8 x 12.0	Ring - on - Ring	140 on 280
* Specimen machining and strength measurements pending			

Equibiaxial flexure strength was measured using ring-on-ring and ball-on-ring tests. The failure stress for ring-on ring (S_{RoR}) of a square plate was calculated using [2.1]

$$S_{RoR} = \frac{3P}{2\pi t^2}\left[(1-\nu)\frac{D_S{}^2 - D_L{}^2}{2D^2} + (1+\nu)\ln\frac{D_S}{D_L}\right] \tag{2.1}$$

and

$$D = \frac{0.5(l_1 + l_2)}{0.90961 + 0.12652\dfrac{t}{D_S} + 0.00168\ln\dfrac{0.5(l_1 + l_2) - D_S}{t}} \tag{2.2}$$

where P is the failure force, t is thickness, ν is Poisson's ratio, D_S is the support ring diameter, D_L is the loading ring diameter, and l_1 and l_2 are the widths of the plate. The failure stress for ball-on-ring (S_{BoR}) of a square plate using a 12.7 mm diameter WC ball was calculated using [2.2]

$$S_{BoR} = \frac{3P(1+\nu)}{4\pi t^2}\left[1 + 2\ln\left(\frac{D_S/2}{0.4384}\right) + \left[\frac{(1-\nu)D_S{}^2}{(1+\nu)D^2}\right]\left[1 - \left(\frac{0.4384^2}{D_S{}^2/2}\right)\right]\right] \quad . \tag{2.3}$$

Special large RoR fixtures were fabricated to test the large tiles. Rings were machined in aluminum plates that, when populated with 12.7-mm diameter steel balls, formed the desired ring diameters. The fixtures are shown in Figs. 2.1-2.5.

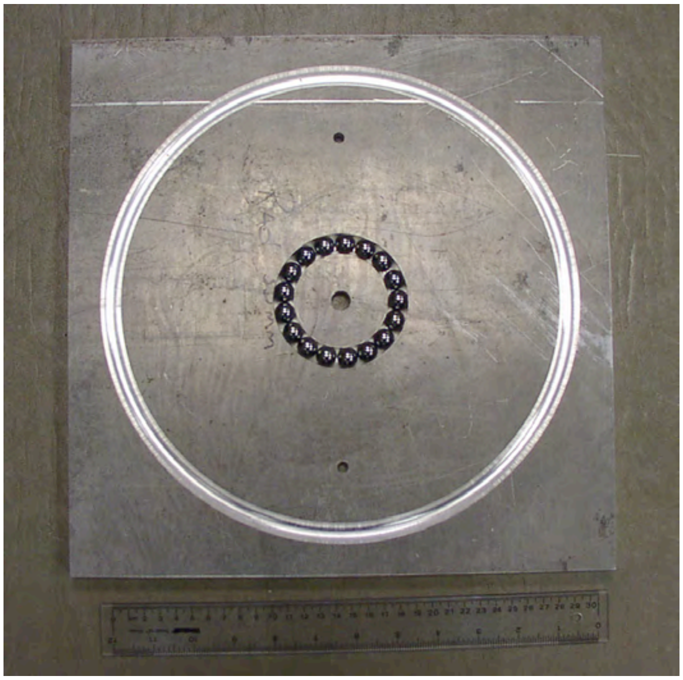

Figure 2.1. Nominal 70-mm (actually 69.2 mm) diameter ring fixture used for RoR biaxial flexure strength testing. 12.7-mm diameter balls comprise the 70-mm ring.

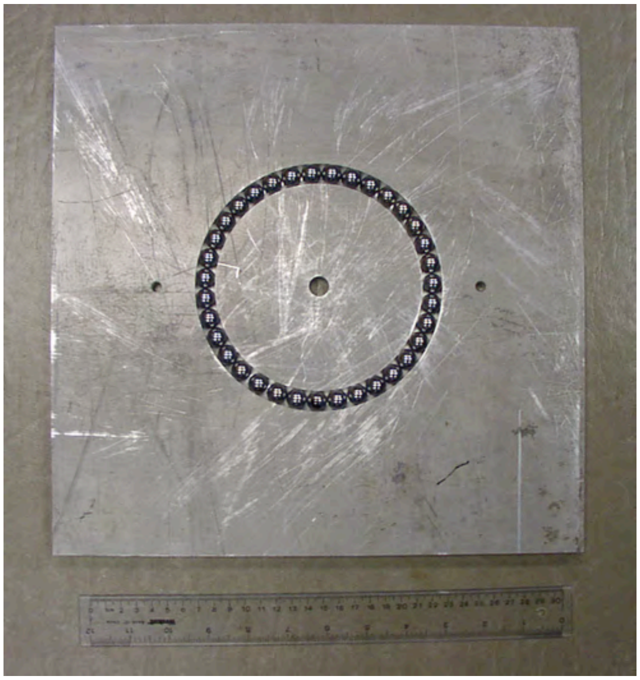

Figure 2.2. Nominal 140-mm (actually 141.7 mm) diameter ring fixture used for RoR biaxial flexure strength testing. 12.7-mm diameter balls comprise the 140-mm ring.

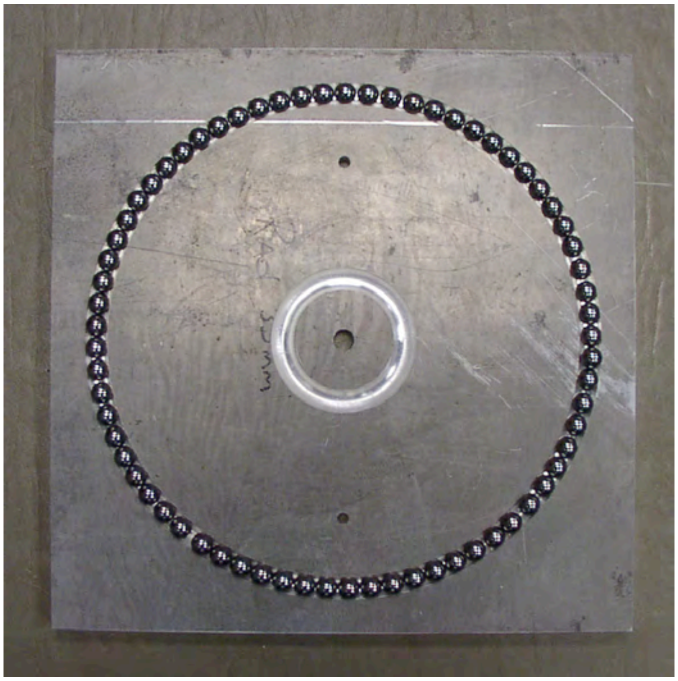

Figure 2.3. Nominal 280-mm (actually 279 mm) diameter ring fixture used for RoR biaxial flexure strength testing. 12.7-mm diameter balls comprise the 280-mm ring.

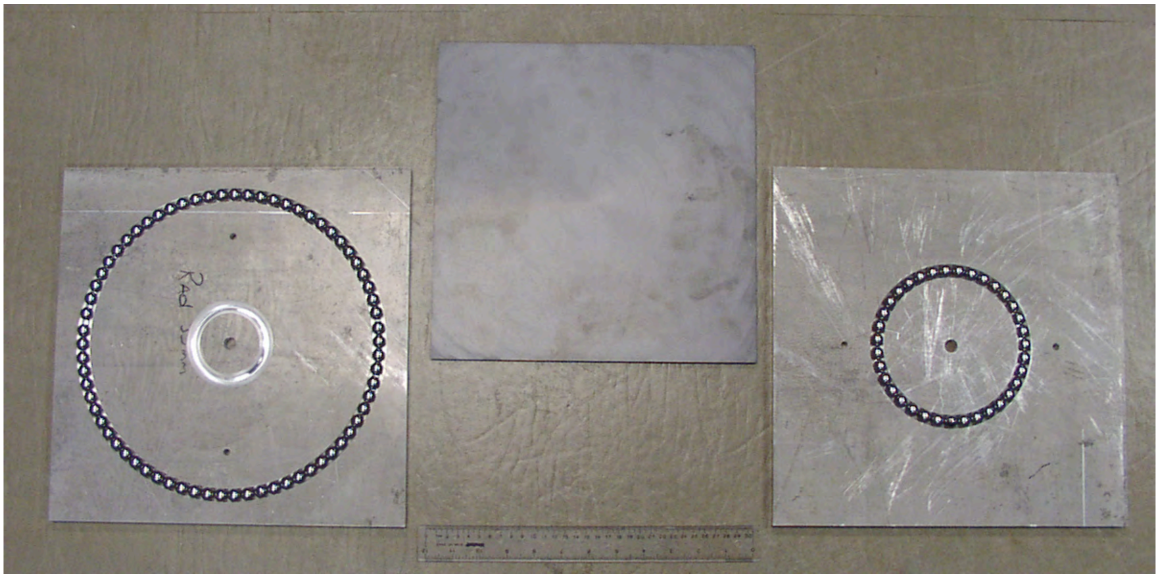

Figure 2.4. Layout shown of 280-mm diameter support ring (left), 305 x 305 mm square ceramic plate that is to be strength tested (center), and 140-mm diameter loading ring (right).

Figure 2.5. Side view of assembled 140/280 mm RoR biaxial flexure strength fixture and 305-mm-square test specimen ready for testing.

Numerous tests were carried out for each of the tests listed in Table 2.2, the (tensile) failure stress determined for each, and then they were fitted against a two-parameter Weibull distribution using commercially available statistical software. The effective areas were estimated using: Reference [2.2] for the RoR data, the Principle of Independent Action for the BoR data [2.3-2.5], and the analysis described in Section 1.4 for the Hertzian ring crack data.

The failure stress as a function of effective area (i.e., strength-size scaling) for Starphire is shown in Fig. 2.6. For the tin side, a Weibull modulus equaling 6.0 represents the strength scaling. Testing is ongoing for the air-side, but preliminary data (at larger effective areas) shows the air side to be stronger which others have shown.

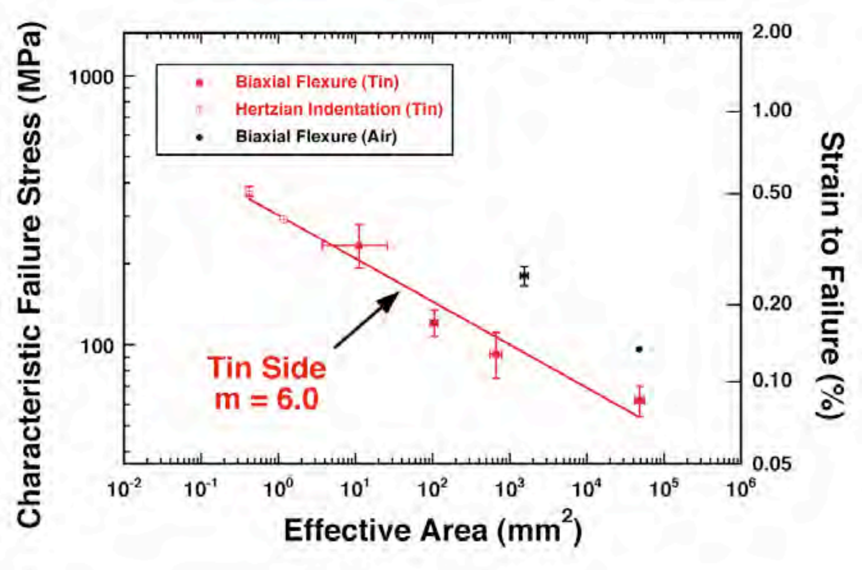

Figure 2.6. Failure stress as a function of effective area for the tin and air sides of Starphire soda lime silicate glass. Weibull modulus of 6.0 represents the scaling between the range of ~ 0.3 to 50,000 mm^2. Air-side testing being completed at the time of this writing.

2.3. Surface- versus Edge-Initiated Failure

Surface-located and edge-located failures comprised the failures of the two largest RoR configurations in Table 2.2. Examples of this are shown in Figs. 2.7-2.8. Additionally, an example of the chamfer at the edge that is associated with such strength-limiting is shown in Fig. 2.9. This is an important observation because it shows the combination of weak edges plus sufficiently high tensile stresses at the edges of tiles can limit "surface-strength", and that that edge-located strength-limiting cannot be ignored or taken for granted.

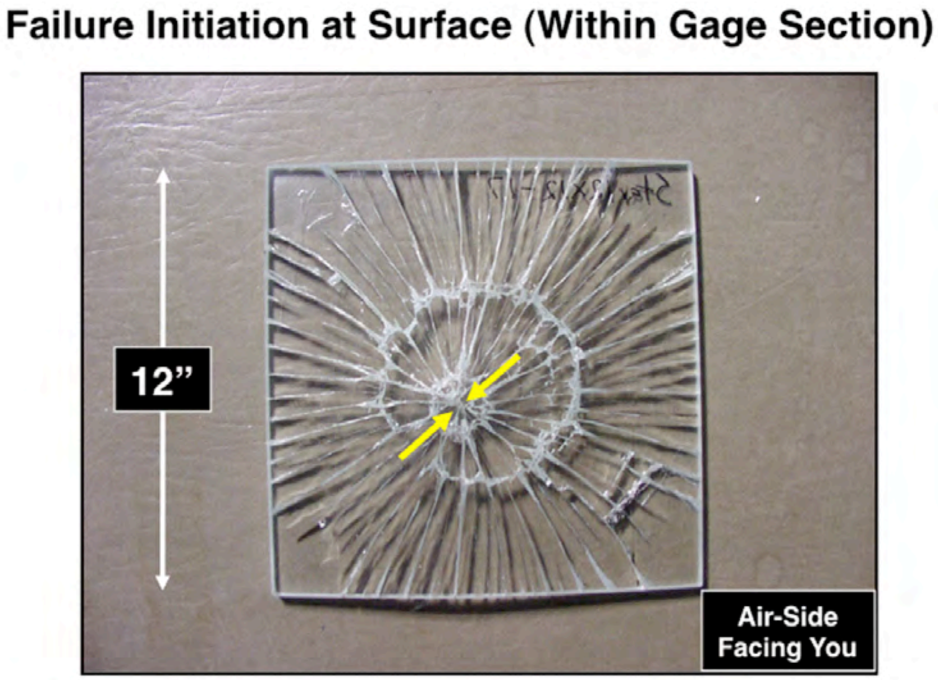

Figure 2.7. Example of surface-located gage-section failure initiation from 140/280 mm RoR testing. Tension side facing up.

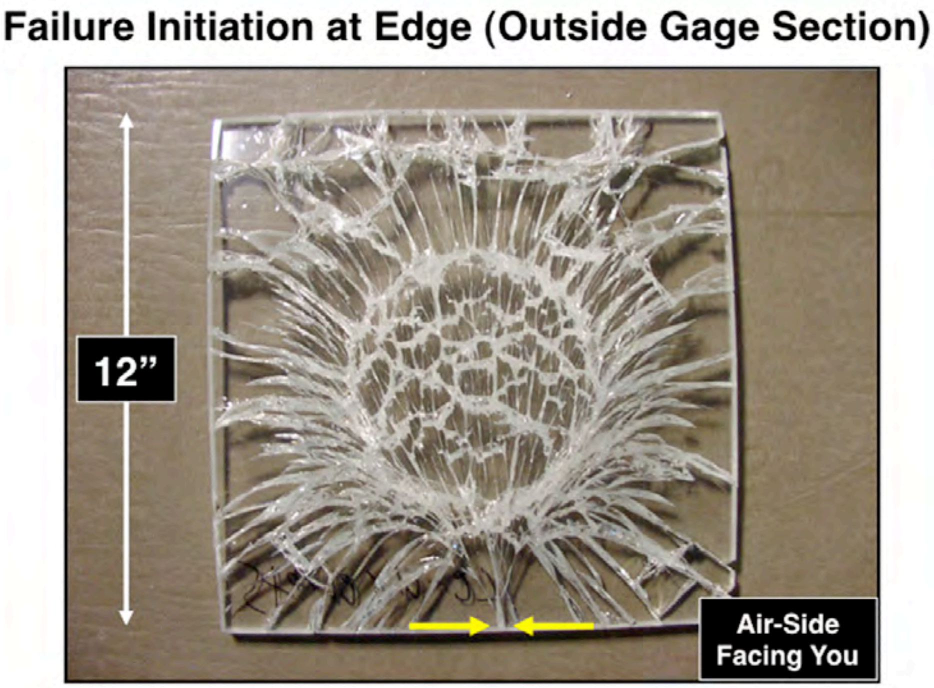

Figure 2.8. Example of edge-located failure initiation from 140/280 mm RoR testing. Tension side facing up.

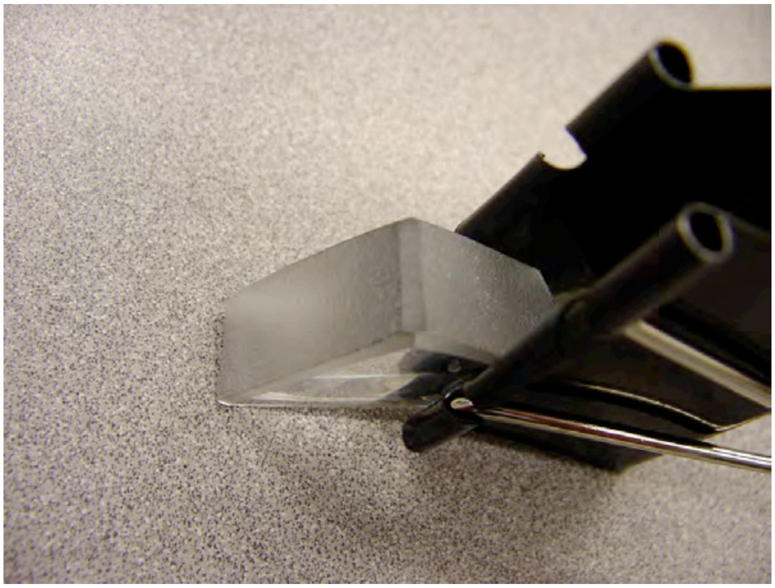

Figure 2.9. View of glass tile fragment showing the supplied chamfering. Thickness of this tile was 12.4 mm.

To further explore the competition of fracture initiation at edges or surfaces, the text matrix shown in Table 2.3 was examined to study the competition of surface- and edge-located failure initiations in RoR testing. Failure initiation locations were identified and studied with respect to the finite element analysis (FEA) estimated surface- and edge-located tensile stresses.

Table 2.3. Starphire strength matrix that produced surface and edge failures.

Tile Size (mm)	**Test Type**	**Fixture Size (mm)**	**Edge Cut**
152.4 x 152.4 x 12.4	Ring - on - Ring	70 on 140	Water-jet
304.8 x 304.8 x 12.0	Ring - on - Ring	140 on 280	Water-jet
355.6 x 355.6 x 12.5	Ring - on - Ring	140 on 280	Scored and bent

The maximum surface- and edge-located tensile stresses as a function of RoR compressive force for the three geometries in Table 2.3 are shown in Figs. 2.10-2.12. For the 152.4-mm tiles RoR-tested with a 70/140mm ring pair (Fig. 2.10), all failure initiations occurred at the tile's edge even though the magnitude of the tensile stress in the RoR gage section was approximately twice as high. For the 304.8-mm tiles RoR-tested with a 140/280mm ring pair (Fig. 2.11), failure initiations occurred within the RoR gage section at lower forces but edge failures occurred at the highest observed failure forces. The same trend occurred with the 355.6-mm tiles RoR tested with the 140/280mm ring pair that had occurred with the 304.8-mm tiles.

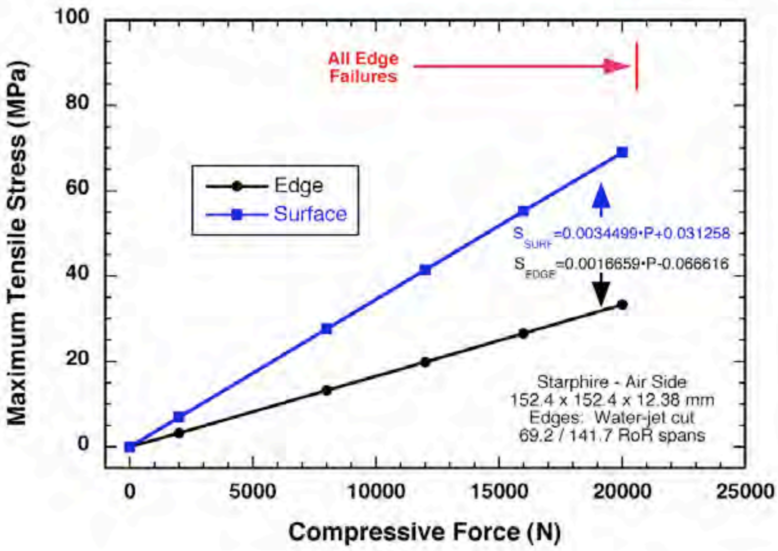

Figure 2.10. Comparison of maximum stress at edge and on the gage-sections surface for the 70/140 mm RoR testing and 152-mm water-jet cut square tiles. Failure initiation started at the edge of all these tiles.

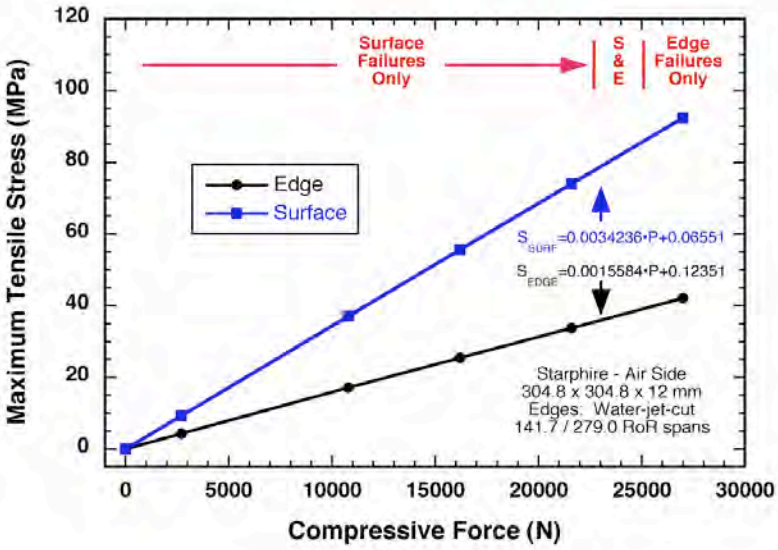

Figure 2.11. Comparison of maximum stress at edge and on the gage-sections surface for the 140/280 mm RoR testing and 305-mm water-jet-cut square tiles. Surface-initiated failures occurred up to ~ 23 kN whereas failures initiated at edges for forces above that.

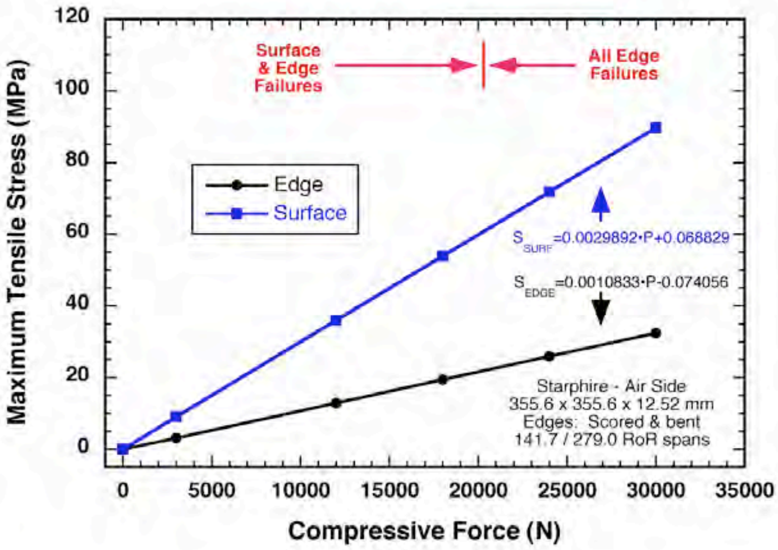

Figure 2.12. Comparison of maximum stress at edge and on the gage-sections surface for the 140/280 mm RoR testing and 356-mm scored and bent square tiles. Surface-initiated failures occurred up to ~ 20 kN whereas failures initiated at edges for forces above that.

The observation that failure stresses associated with surface-located failure initiation are lower than those associated with edge-located failure initiation, even when the maximum stress of the latter is concurrently lower than the former, is an important one. It suggests that failure stress (or strain-to-failure) of glass deflection could be limited by the quality of the edge-state or its chamfering. Additionally, if efforts are made to strengthen glass, then it behooves the practioner to ensure that the edge quality is sufficiently good so that that strengthening can indeed be exploited. Chamfering is an important and necessary part to any glass tile manufacturing, so one potential practice that could improve its quality would be to employ "parallel" or longitudinal directionality when machining them. This is illustrated in Fig. 2.13.

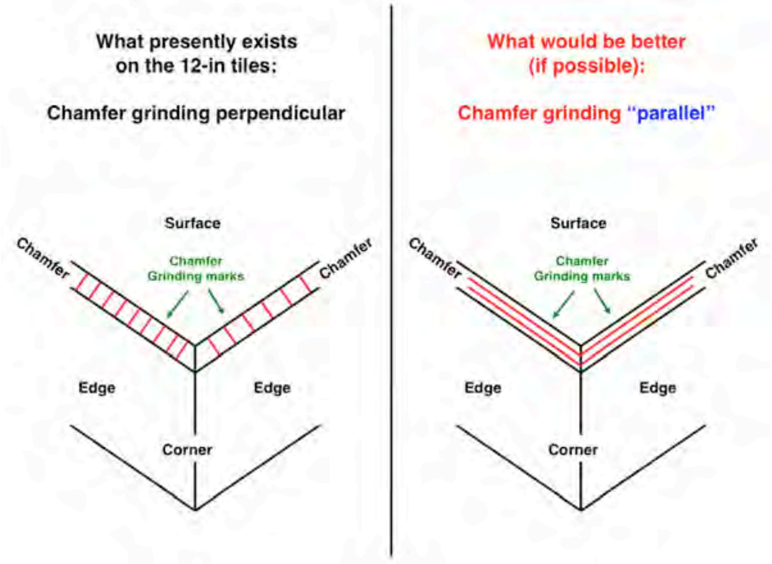

Figure 2.13. Schematic of the tile chamfer and recommended grinding direction to improve strength.

2.4. Edge-Located Tensile Failure Stress as a Function of Size

To examine the edge effect on failure stress further, and its anticipated size-scaling, the flexure test matrix shown in Table 2.4 was explored to purposely cause failure initiation at the edges of 100-mm square tiles of both Starphire and Borofloat. Additionally, failure stresses at edges on both the air and tensile surfaces were examined.

Table 2.4. Edge failure stress test matrix.

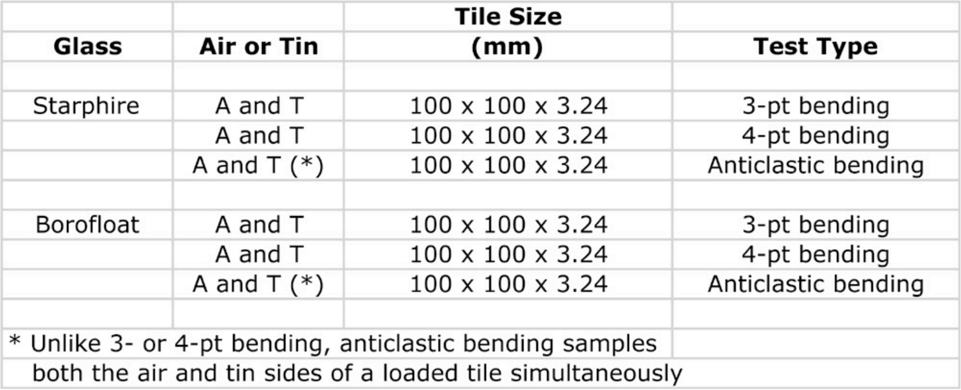

Glass	Air or Tin	Tile Size (mm)	Test Type
Starphire	A and T	100 x 100 x 3.24	3-pt bending
	A and T	100 x 100 x 3.24	4-pt bending
	A and T (*)	100 x 100 x 3.24	Anticlastic bending
Borofloat	A and T	100 x 100 x 3.24	3-pt bending
	A and T	100 x 100 x 3.24	4-pt bending
	A and T (*)	100 x 100 x 3.24	Anticlastic bending

* Unlike 3- or 4-pt bending, anticlastic bending samples
both the air and tin sides of a loaded tile simultaneously

A schematic of the 3-pt flexure setup and an example of a produced tile failure are shown in Figs. 2.14-2.15, respectively. A similar schematic and failure example for 4-pt flexure are shown in Figs. 2.16-2.17, respectively, as well as for anticlastic failure and an example in Figs. 2.18-2.19.

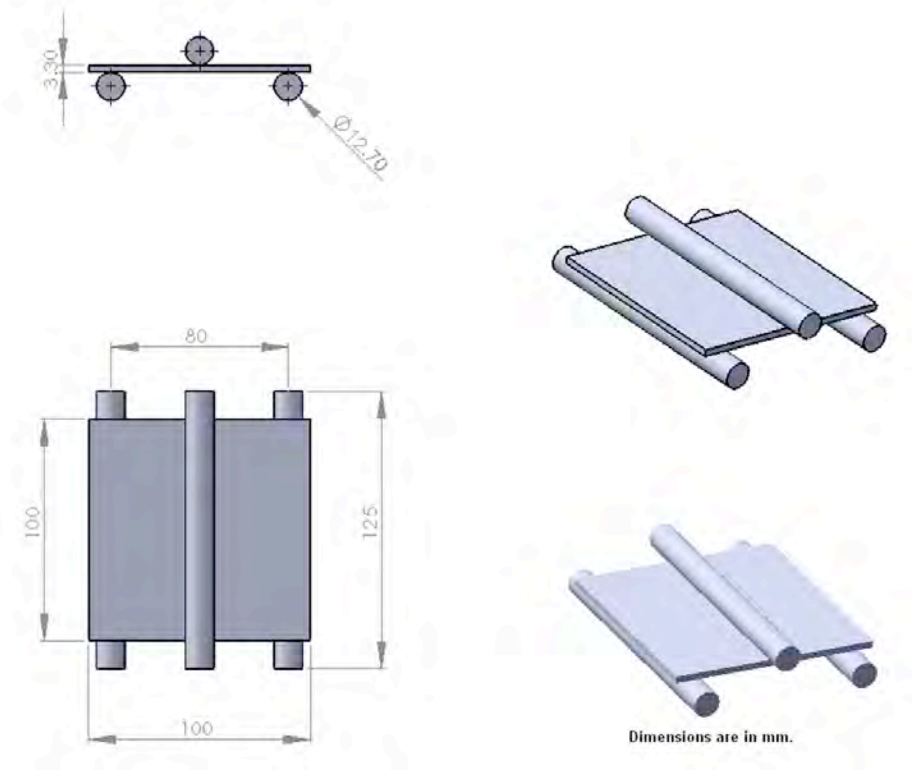

Figure 2.14. Schematic of the 3-pt bend loading configuration used in the edge-testing matrix. Dimensions in mm.

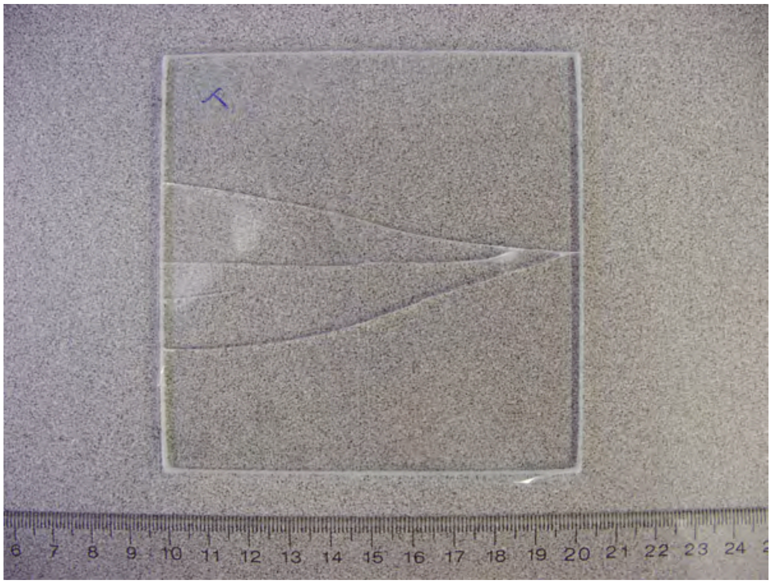

Figure 2.15. Example of 100-mm square tile fractured in 3-pt bending. Failure initiation occurred at the right edge.

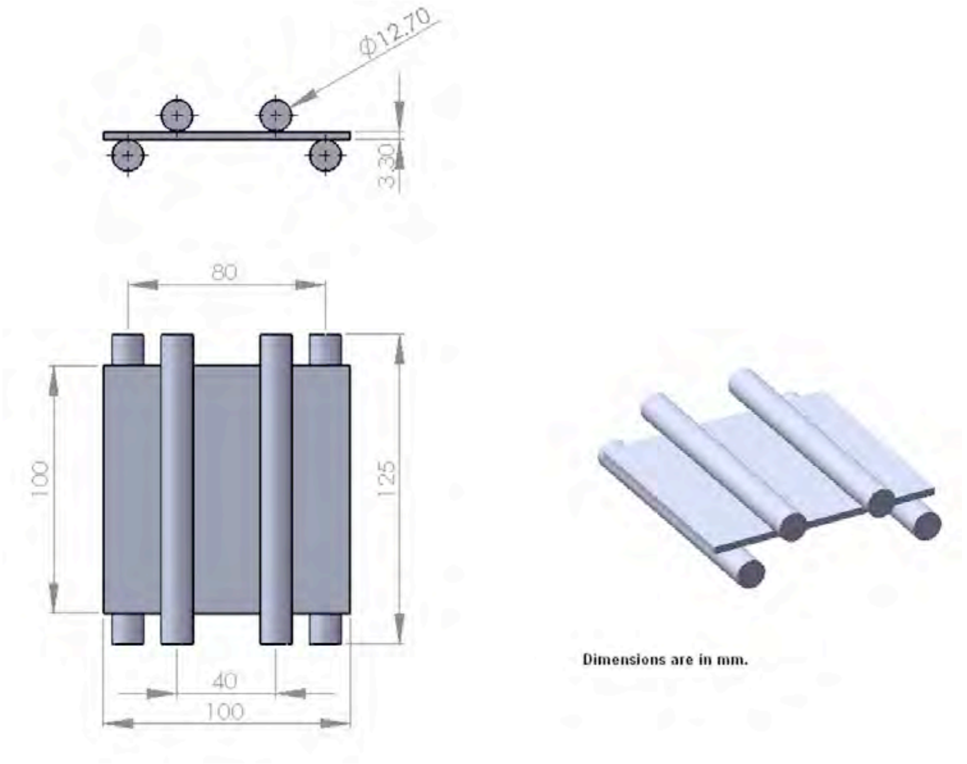

Figure 2.16. Schematic of the 4-pt bend loading configuration used in the edge-testing matrix. Dimensions in mm.

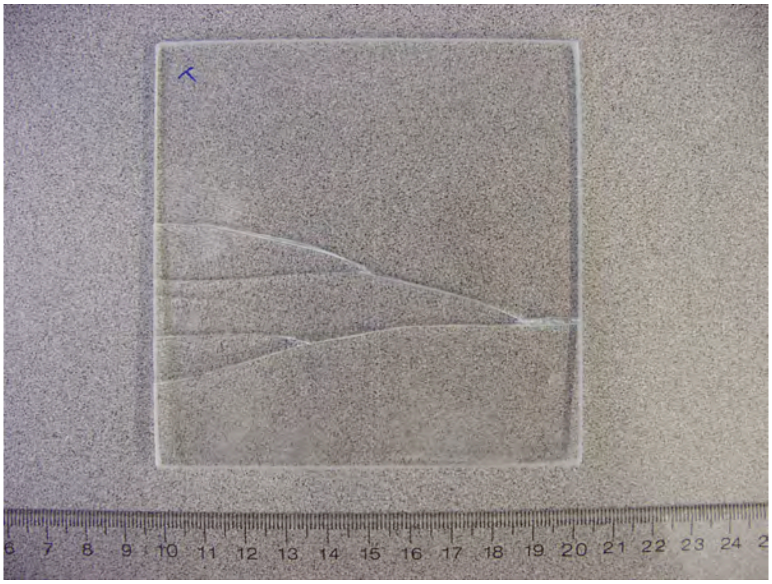

Figure 2.17. Example of 100-mm square tile fractured in 4-pt bending. Failure initiation occurred at the right edge.

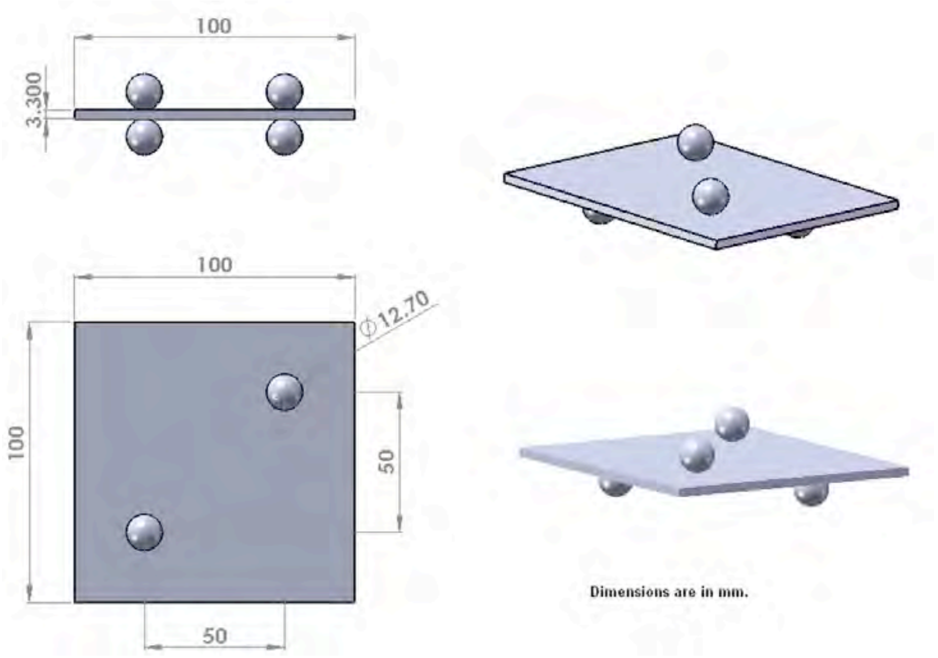

Figure 2.18. Schematic of the anticlastic bend loading configuration used in the edge-testing matrix. Dimensions in mm.

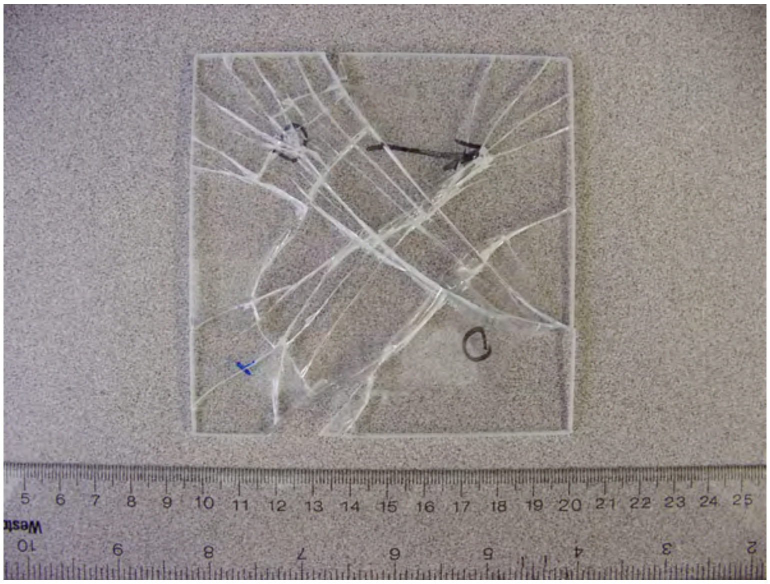

Figure 2.19. Example of 100-mm square tile fractured in anticlastic bending. Failure initiation occurred at the right edge approximately one-fourth the way up from the lower right corner.

The anticlastic bend specimen has been used for many years in the field of metallurgy to study fatigue [2.6-2.8]. Its use in the present study with glass was of interest because of its potential to effectively study edge effects for a test coupon that has an inherently good surface finish. This last issue is illustrated in Fig. 2.20. Even though Hertzian loading generates the highest tensile stresses subjected onto the anticlastic test coupon, it is the combination of the very good surface integrity of glass (i.e., relatively high resistance to Hertzian ring crack initiation) and the relatively low strain-to-failure at the glass edges that results in this test configuration being utilizable with glass (and other materials or coupons with similar characteristics, e.g., semiconductor chips). The σ_x stress field for a deflected anticlastic bend specimen is illustrated in Figs. 2.21-2.22.

Another attractive feature of the anticlastic flexure specimen is that it subjects one-half of the edge length *of all eight primary edges* to a tensile stress. Uniaxial flexure testing (i.e., 3- or 4-pt) only subjects a portion of two of the eight edges to tensile stress, and it only samples edges on either the air or tin sides, so more test coupons must be tested to test both sides than with anticlastic bending.

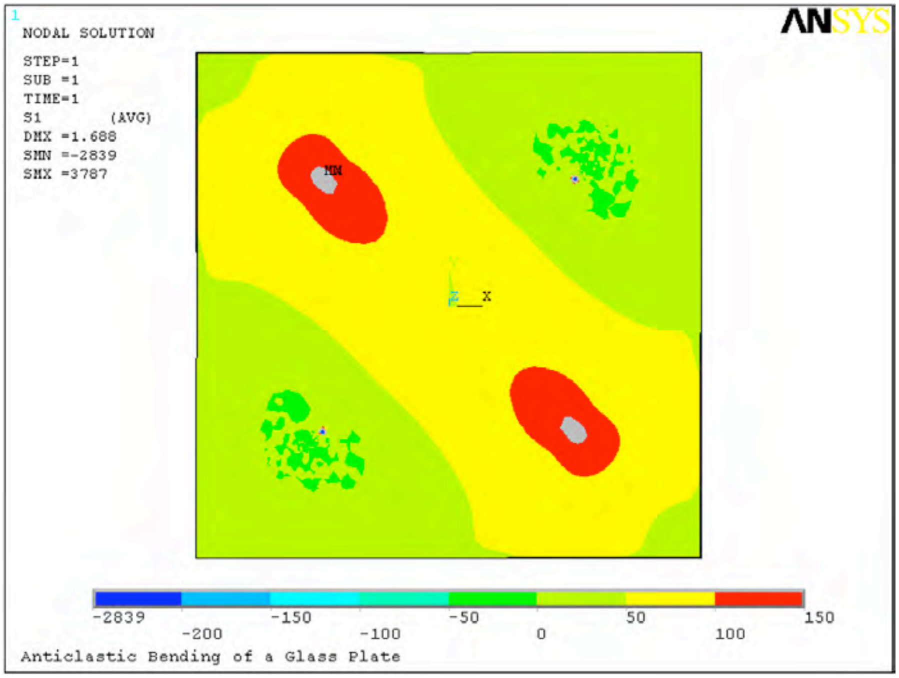

Figure 2.20. Top view of the first principal stress field of an anticlastic bent tile. Though the highest tensile stresses are around the Hertzian ball loading, it is the (more modest) tensile stresses at the edges that initiate fracture.

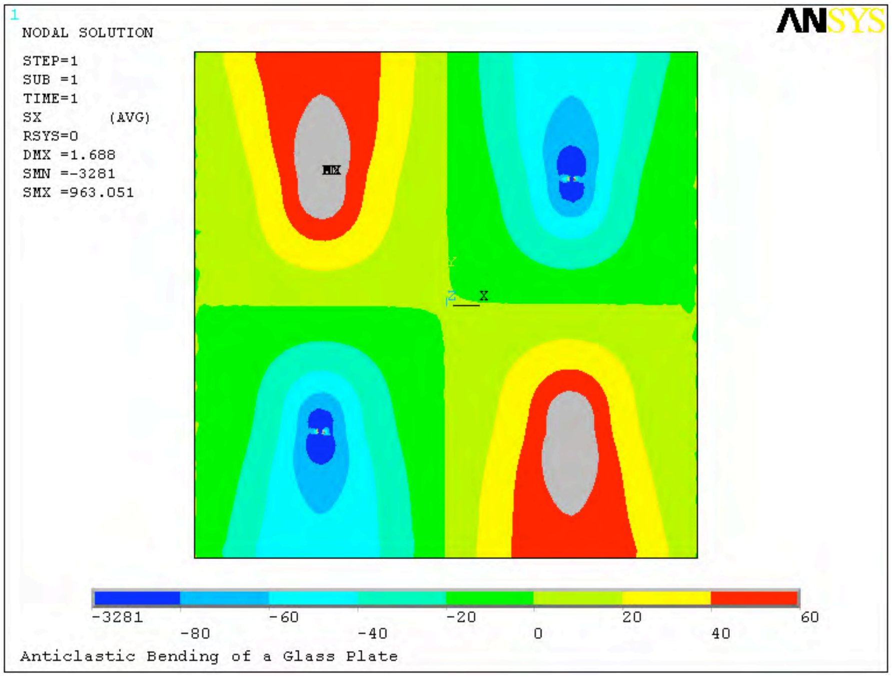

Figure 2.21. Top view of the σ_x (horizontal uniaxial) stress field of an anticlastic bent tile. The tensile stress at one of the edges initiates fracture.

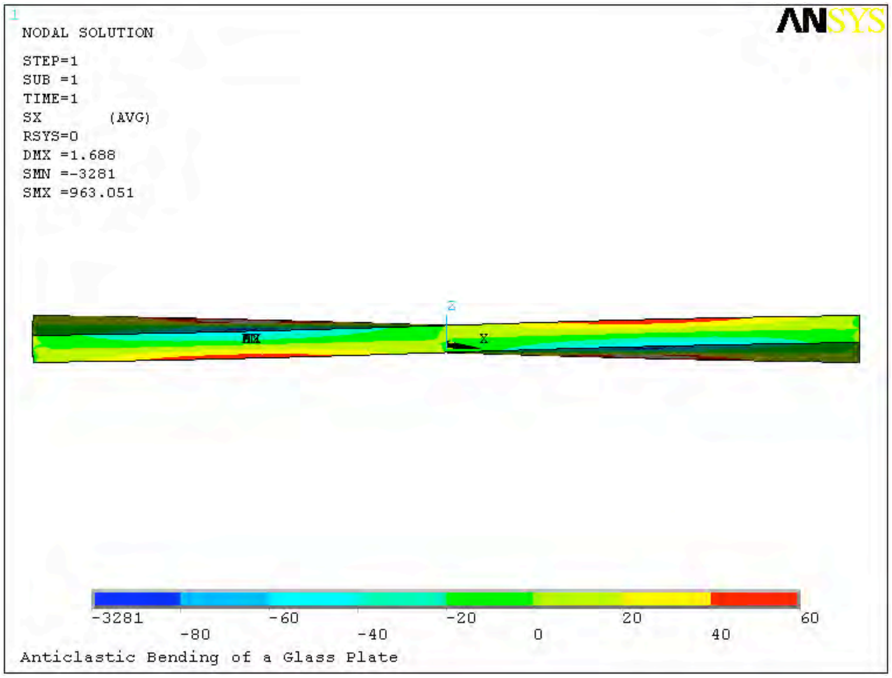

Figure 2.22. Side view of the σ_x (horizontal uniaxial) stress field of an anticlastic bent tile. The tensile stress at one of the edges initiates fracture.

To link anticlastic bending failure force to a maximum failure stress, finite element analysis was conducted with the anticlastic bend fixture and tile geometries shown in Fig. 2.18. To assess any presence of non-linear effects, both linear and non-linear analyses were conducted, and their results are shown in Fig. 2.23. Their stress states were concluded to be equivalent (given the uncertainties of the FEA model and meshing), so the linear relationship shown in Fig. 2.18 for both glasses was used to estimate anticlastic bending failure stress.

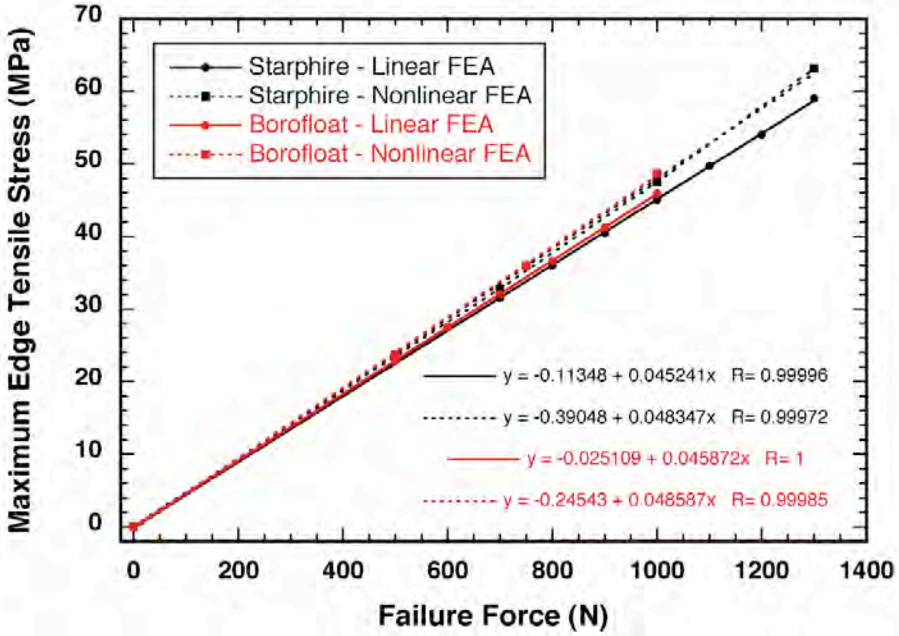

Figure 2.23. Maximum edge tensile stress as function of failure force for both investigated glasses under linear and nonlinear FEA conditions. Modeled conditions for dimensions shown in Fig. 2.18. There was not a significant difference, so the linear condition was used to estimate tensile failure stress.

The effective length (L_{eff}) of the anticlastic specimen described in Fig. 2.18 was estimated as a function of Weibull modulus using finite element analysis and the Principle of Independent Action [2.4-2.5]. The resulting function is shown in Fig. 2.24.

The effective length estimations for uniaxial flexure are relatively simple. The L_{eff} for 3-pt flexure is

$$L_{eff\text{-}3pt} = (2 \bullet L)/(m+1) \tag{2.4}$$

where L is the lower or support span and m is the Weibull modulus. For 4-pt (quarter-point) flexure, it is

$$L_{eff\text{-}4pt} = ((m+2)/(m+1)) \bullet L \quad . \tag{2.5}$$

In the present study, the L in both Eqs. 2.4-2.5 is 80 mm.

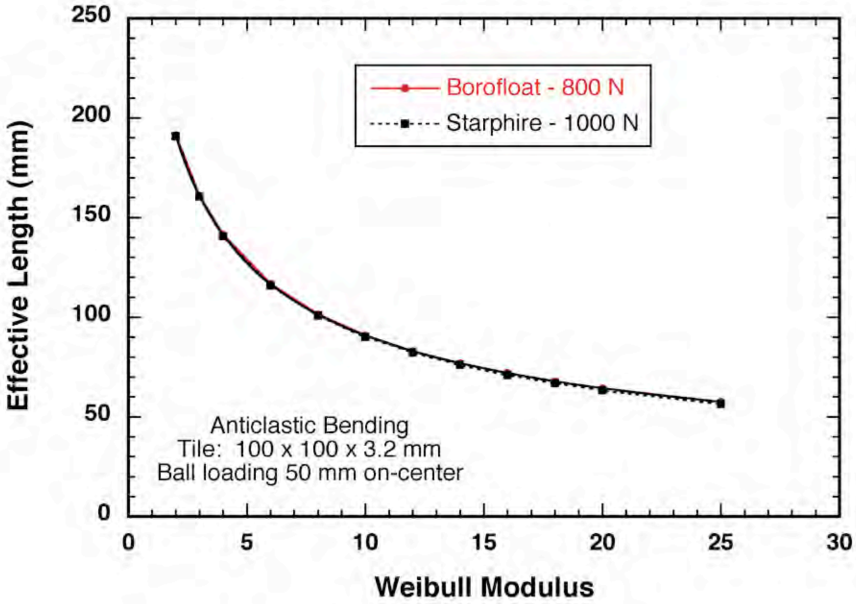

Figure 2.24. Effective length as a function of Weibull modulus for anticlastic bending of the plate shown in Fig. 2.18 was estimated using the Principle of Independent Action [2.4-2.5].

The characteristic failure forces as a function of effective length for all three test geometries, both glasses, and both the air and tin sides are shown in Fig. 2.25. The Weibull modulus is very low for the tin sides of both the Starphire and Borofloat glasses; these low values represent a very large amount of scatter in strength that in turn reflects inconsistent chamfering on the tin sides.

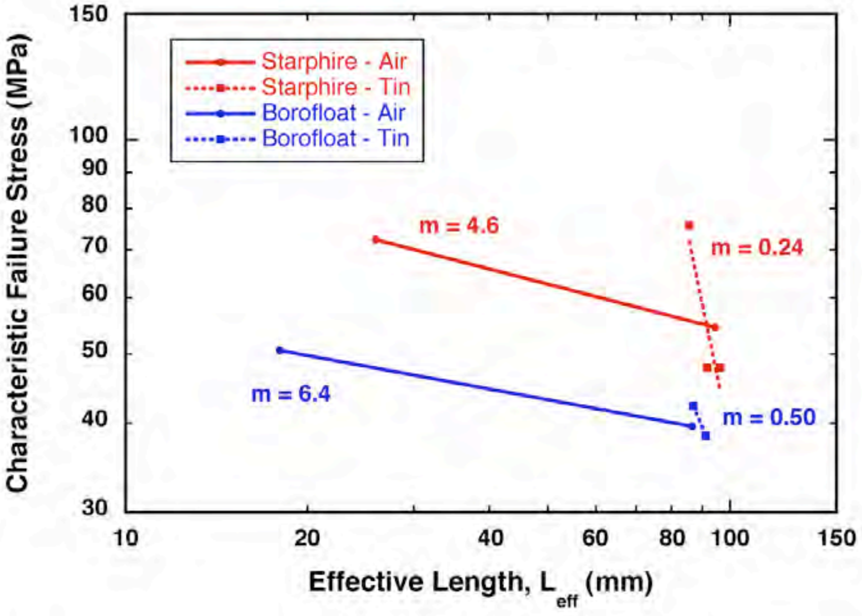

Figure 2.25. Characteristic failure stress as a function of effective length for glass tiles tested according to loadings shown in Fig. 2.14, 2.16, and 2.18.

2.5. Summary

The efforts described in this subsection clearly illustrate that glasses used for transparent armor exhibit strength-size scaling and that the quality of their edges can affect how much bending it can withstand before fracturing. Therefore, in order to exploit allowable surface deflections caused by a ballistic event, homage must be paid to the quality of the edge preparation of the glass.

2.6. References

[2.1] A. A. Wereszczak, "Elastic Property Determination of WC Spheres and Estimation of Compressive Loads and Impact Velocities That Initiate Their Yielding and Cracking," *Ceramic Engineering and Science Proceedings*, [7], 27:211-223 (2006).

[2.2] ASTM C 1499, "Standard Test Method for Monotonic Equibiaxial Flexure Strength of Advanced Ceramics at Ambient Temperatures," Vol. 15.01, 2008, ASTM, West Conshohocken, PA.

[2.3] G. de With and H. H. M. Wagemans, "Ball-on-Ring Test Revisited," *J. Am. Cer. Soc.*, 72:1538-1541 (1989).

[2.4] R. L. Barnett, P. C. Hermann, J. R. Wingfield, and C. L. Connors, "Fracture of Brittle Materials Under Transient Mechanical and Thermal Loading," Technical Report AFFDL-TR-66-220, March, 1967.

[2.5] A. M. Freudenthal, "Statistical Approach to Brittle Fracture," pp. 591-619 in Facture, An Advanced Treatise, Vol. 2, Mathematical Fundamentals, Academic Press, 1968.

[2.6] S. Y. Zamrik, and M. Shabara, "The Effect of Stress Ratio on Fatigue Crack Growth in a Biaxial Stress Field," *ASME Trans. J. Press. Vessel Tech., Vol. 99*, [1], 99:137-143 (1977).
[2.7] S. Y. Zamrik, and D. C. Davis, "A Novel Test Method and Apparatus for Multiaxial Fatigue Studies," *Advances in Multiaxial Fatigue*, pp. 204-219 in ASTM STP 1191, D. L. McDowell and R. Ellis, Eds., ASTM, (1993).
[2.8] S. Y. Zamrik, and R. E. Ryan, "Fatigue Crack Propagation in IN-718 Material under Biaxial Stress Bending," *Advances in Fatigue Lifetime Predictive Techniques*, pp. 161-187 in ASTM STP 1292, M. R. Mitchell and R. W. Landgraf, Eds., ASTM, (1996).

3. GLASS SURFACE MODIFICATION - PLASMA ARC HEATING

3.1. Basis for Inquiry

Improving the flexure strength of transparent glass and glass ceramics is desirable because it concomitantly improves the strain-to-failure and therefore increases the time of projectile-target interaction and improves ballistic resistance.

There are several processes that are known to increase the flexure strength of glass. Under an applied tensile stress, they all act to lessen the stress concentration of surface-located flaws. Many of those strengthening processes were identified decades ago and include ion exchange methods involving molten salts [3.1], acid etching [3.2], annealing and tempering [3.3], and simply storing glass in water [3.4]. Since then, the application of inorganic or organic coatings [3.5-3.6], and the use of flame-sprayed glazings [3.7] and flame-sprayed gas reagents [3.8] have been shown to increase strength too. These strengthening methods require either the use of: chemicals, time-consuming and carefully controlled thermal processing, a service condition that the glass is not likely to experience (i.e., constant submersion in water), the deposition of a coating that might not withstand impact conditions or that may affect transparency, or combinations thereof.

Another process that serves to lessen stress concentrations on glass surfaces is fire polishing. A flame is used to provide rapid, short-term, and intense heating on a glass surface. That causes a reduction of the glass viscosity in that locality and surface-tension stress concentrators (e.g., surface flaws, edges, etc.) are reduced. Because of the rapid and short-term exposure, the total amount of absorbed heat is low, so the bulk of the glass remains at a temperature below which glass viscosity is minimally or not reduced. An oxycombustion process can be used to accomplish fire polishing [3.9] but it has its disadvantages. If the burners are positioned too far away from the glass, then a lot of energy is wasted. If they are too close, then the flame temperature may not be optimized and soot could also be deposited on the glass.

A method not used yet with glass, but that has potential attractiveness to produce strengthening analogous to how fire polishing works, is plasma-arc heating [3.10]. It can produce very rapid heating and cooling, precise temperature control, instantaneous starting and stopping, does not rely on the use of chemicals or gases and therefore generates no waste by-product nor deposits soot, is amenable for processing large quantities of glass, and can be used by either the glass manufacturer, the end user, or both. A controlled and contained plasma, which has a temperature greater than 10000 K, forms the basis of the lamp. A water-cooled and highly polished line focus reflector redirects the radial radiant energy output to the sample being processed. Its ability to provide intense heating on a surface in less than a second offers the potential to produce surface flaw healing without heating or affecting the majority the glass.

In this study, a soda-lime silicate glass was irradiated with a plasma-arc lamp to examine if strengthening was producible. Strength tests of untreated and treated tiles were performed to study, compare, and examine any changes in the behavior of edge- and surface-located fracture initiation.

3.2. Processing Conditions and Testing

The examined glass was a commercially available float soda-lime silicate. Its density was measured to be 2.49 g/cm^3. Additionally, its elastic modulus and Poisson's ratio were measured with a resonance ultrasound spectroscope and a method described elsewhere [3.11] and were 73.1 GPa and 0.203, respectively.

A 300 kW plasma arc lamp with a 10-cm configuration capable of delivering 3.5 kW/cm^2 at 100% power was used to irradiate the glass samples [3.10]. It is shown in Fig. 3.1. Initial, but non-optimized, heat-treating resulted in the irradiation of samples at a power density of 900 W/cm^2. The lamp was held stationary at a standoff distance of 2 cm and each tile sample was set on a table that unidirectionally translated it under the lamp at a speed of 8 mm/s. Every tile sample (50 x 50 x 3.3 mm) was wiped clean with alcohol just prior to irradiation. Thirty tiles were irradiated over a course of two days in ambient air (55% RH, 23°C). The tin-side was irradiated because it is known to be weaker than the air-side [3.12-3.15].

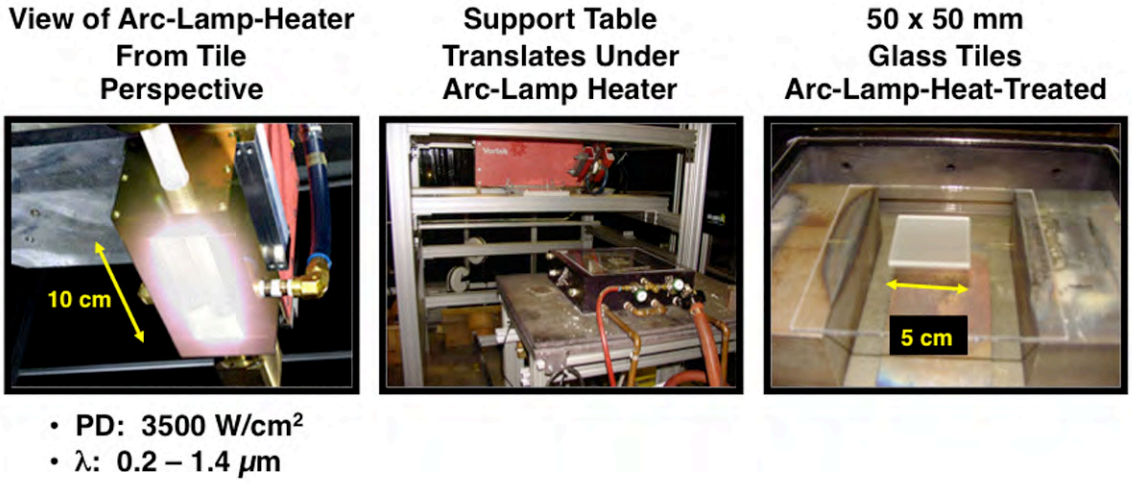

Figure 3.1. Pictures of the plasma arc lamp and the tile positioning.

The strength testing of the thirty tiles was completed within 3 days after their irradiation. Thirty untreated tiles were also tested. All 60 tiles were tested in a random order. 4-point-flexure and ring-on-ring flexure tests were performed. Given the two strength tests types and two glass conditions (heat-treated and untreated), 15 specimens were tested with each strength-test-glass-condition combination.

Uniaxial flexure strength was measured with 4-point bending from an adaptation of ASTM C1161 [3.16]. A semi-articulating fixture with 6.35-mm-diameter carbon-steel roller pins, a crosshead displacement rate of 0.5 mm/min, and a universal testing machine were used. The failure load was recorded in each test. The failure stress for 4-point-bending (S_{4pt}) was calculated using

$$S_{4pt} = \frac{3P\left(L_S - L_L\right)}{2bt^2} \tag{3.1}$$

where P is the failure force, L_S and L_L are support and loading bend spans, respectively, b is the base dimension, and t is thickness or height. For S_{4pt} testing, L_S = 40 mm, L_L = 20 mm, b = 50 mm, and t = 3.3 mm. A schematic of the 4-point bend test fixture is shown in Fig. 3.2.

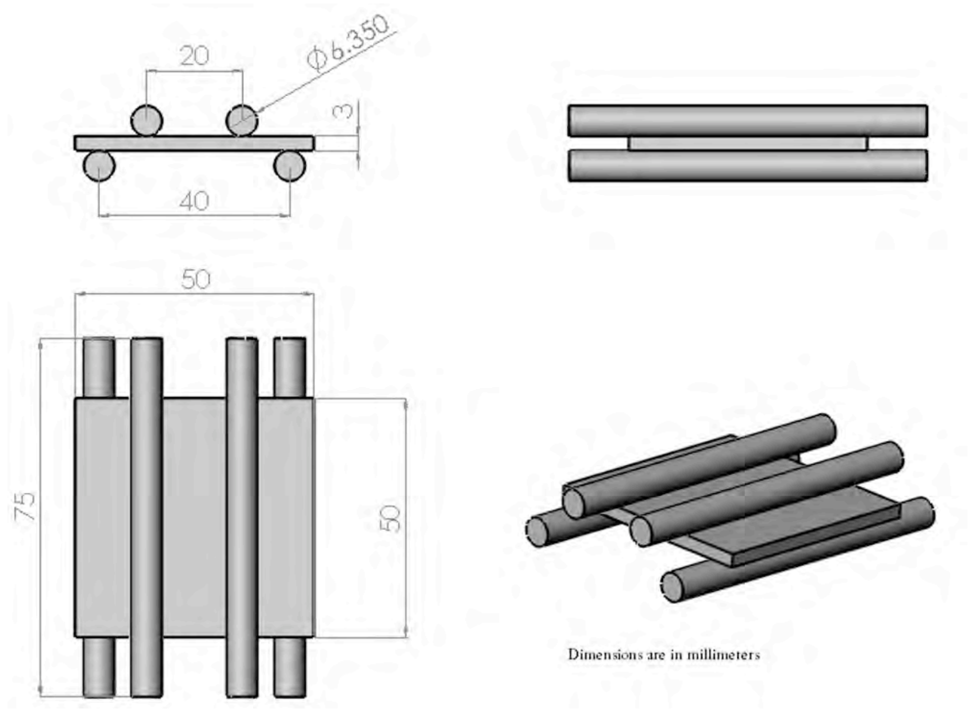

Figure 3.2. Schematic of the 4-pt bend loading configuration. Dimensions in mm.

Equibiaxial flexure strength was measured using ring-on-ring testing. A semi-articulating fixture made from carbon steel, a crosshead displacement rate of 0.5 mm/min, and a universal testing machine were used. Graphoil sheeting was used between the glass surfaces and the loading rings. The failure load was recorded in each test. The failure stress for ring-on ring (S_{RoR}) of a square plate was calculated using [3.17]

$$S_{RoR} = \frac{3P}{2\pi t^2}\left[(1-\nu)\frac{{D_S}^2 - {D_L}^2}{2D^2} + (1+\nu)\ln\frac{D_S}{D_L}\right] \tag{3.2}$$

and

$$D = \frac{0.5(l_1 + l_2)}{0.90961 + 0.12652\frac{t}{D_S} + 0.00168\ln\frac{0.5(l_1 + l_2) - D_S}{t}} \tag{3.3}$$

where P is the failure force, t is thickness, ν is Poisson's ratio, D_S is the support ring diameter, D_L is the loading ring diameter, and l_1 and l_2 are the lengths of the sides of the plate. For S_{RoR} testing, $t = 3.3$ mm, $D_L = 15$ mm, $D_S = 35$ mm, and $l_1 = l_2 = 50$ mm. A schematic of the ring-on-ring bend test fixture is shown in Fig. 3.3.

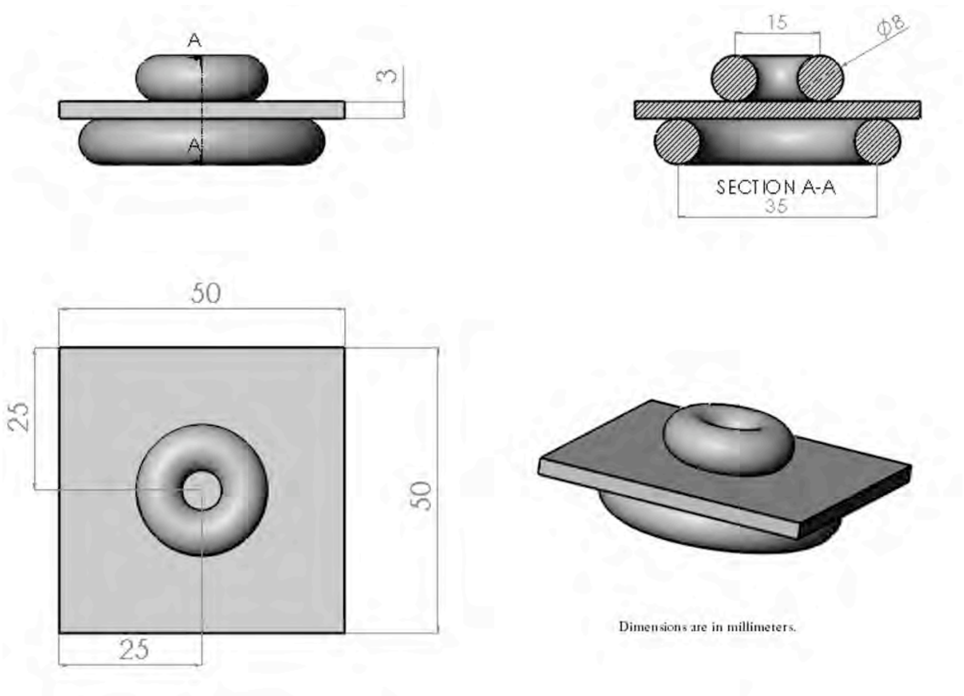

Figure 3.3. Schematic of the ring-on-ring bend test configuration. Dimensions in mm.

3.3. Strengthening

Even without process optimization, the uniaxial 4-pt-bend failure stress increased by approximately 65% and the equibiaxial failure stress increased by approximately 25%. These differences are shown in Figs. 3.4-3.5 and are statistically significant.

Four-point bending of the entire tile is usually an effective test to assess strength limits caused by edge-located flaws; the fracture response of the untreated tiles (14 of 15) is an indication of that. But as shown in Fig. 3.4, none of the 15 arc-lamp-processed glass tiles had failure initiate at an edge; failure always began at the surface. This change in failure mechanism resulted in the observed 65% increase in failure stress of the treated glass. The employed arc-lamp-heating served to "heal" edge-located flaws as evidenced by the "rounding" that was produced at the chamfer (see Fig. 3.6). This is the same effect that fire polishing produces.

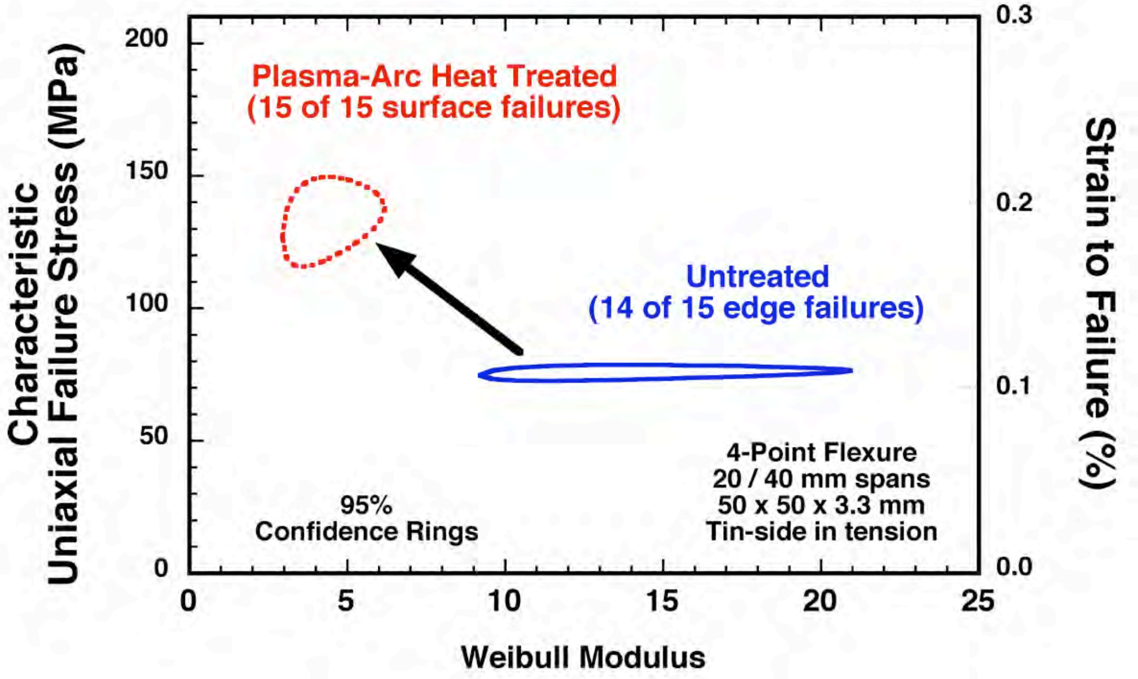

Figure 3.4. Comparison of uncensored 4-pt-bend failure stress distributions of untreated and plasma-arc-lamp heat-treated soda-lime silicate glass. For a loading and support span of 20 and 40 mm, respectively, the effective length, $L_e = L_S((m+2)/(m+1))$, is 42.9 mm for a Weibull modulus of 13, and the effective area is 516 mm^2 for a Weibull modulus of 3 [3.18].

Equibiaxial flexure of entire tiles is typically the most effective way to examine strength limiting caused by surface-located flaws. As shown in Fig. 3.5, the strength of the arc-lamp-irradiated glass increased by approximately 25%. Preliminary fractography was inconclusive, but examinations of the strength-limiting flaws in some of the heat-treated tiles revealed a smaller flaw size (and mirror), which is associated with higher failure stress.

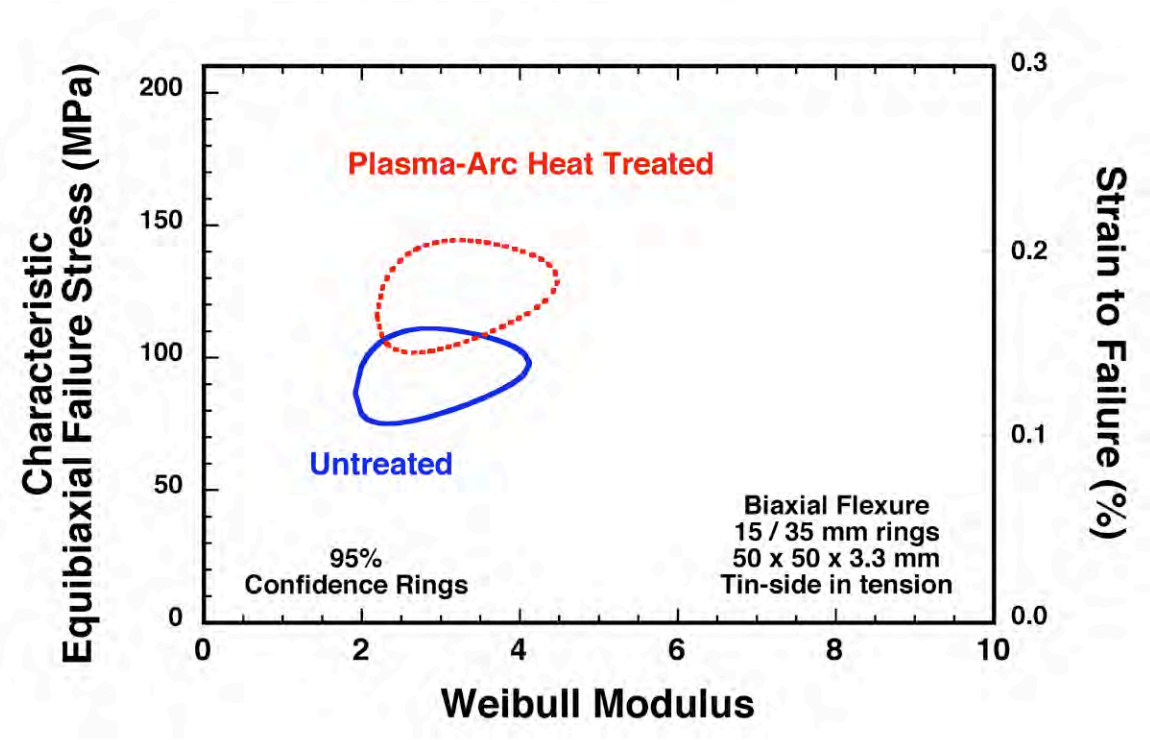

Figure 3.5. Comparison of uncensored ring-on-ring bend failure stress distributions of untreated and plasma-arc-lamp heat-treated soda-lime silicate glass. The effective area is 629 mm^2 for a Weibull modulus of 3 with this specimen and fixture size [3.17].

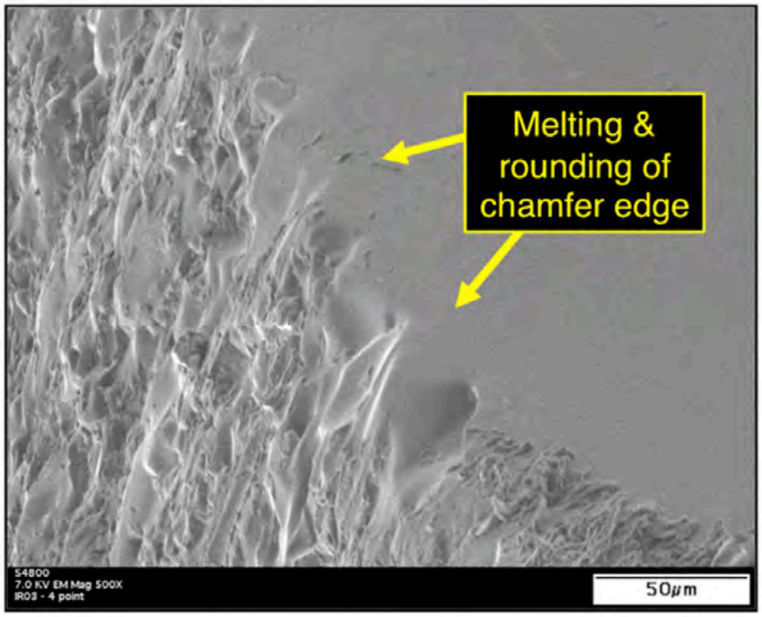

Figure 3.6. High magnification images of a chamfered edge of a 4-pt-bend specimen that was plasma-arc heat treated showing localized softening and edge rounding which ultimately caused strengthening and a change in the strength-limiting flaw location.

One or more mechanisms could be contributing to the observed strengthening. Rounding of crack tips [3.4], filling-in and partial healing of surface flaws [3.5], and the introduction of surface-located residual compressive stresses [3.19] are possibilities. These are illustrated in Fig. 3.7. The "rounding" observed in Fig. 3.6 suggests that the filling-in or partial healing or fire polishing mechanism is operative. The activity of that mechanism is significant and important because it suggests that plasma-arc-heating may be able to increase the strength of even the weakest samples in a glass sample population whereas commonly used chemical strengthening treatments may not be able to [3.20].

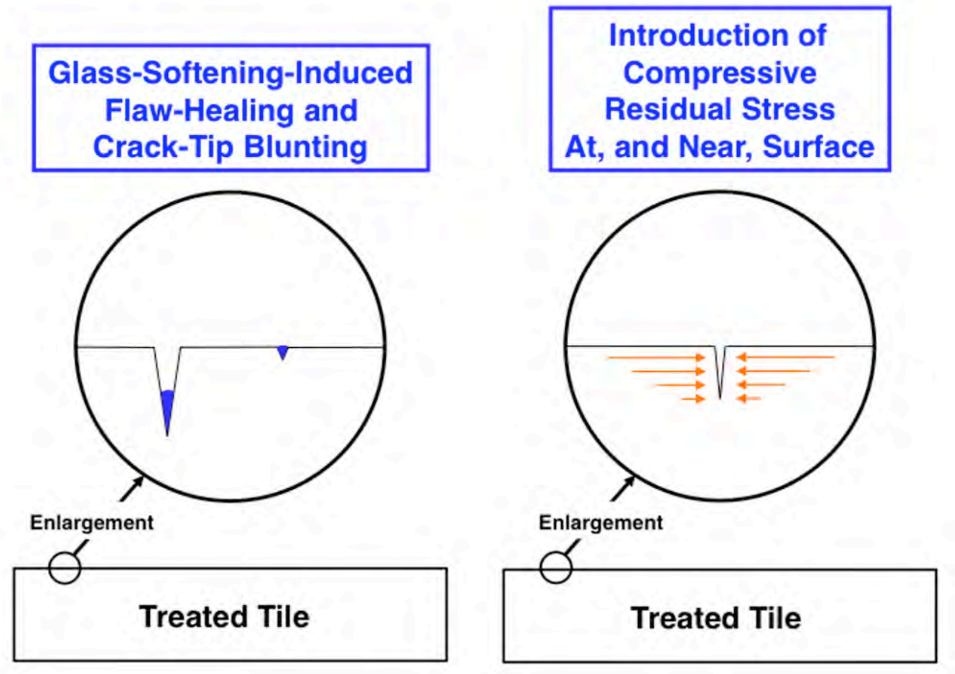

Figure 3.7. One of two mechanisms (or both) likely causes the observed strengthening.

To examine what effect the plasma arc heating could have on Hertzian contact damage, spherical indentation was done on the irradiated surface of a treated tile and compared to that of an untreated tile. The differing responses are shown in Fig. 3.8. The greater amount of secondary cracking (at a lower maximum force) suggests that the plasma arc heating introduced residual stresses, and that residual stresses were relieved by it. Based on this preliminary examination, it appears that the plasma arc heat treatment is effective at improving bend strength but it may not improve contact damage resistance. Future work should examine this further.

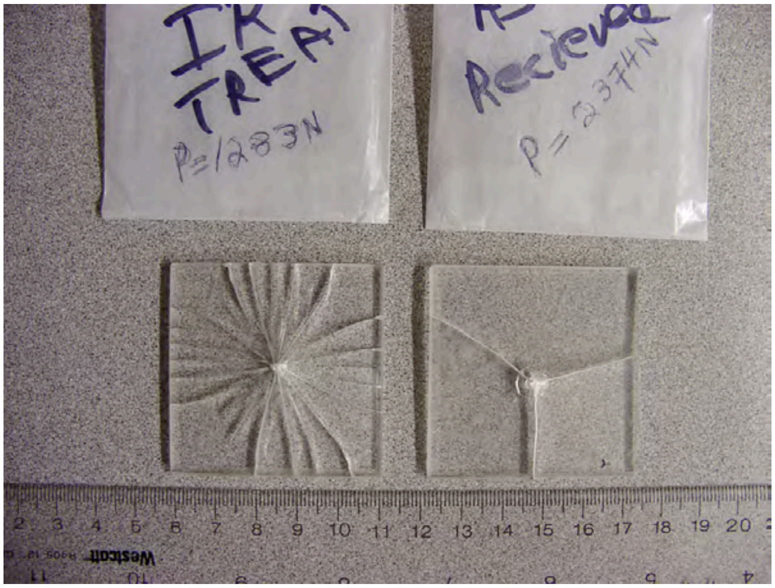

Figure 3.8. Cracking response from Hertzian indentation of (left) arc-lamp processed tile and (right) untreated tile.

3.4. Patterning

It was anecdotally observed during plasma arc heat treatment that opaque and high emissivity marks (permanent pen) on the glass surface affected the glass surface as a consequence of the heat treatment. The marks locally heat the glass surface that is under it. To study this effect in more detail, an arbitrary pattern of graphite ink was screen printed on a glass slide as shown in Fig. 3.9. The glass tile was then arc lamp processed with the same conditions that the tiles were processed for the above strength testing. The resulting pattern is shown in Fig. 3.10 with the produced lettering having a height of approximately 15 µm. The intent of the limited amount of patterning study was to show that plasma arc lamp heating can be used to put permanent marks on a glass surface.

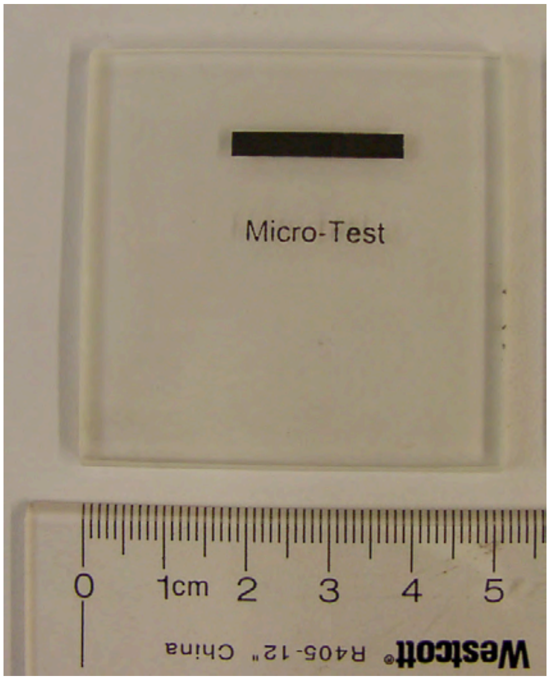

Figure 3.9. Screen-printed pattern deposited on glass tile prior to plasma-arc irradiation.

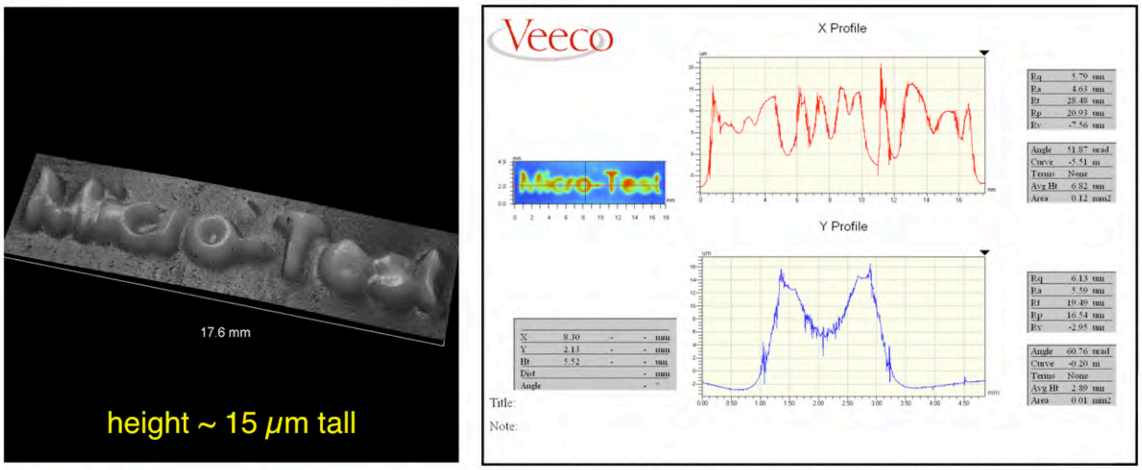

Rq	5.79	um
Ra	4.63	um
Rt	28.48	um
Rp	20.93	um
Rv	-7.56	um

Angle	51.87	urad
Curve	-5.51	m
Terms	None	
Avg Ht	6.82	um
Area	0.12	mm2

X	8.30	-	-	mm
Y	2.13	-	-	mm
Ht	5.52	-	-	um
Dist			-	mm
Angle			-	°

Title:

Note:

Rq	6.13	um
Ra	5.59	um
Rt	19.49	um
Rp	16.54	um
Rv	-2.95	um

Angle	60.76	urad
Curve	-0.20	m
Terms	None	
Avg Ht	2.89	um
Area	0.01	mm2

Figure 3.10. Produced pattern after plasma-arc lamp irradiation.

3.5. Summary

The flexure strength of a soda-lime silicate glass increased by heat-treating it with a high-intensity plasma-arc lamp. Even without process optimization, the equibiaxial failure stress increased by approximately 25% and uniaxial 4-pt-bend failure stress increased by approximately 65%. The strengthening was statistically significant. The arc-lamp heat-treatment caused flaw healing that was responsible for the observed strengthening, and that mechanism is likely the same produced in fire polishing. An associated effect was the change-in-location of the strength-limiting flaws in the 4-pt-bend tiles where failure initiation occurred on the gage section surface for treated glass but it occurred at a gage section edge for the untreated. More work and optimization is planned, but plasma-arc heat treating has demonstrated attractiveness for its potential to strengthen glass.

3.6. References

[3.1] M. E. Nordberg, E. L. Mochel, H. M. Garfinkel, and J. S. Olcott, "Strengthening by Ion Exchange," *J. Am. Cer. Soc.,* 47:215-219 (1964).

[3.2] P. C. Fletcher and J. J. Tillman, "Effect of Silicone Quenching and Acid Polishing on the Strength of Glass," *J. Am. Cer. Soc.,* 47:379-382 (1964).

[3.3] J. M. Barsom, "Fracture of Tempered Glass," *J. Am. Cer. Soc.,* 51:75-78 (1968).

[3.4] R. E. Mould, "Strength and Static Fatigue of Abraded Glass Under Controlled Ambient Conditions: III, Aging of Fresh Abrasions," *J. Am. Cer. Soc.,* 43:160-167 (1960).

[3.5] B. D. Fabes and D. R. Uhlmann, "Strengthening of Glass by Sol-Gel Coatings," *J. Am. Cer. Soc.,* 73:978-988 (1990).

[3.6] R. J. Hand, F. H. Wang, B. Ellis, and A. B. Seddon, "Glass Strengthening Using Ormosil Polymeric Coatings," *J. Sol-Gel Sci. Tech.,* 13:695-699 (1998).

[3.7] M. R. Sozanski and A. K. Varshneya, "Strengthening of Glass Tubes and Containers by Flame-Sprayed Glazing," *Am. Cer. Soc. Bull.,* 66:1630-1634 (1987).

[3.8] I. N. Yashchishin, T. B. Zheplinskii, D. Yu. Matskyavichus, and V. D. Kazakov, "Strengthing Glass Containers by a Thermochemical Flame Method," *Glass Cer.,* 46:7-9 (1989).

[3.9] P. Zuccelli, "Oxycombustion for Glass Conditioning and Fire Polishing," *Int. Glass J.,* 133:26-31 (2004).

[3.10] J. D. K. Rivard, C. A. Blue, A. Sabau, E. K. Ohriner, G. M. Ludtka, T. N. Tiegs, and J. J. Stiglich, "The Use of High Density Infrared Heating for Surface Modification/Coatings Processes," *Proc. 18th Int. Conf. Surf Mod. Tech.*, 139-146 (2006).

[3.11] A. A. Wereszczak, “Elastic Property Determination of WC Spheres and Estimation of Compressive Loads and Impact Velocities That Initiate Their Yielding and Cracking,” *Cer. Eng. Sci. Proc.*, [7], 27:211-223 (2006).

[3.12] R. R. Tummala and B. J. Foster, "Strength and Dynamic Fatigue of Float Glass Surfaces," *J. Am. Cer. Soc.,* 58:156-157 (1975).

[3.13] R. Akcakaya, S. Gulati, and J. R. Varner, "Fatigue Behavior of Surface Flaws on Air vs. Tin Side of Soda–Lime–Silica Float Glass"; Paper T4.3 in *Glass in the New Millennium: Challenges and Break-Through Technologies*, Proceedings of the ICG Annual Meeting 2000 (Amsterdam, The Netherlands, May 15–17, 2000), National Committee Netherlands Glass Industry (NCNG), 2000.
[3.14] M. K. Krohn, J. R. Hellmann, D. L. Shelleman, C. G. Pantano, and C. E. Sakoske, "Biaxial Flexure Strength and Dynamic Fatigue of Soda-Lime-Silica Float Glass," *J. Am. Cer. Soc.,* 85:1777-1782 (2002).
[3.15] A. A. Wereszczak, K. E. Johanns, T. P. Kirkland, C. E. Anderson, Jr., T. Behner, P. Patel, and D. Templeton, "Strength and Contact Damage Responses in a Soda-Lime-Silicate and a Borosilicate Glass," Paper FP-05, 25th Army Sci. Conf., Orlando, FL, Nov. 27-30, 2006.
[3.16] "Standard Test Method for Flexural Strength of Advanced Ceramics at Ambient Temperature," ASTM C1161, Vol. 15.01, 2008, ASTM International, West Conshohocken, Pennsylvania.
[3.17] "Standard Test Method for Monotonic Equibiaxial Flexure Strength of Advanced Ceramics at Ambient Temperature," ASTM C1499, Vol. 15.01, 2008, ASTM International, West Conshohocken, Pennsylvania.
[3.18] G. D. Quinn, "Weibull Strength Scaling for Standardized Rectangular Flexure Specimens," *J. Am. Cer. Soc.,* 86:508-510 (2003).
[3.19] D. J. Green, "Compressive Surface Strengthening of Brittle Materials by a Residual Stress Distribution," *J. Am. Cer. Soc.,* 66:807-810 (1983).
[3.20] W. C. LaCourse, "How Surface Flaws Affect Glass Strength," *Glass Ind.*, [7] 68:14-18 (1987).

4. THRESHOLD PRESSURE

4.1. Basis for Inquiry

It is desirable to study Hertzian indentation responses because the stress state it generates is similar to that of a ballistic impact. This subsection constitutes the first examination to link Hertzian indentation response to ballistic response. It would be quite significant if such a link can be established because (inexpensive, quick, and simple) Hertzian indentation testing of armor ceramics could be used to generate ballistic model input parameters, and ballistic performance could be predicted. This would enable armor ceramic manufacturers to improve their materials, and enable end-users to more readily compare and rank candidate materials for their application.

This subtask was an initial study to evaluate the usefulness of Hertzian indentation experiments as a means to characterize the mechanical behavior of high strength ceramic materials. Of specific interest is the ability of Hertzian indentation to provide the constitutive response for the determination of material model constants and/or model validation. Because ceramic materials are so strong in compression, it is difficult, expensive and time consuming to perform the laboratory and ballistic tests needed to obtain constitutive model constants. Hertzian indentation tests offer a potentially attractive alternative. Although it is probably not feasible to determine the entire constitutive response from Hertzian indentation tests it may be possible to determine a significant portion of the response and significantly reduce the number of laboratory tests that are currently required. Desirable features of indentation tests are the high stresses and permanent deformation produced in the material, they are simple, inexpensive and quick, and sample preparation and postmortem analysis are relatively straightforward and inexpensive. Furthermore, recent advancements in the test technique now allow for indentation stresses of over 30 GPa to be generated. Stresses of this magnitude are similar to those produced during ballistic impact and/or plate impact. The disadvantage of Hertzian indentation is that the stresses, strains, and pressures are not explicit outputs of the experiment. The output is generally presented in the form of a force-displacement relationship that represents the applied force on the indenter as a function of the ceramic displacement. This requires the constitutive response to be inferred by performing computations and comparing the force-displacement results to the experiment.

There is also a strong desire to use Hertzian indentation to rank the ballistic performance of ceramics, specifically interface defeat. Historically the ballistic performance of ceramic materials is determined from ballistic tests. Ceramics are placed in specific target configurations, impacted by specific projectiles and ranked by their ability to defeat the projectile. This is also the procedure used to determine the dwell-penetration transition velocity [4.1]. This is a very expensive and time-consuming process. Hertzian indentation, again, offers a very attractive alternative if a ranking procedure can be determined.

This effort used computations, and test results, in an attempt to determine if Hertzian indentation can be used to (1) determine and/or validate Johnson-Holmquist-Beissel, JHB, constitutive model response, and (2) provide a ranking procedure for ranking the ballistic performance (specifically, the transition from dwell to penetration) of ceramics.

4.2. Computed Results for Hertzian Indentation Geometry

The initial geometry used for the Hertzian indentation computations in shown in Fig. 4.1. A spherical diamond indenter is used to produce indentation into silicon carbide (SiC). The indenter is diamond with a diameter, D = 0.5 mm. The diamond indenter is modeled as strictly elastic with a Young's modulus and Poisson's ratio of, $E_i = 1141$ GPa and $\nu_i = 0.07$ respectively. The SiC sample is $t = 1.0$ mm thick, with a diameter of, D = 3.0 mm and is modeled using the JHB model and constants as previously presented [4.2]. It should be noted that both the experiment and the JHB model are for SiC-B, a specific form of silicon carbide manufactured by BAE systems, Advanced Ceramics Division (formerly CERCOM). It should also be noted that the JHB model for SiC has been used to successfully model several different impact experiments including plate impact, spall, interface defeat, dwell, penetration, perforation, and Hertzian indentation [4.2]. The JHB strength model for SiC is shown in Fig. 4.2 and is used for all of the following computed results unless otherwise noted.

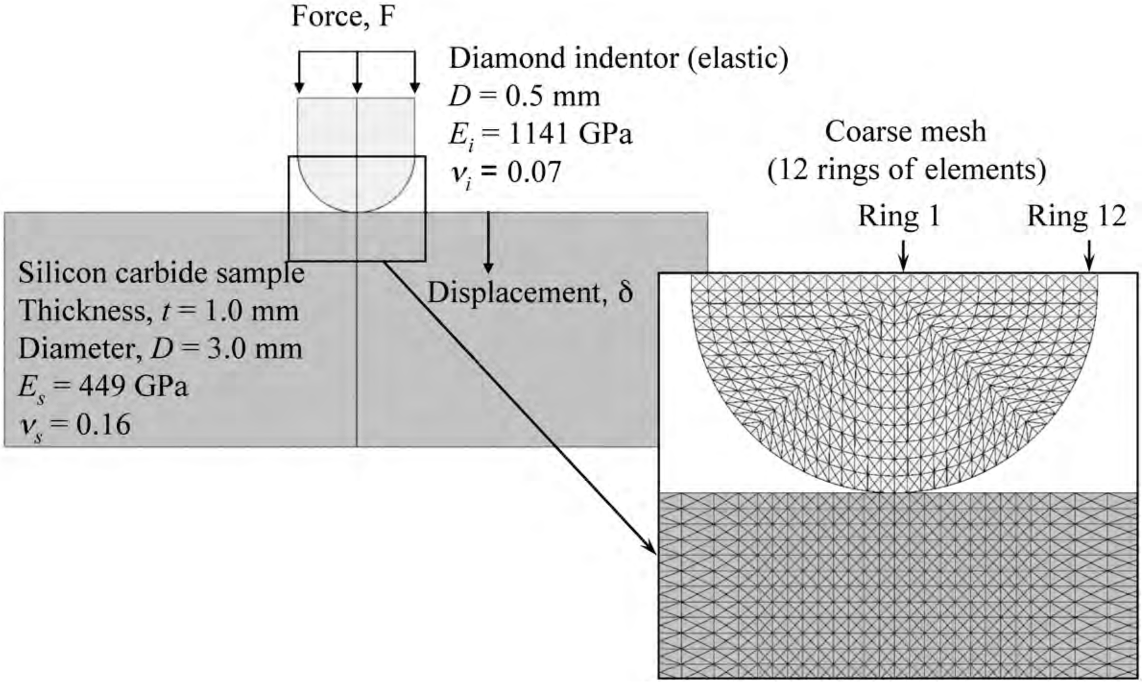

Figure 4.1. Initial 2D Hertzian indentation geometry.

4.2.1 Computational Approach

This subsection is provided to establish a computational approach for computing Hertzian indentation. The EPIC Lagrangian finite element computer code [4.3] is used for all the computed results and all are performed in the 2D axisymmetric configuration. The EPIC code is an explicit finite element hydrocode developed primarily to simulate dynamic events such as ballistic impact and penetration. Here the code is used to simulate indentation, a quasi-static event. The computations use a velocity field applied to the rear surface of the indenter to produce the indentation process. A velocity of 1 m/s produce computed results within a reasonable computing time without introducing any significant inertial effects. All the computed results use a 1 m/s velocity field applied gradually to the rear surface of the indenter.

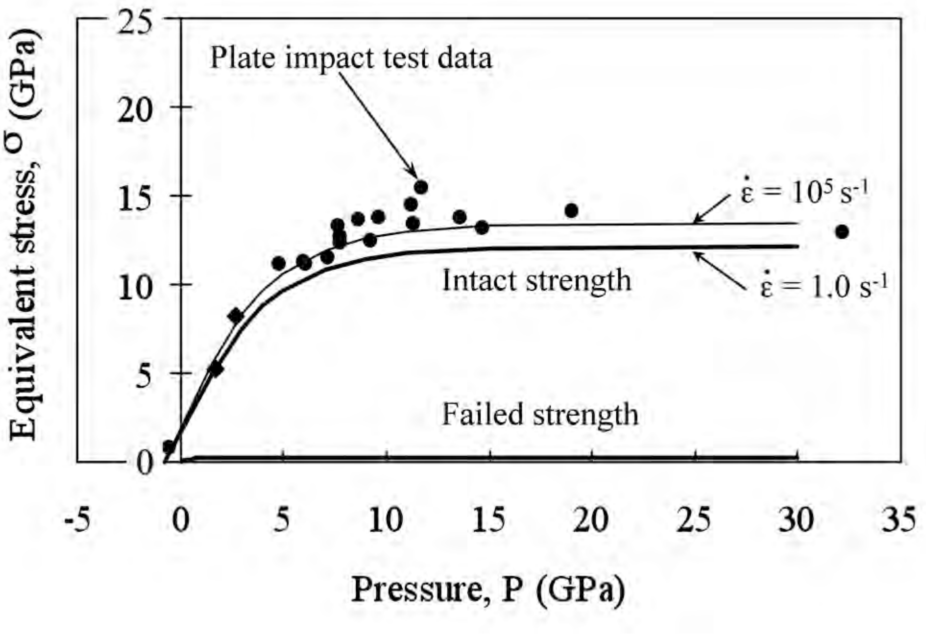

Figure 4.2. The JHB strength model for silicon carbide.

The effect of using contact and finite elements to represent the indentation process is presented in Fig. 4.3. Here the effect of using a series of elements to represent a spherical surface is clearly shown. As the indentation process proceeds new elements come in contact with the surface creating a larger surface area. The larger surface area requires a larger force to continue the indentation process that produces a discontinuity in the force-displacement curve. It is important to know that this response is a result of representing a spherical surface by a series of flat surfaces and not the constitutive response. It is also important to note that this effect is reduced as the mesh is refined. Figure 4.4 shows the indentation response for four meshes, a coarse mesh (12 rings of elements that represent the indenter, also shown in Fig. 4.1), a medium mesh (24 rings of elements), a fine mesh (48 rings of elements) and a very fine mesh (96 rings of elements). For clarity, the responses for the four meshes are also shown separately, each separated by $\delta = 1.5$ μm. It is clear that using 12 rings of elements produces distinct cusps in the force-displacement response. When 24 rings are used the response is much smoother and when 48 and 96 rings are used the solutions become nearly identical. Based on these results, a medium mesh is used for all of the following computations unless otherwise noted.

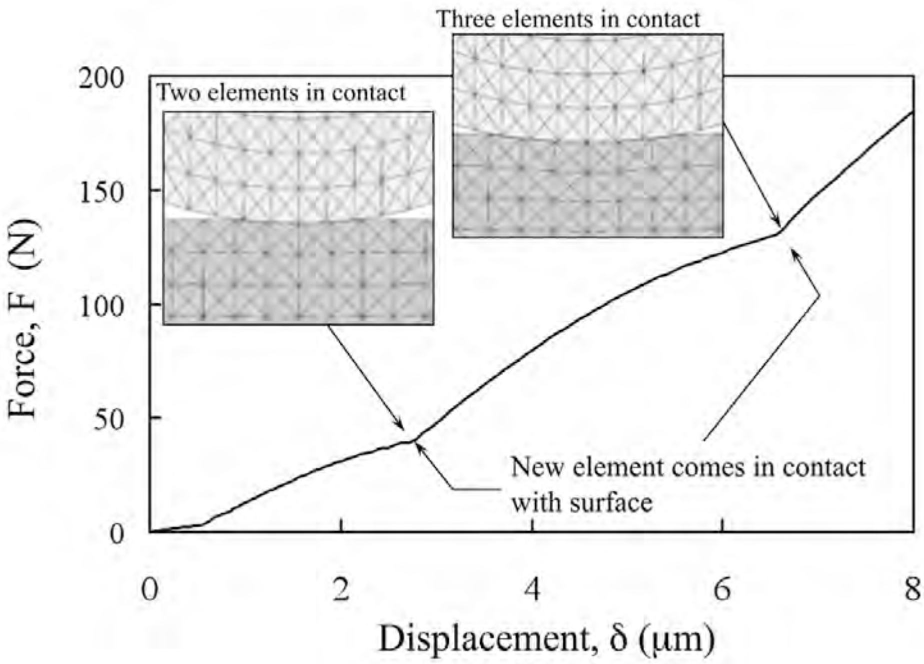

Figure 4.3. The effect of using contact and finite elements when computing the response of Hertzian indentation.

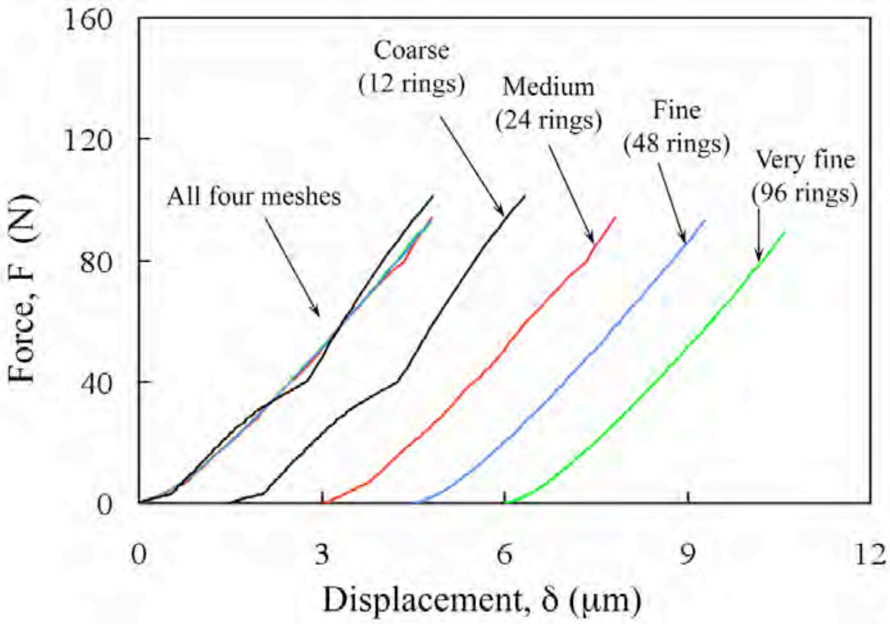

Figure 4.4. The effect of mesh refinement when computing the response of Hertzian indentation. The responses are also shown with a 1.5 μm offset for clarity.

To provide a measure of the accuracy of the finite element approach it is of interest to compare the computed result to the elastic analytic solution. There is a closed form solution for the response of two elastic solids in contact. This analysis was first presented by Hertz [4.4] and has been reproduced by Johnson [4.5]. The assumptions are the following:

1. the surfaces are continuous and non-conforming: $a \ll R$,
2. the strains are small: $a \ll R$,
3. each solid is considered an elastic half-space: $a \ll R_{1,2}$, $a \ll l$, *and*
4. the surfaces are frictionless,

where a is the contact radius, R is the relative radius of curvature, R_1 and R_2 are the radius of curvature of each of the two bodies and l is the sample thickness and lateral dimension. Using these assumptions the elastic force-displacement relationship is

$$F = \left[\frac{4a}{3}\right]\left[\frac{E_s}{1-\nu_s^2}\right]\delta \tag{4.1}$$

where F is the force, δ is the displacement at the center of the indenter-specimen interface, and E_s and ν_s are Young's modulus and Poisson's ratio of the sample respectively. The contact radius is given by the relationship

$$a = \left[\frac{3FR}{4E^*}\right]^{\frac{1}{3}} \tag{4.2}$$

where R is the radius of the indenter and E^* is the relative Young's modulus and is given by the relationship

$$\frac{1}{E^*} = \frac{1-\nu_i^2}{E_i} + \frac{1-\nu_s^2}{E_s} \tag{4.3}$$

where ν_i and E_i are Poisson's ratio and Young's modulus of the indenter respectively.

Using Eqn. (4.1-4.3), the elastic constants for the diamond indenter, $\nu_i = 0.07$, $E_i = 1141$ GPa, the elastic constants for the SiC sample, $\nu_s = 0.16$, $E_s = 449$ GPa and the indenter radius, R = 0.25 mm, the elastic analytic force-displacement relationship is determined and is given by

$$F = 11.48\delta^{1.5} \tag{4.4}$$

where F is in Newton's and δ is in µm. This relationship is presented graphically in Fig 4.5 including the computed solutions for a thickness of $t = 1$ mm and for $t = 3$ mm. As the thickness, t, of the indentation specimen increases the indentation displacement increases. The computed elastic force-displacement results are in very good agreement with the analytic solution.

Figure 4.6 presents stress contours produced from the computed elastic solution for a force of 57 N. A comparison of the computed elastic solution to the analytic solution is given in Table 4.1. The computed solution is in good agreement with the contact radius, a, the maximum shear location, z, the indentation depth, δ, the maximum axial stress, σ_z, the maximum hoop stress, σ_θ, the maximum radial stress, σ_r, and the maximum equivalent stress, $\sigma = 2\tau$. The maximum radial tensile stress is not in good agreement. This is caused by the discontinuity in the radial stress that occurs on the very edge of the contact surface. The radial stress is compressive under the indenter and rapidly decreases, eventually going into tension at the edge of the indenter. Discontinuities are difficult to resolve with a finite element method as the discontinuity becomes "smeared", although the results improve as the mesh is refined.

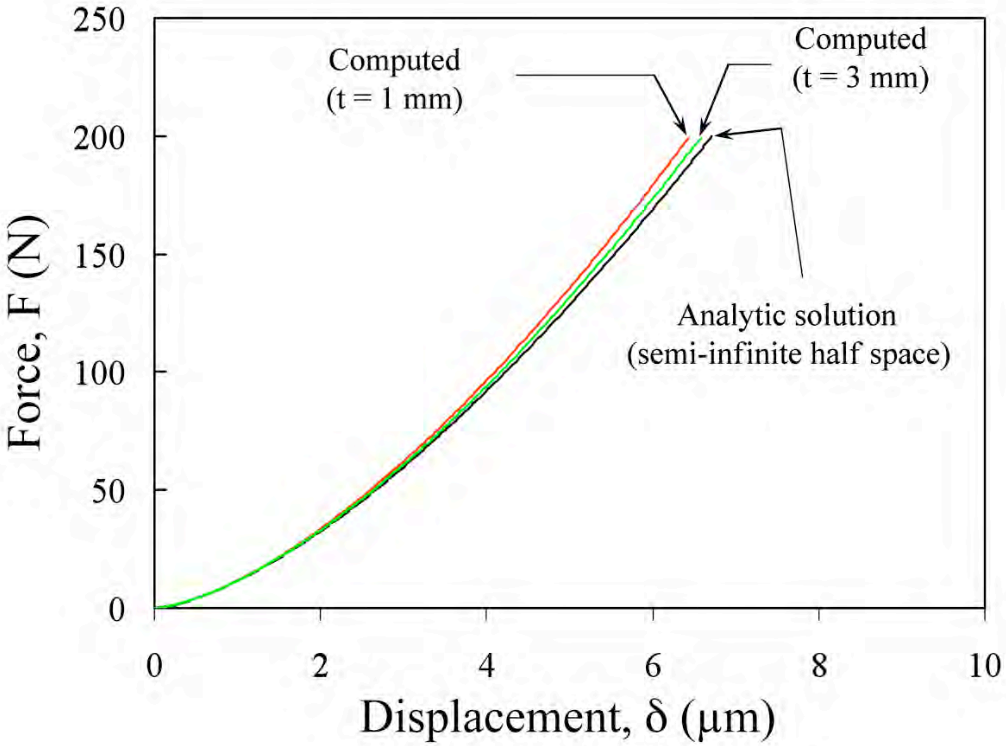

Figure 4.5. Comparison of the computed and analytic elastic solutions.

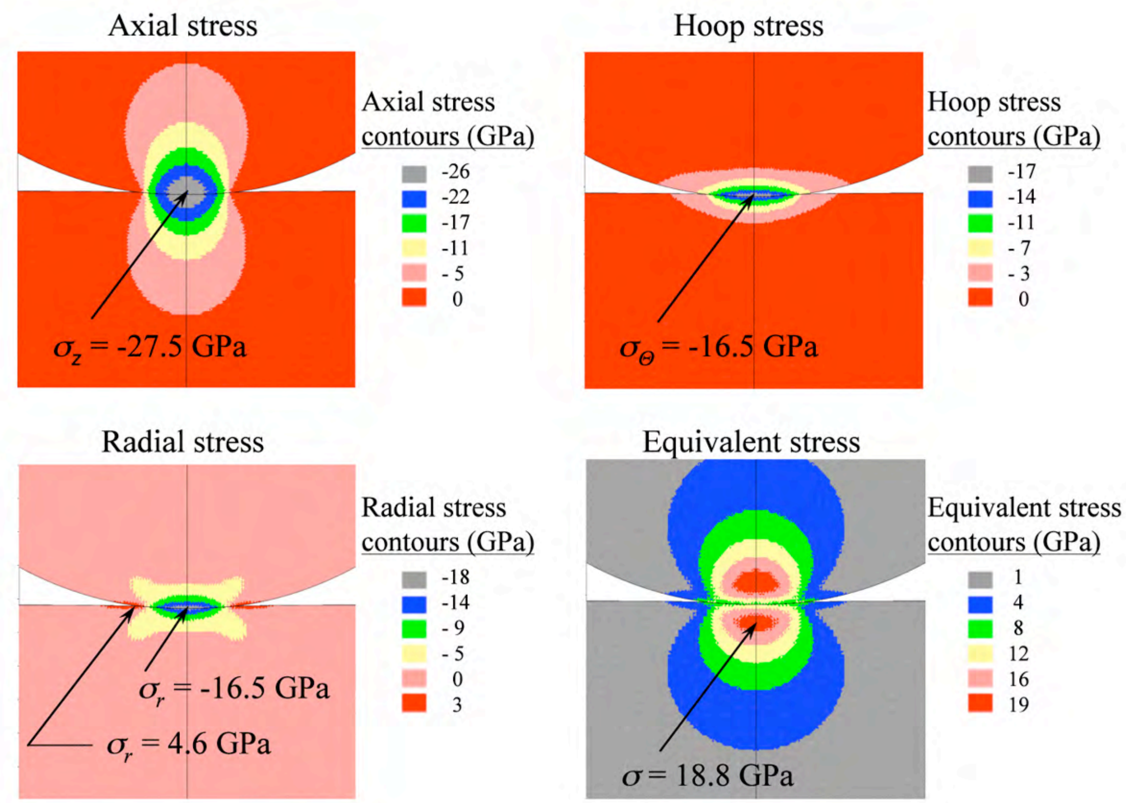

Figure 4.6. Computed elastic stress contours from a 57 N applied load.

Table 4.1. Comparison of the analytic and computed elastic solutions. The computed results are from a medium mesh.

	Analytic solution	Computed solution
Applied force, F (N)	57	57
Indenter radius, R (mm)	0.25	0.25
Sample thickness, t (mm)	infinite	1.0
Sample diameter, D (mm)	infinite	3.0
E* (GPa)	329	329
Contact radius, a (µm)	32	32
Maximum shear location, z (µm)	14	14
z/a	0.44	0.44
Indentation depth, δ (µm)	2.90	2.83[#]
Maximum axial stress, σ_z (GPa)	-26.7	-27.5
Maximum hoop stress, σ_θ (GPa)	-17.6	-16.5
Maximum radial stress, σ_r (GPa)	-17.6	-16.5
Maximum tensile radial stress, σ_r (GPa)	6.1	4.6[&]
Maximum equivalent stress, $\sigma = 2\tau$ (GPa)	18.3	18.8

[#] Indentation depth increases as the sample thickness increases

[&] Tensile radial stress increases as the mesh is refined

4.2.2 Sensitivity of Hertzian Indentation to changes in the JHB Strength Model

If Hertzian indentation experiments are to be helpful in determining constitutive model parameters, or validation of model parameters, it is important to know the effect the model parameters have on the indentation response. If big changes in the model parameters (material strength) produce small changes in indentation response the possibility for indentation tests to be helpful is less likely. It is also important to know the magnitudes of the stresses, pressures, and strains produced in the indentation test so it can be determined where the model is being exercised. Computations using the JHB strength model, normalized to a strain rate of 1.0 s^{-1}, are used to provide insight into these issues. Computed results for a peak load of 200 N are presented in Figs. 4.7 and 4.8 (here a coarse mesh is used). Figure 4.7 shows the plastic stain contours under the indenter at four points during the loading process. The solid circles represent the maximum equivalent stress and pressure produced at each of the four loads (10 N, 53 N, 89 N and 200 N). The equivalent stresses and pressures produced are very high (> 10 GPa) and the plastic strains exceed 6%. These magnitudes (of combined pressure and shear) have typically been attainable only by plate impact experiments, but here it appears that it is possible using Hertzian indentation. Figure 4.8 shows the change in the force-displacement response when the material strength is reduced by 20%. There is an approximate 1 to 1 correlation between the reduction in strength and the reduction in the force-displacement response.

These results are encouraging in that the stresses, pressures and strains produced from indentation are large and changes in material strength produce significant changes in the force-displacement response.

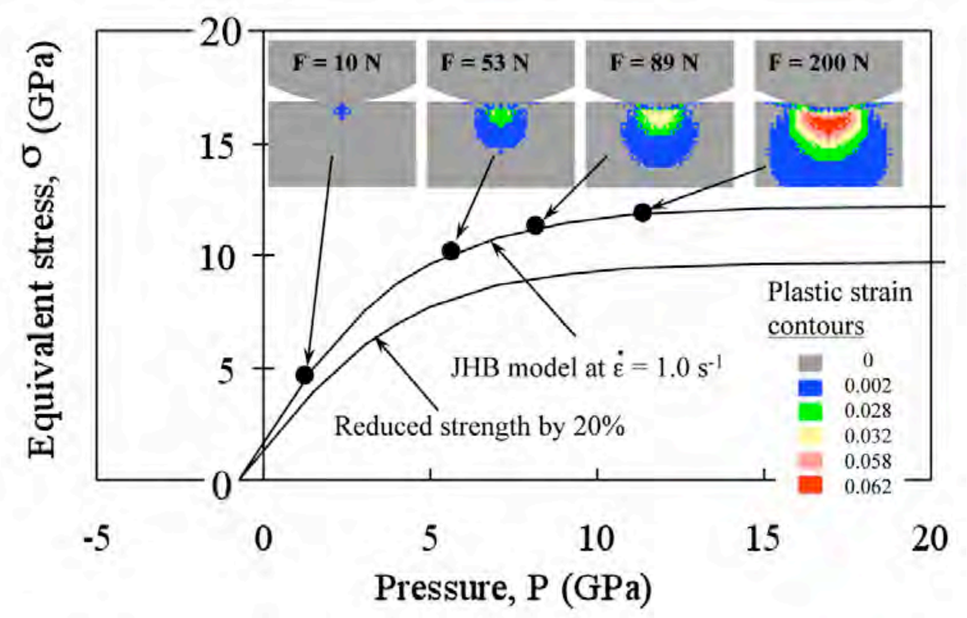

Figure 4.7. Computed indentation response for a peak load of 200 N. The maximum pressures and stresses are shown including the plastic stain contours at four points during the loading process.

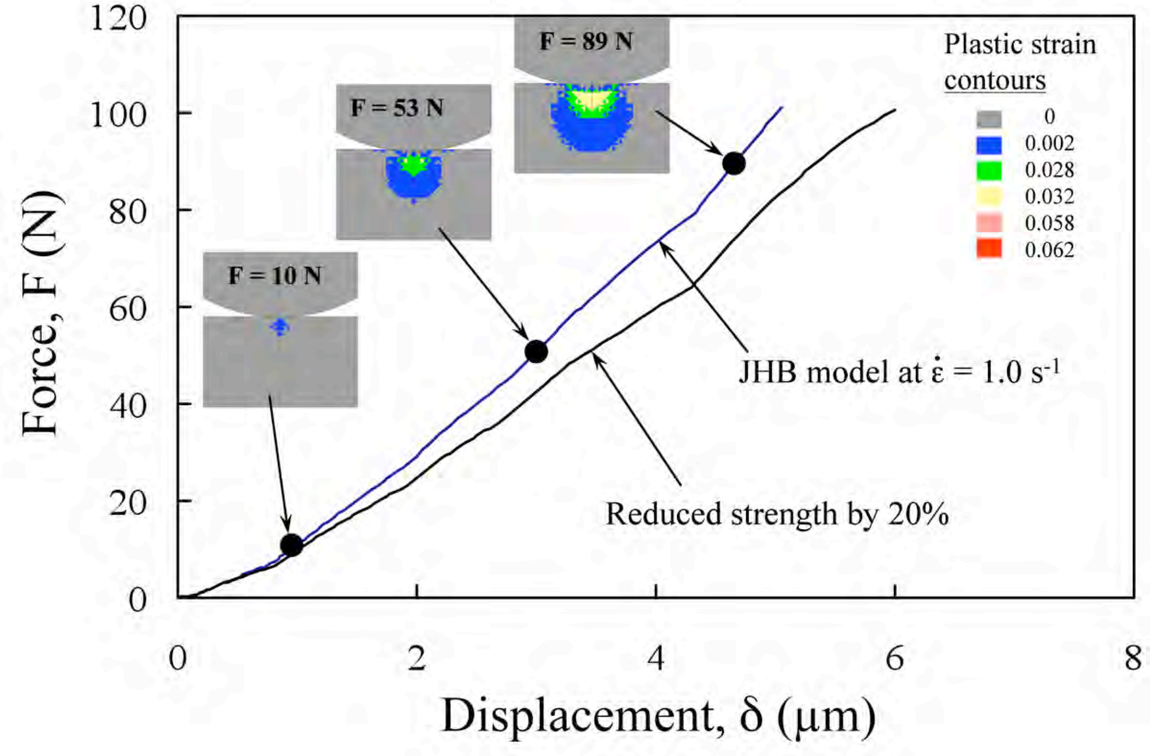

Figure 4.8. Computed force-displacement response showing the effect of a 20% reduction in strength.

4.2.3 Comparison to Test Data

Figure 4.9 presents experimental results (shown in red) for a diamond indenter onto a silicon carbide sample. The indenter has a radius of, R = 0.25 mm, and the sample is SiC-B manufactured by BAE systems, Advanced Ceramics Division, having a thickness of, t = 1 mm and the diameter is large. A maximum force of 200 N is applied to the indenter. The results appear smooth for both loading and unloading and a permanent displacement of approximately δ_p = 3 μm is produced. Computed results are also presented in Fig. 4.9. The result using the JHB model, at a normalized strain rate of $\dot{\varepsilon}$ = 0.001 s^{-1}, and a coarse mesh, produce a response that is significantly softer than the experiment, resulting in a permanent displacement of δ_p = 4.6 μm. Figure 4.10 presents a modified JHB strength model (shown in red) that matches the experimental force-displacement curve including the permanent displacement of δ_p = 3 μm as shown in Fig. 4.9. The modified model is significantly stronger (~ 25%) than the baseline JHB model and appears to correlate well to the plate impact data. It is not known why the indentation data appears so much stronger, or why it correlates so well to the plate impact data but possible explanations could be; errors in the indentation data (resulting from errors produced when subtracting out the machine compliance), errors in the baseline JHB model response, SiC is not strain rate sensitive, or the plate impact data (the Hugoniot stress) may more closely represent a quasi-static response than a dynamic response. This will require further research.

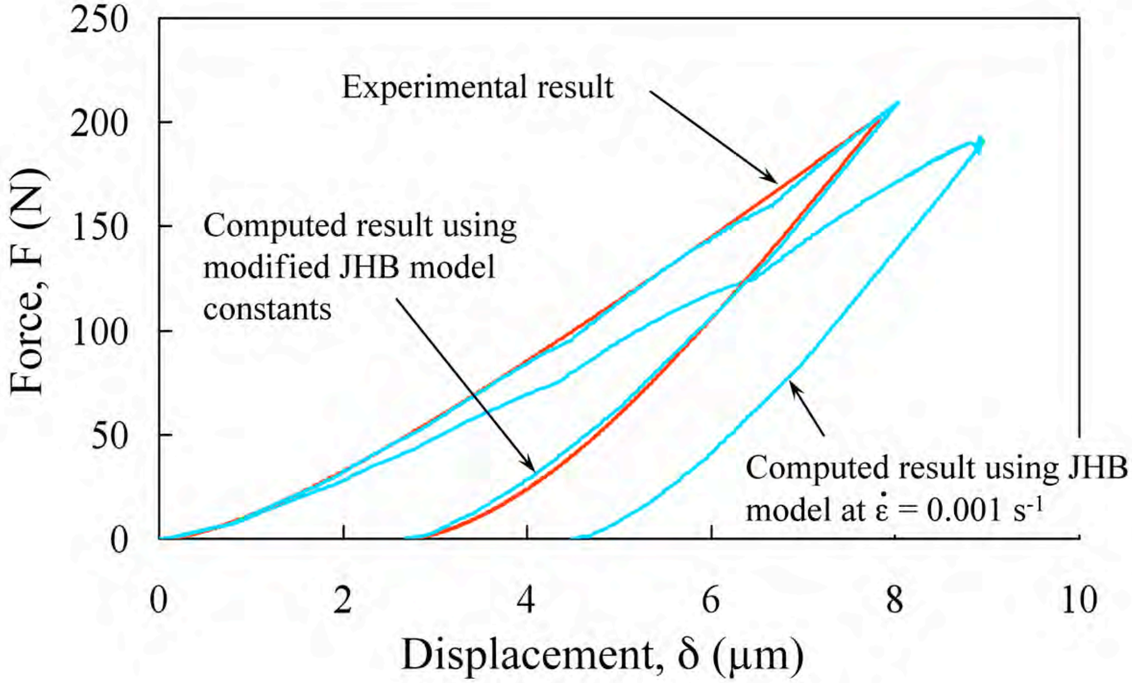

Figure 4.9. Hertzian indentation test data and computed results using the baseline JHB model at strain rate = 0.001 s^{-1} and with modified constants generated to match the test results.

The modified JHB model presented in Fig. 4.10 is used to compute the plastic strain evolution as presented in Fig. 4.11. The computation uses a very fine mesh such that there is good resolution of the plastic deformation. Experimentally it is very difficult to determine the onset of plastic deformation. Currently, the procedure uses a series of load-unload experiments. Each additional experiment loads the specimen to a slightly higher load. This cycle is continued until permanent deformation is detected. This load is defined as the "apparent yield" since yielding is inferred from the first detection of permanent displacement. For the experiment presented in Fig. 9 the first detection of plastic deformation occurred at a load of 25.6 N. The computed result shows the onset of plastic deformation to occur at 16.9 N and a permanent displacement of only δ_p = 0.007 μm. This may be beyond the accuracy of the experimental measuring technique. At a load of 26.7 N (close to the experimental apparent yield) the permanent displacement increases to δ_p = 0.030 μm, at 55.5 N the permanent displacement is δ_p = 0.289 μm and finally, at 74.7 N the permanent displacement is δ_p = 0.537 μm. Also shown in Fig. 4.11 are the force-displacement responses for the experiment and the computation that are nearly identical. Although Hertzian indentation appears to over estimate the load at which yielding occurs, the plastic strains are still very small (<0.005), and is probably still a reasonable approximation of initial yielding.

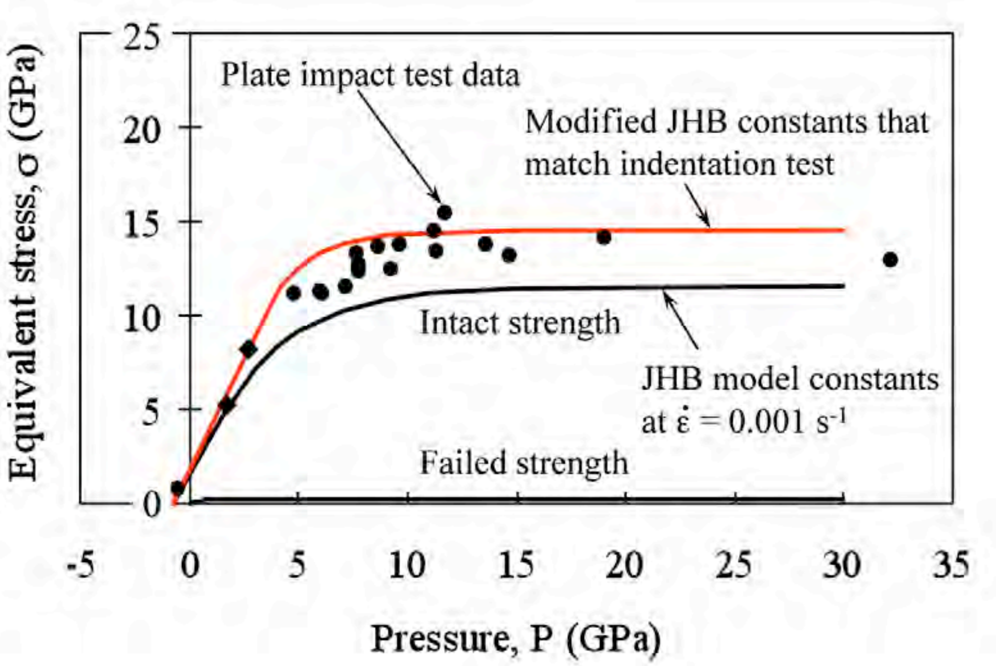

Figure 4.10. The baseline JHB model at strain rate = 0.001 s^{-1} and with modified constants generated to match the experimental response.

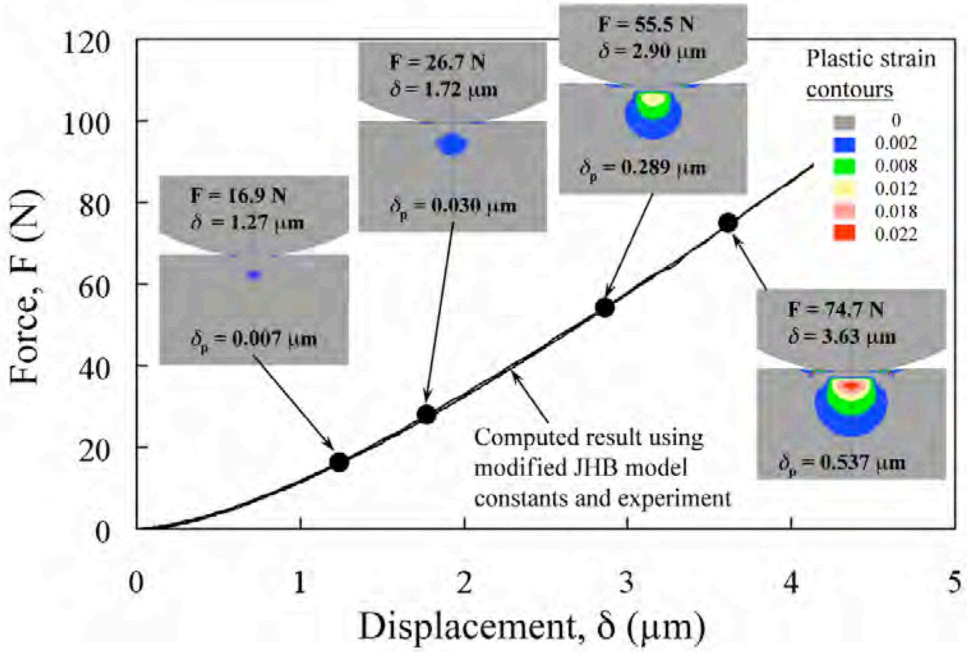

Figure 4.11. Computed and experimental force-displacement results for a Hertzian indentation test up to 100 N. Plastic strain contours including the permanent indentation after unloading, δ_d, are shown at four points during the loading process.

4.3. Computed Results for Hertzian Indentation and Ballistic Impact (Dwell)

The phenomena of ceramic dwell and interface defeat continue to be of major interest as they may provide significant improvement to armor systems. Ceramic dwell occurs when a high-velocity projectile impacts a ceramic target and flows out radially along the surface of the ceramic with no significant penetration. When the projectile is completely eroded at the ceramic surface it is referred to as interface defeat. As the impact velocity is increased, there is a point at which dwell is not maintained and penetration occurs; this impact velocity is called the dwell-penetration transition velocity and is a function of projectile material, projectile configuration, impact velocity, and target configuration. An example of dwell and interface defeat is presented in Fig. 4.12 [4.1]. Here an APM2 projectile impacts a thick block of AD995 alumina at 850 m/s. Images are presented at approximately t = 10, 30, 50, and 60 μs after projectile impact. The images clearly show the projectile flowing radially (dwelling) along the surface of the ceramic. The post mortem evaluation of the target showed no penetration into the ceramic (interface defeat).

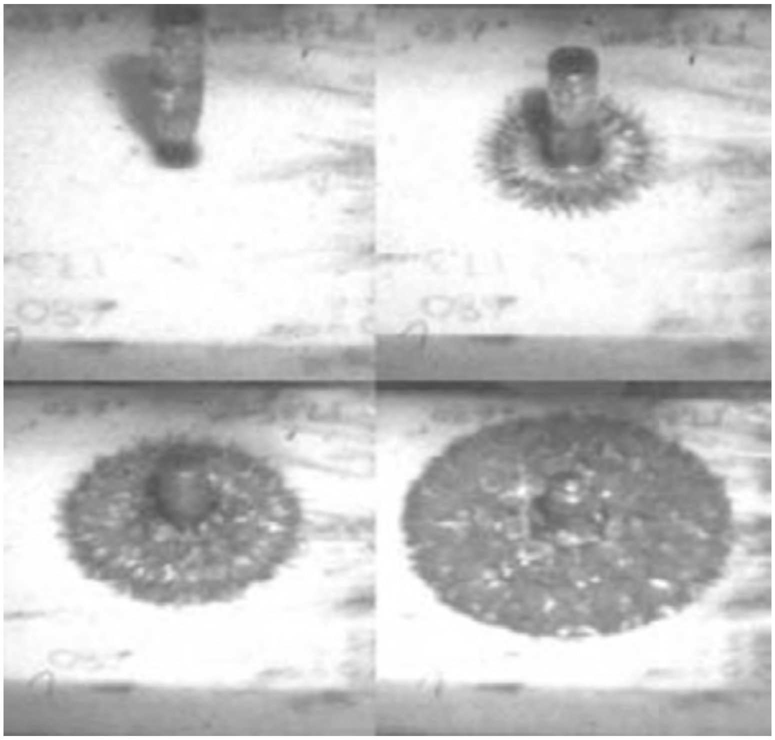

Figure 4.12. The APM2 projectile impacting a thick AD995 alumina target at 850 m/s. The impact event is shown at t = 10, 30, 50 and 60 μs after impact.

There is a strong desire to use Hertzian indentation to rank the ballistic response of ceramics, specifically the phenomenon of interface defeat. When a projectile exceeds a certain impact velocity there is a very distinct transition that occurs when the projectile ceases to dwell and begins to penetrate. This is an unstable condition and the transition is sharp and dramatic. It is not known if Hertzian indentation will also show this sharp, unstable transition and the author is not aware of any existing test data that show this response. If this unstable transition is produced in an indentation test, it may be possible to use the axial stress, measured at the transition, as a ranking parameter. If this unstable response is not produced, then other approaches might be possible, such as the energy absorbed from indentation (area under the loading curve minus the area under the unloading curve). The test data presented in Fig. 4.9 produces a peak axial stress of approximately 22 GPa (determined from the computation) which is very near the stress that transitions from dwell to penetration (~25 GPa) [4.1] but the load-unload curve appears to be very smooth and well behaved with no indication of any discontinuity. The computed result in Fig. 4.9 also is smooth and well behaved because no material has failed. If the load is increased to 220 N material begins to fail and the response becomes unstable, similar to the transition from dwell to penetration. It is not known if this would also occur in the Hertzian indentation experiment if the load was increased.

As a first step at evaluating the commonality between Hertzian indentation and interface defeat, a comparison of the stress and strain fields produced from each event is performed. Figure 4.13 presents the initial 2D geometries for a gold rod impacting a buffered silicon carbide target at 1300 m/s and for the Hertzian indentation configuration discussed previously. The copper buffer is used to attenuate the impact shock, produce gradual loading onto the ceramic surface and set up the conditions for dwell to occur [4.1]. The impact velocity of 1300 m/s was chosen because it is well below the transition velocity of approximately 1550 m/s [4.1]. For the Hertzian indentation configuration a load of 52 N was chosen such that the peak axial stress would be similar to that produced from dwell. Figure 4.14 presents a comparison of the axial stress, radial stress, equivalent stress and plastic strain fields produced from dwell and Hertzian indentation. The comparisons of the stress and strain fields are very similar with the exception of the tensile radial stress. There appears to be very little tensile radial stress produced during dwell, but significant tensile radial stress produced from Hertzian indentation. It is not known how this will affect the response as the loading is increased. This will be an area for future research.

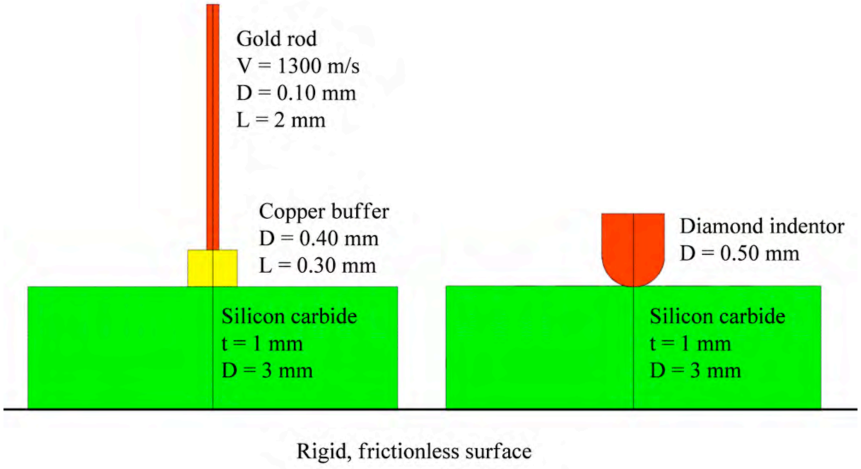

Figure 4.13. The initial 2D geometry for a ballistic impact configuration and for the Hertzian indentation configuration.

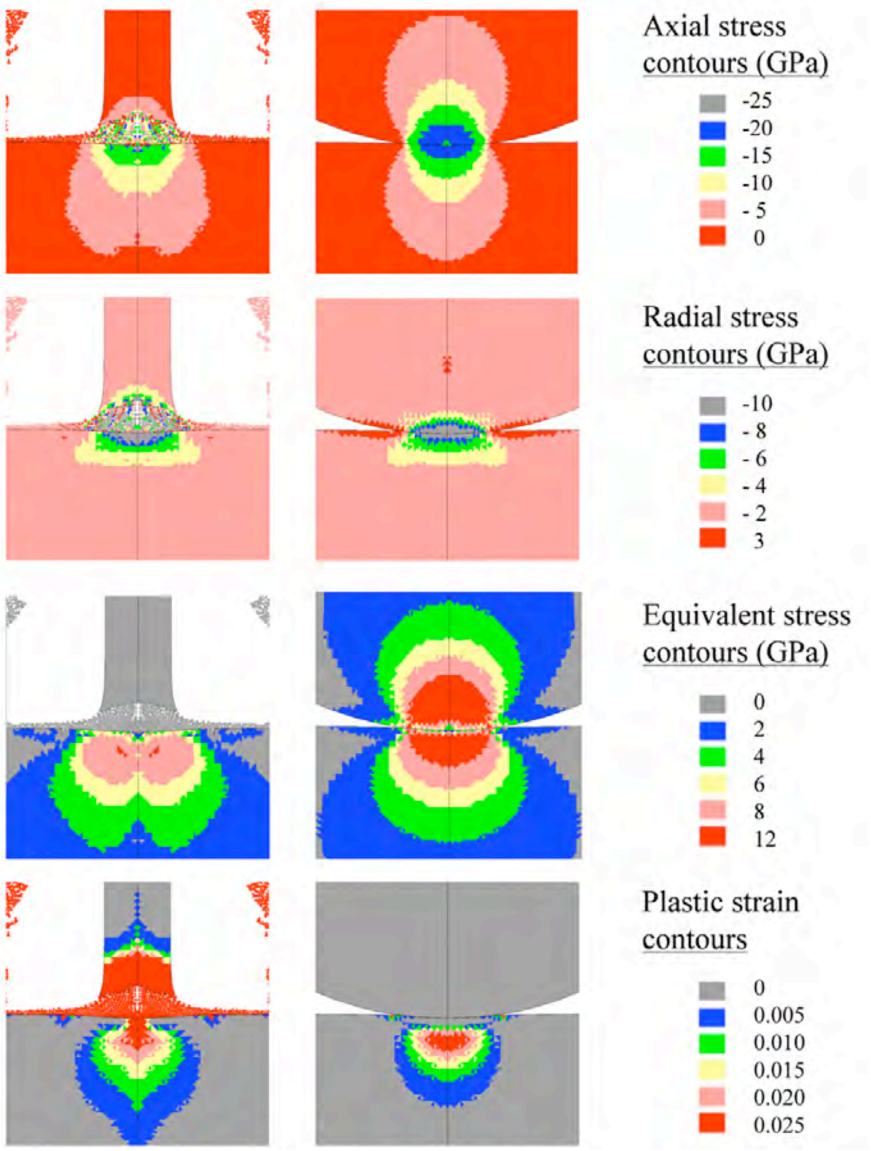

Figure 4.14. A comparison of the computed stresses and stains from a gold rod dwelling at 1300 m/s and a Hertzian indentation loaded to 52 N.

4.4. Summary

This section demonstrates an initial evaluation of the usefulness of Hertzian indentation for the determination/validation of JHB model constants and for a potential link to ballistic resistance (interface defeat). Recent advancements in producing elevated stress levels in Hertzian indentation make the usefulness of this test much more feasible. There are very few experimental techniques that can produce the high stresses, strains and pressures produced in Hertzian indentation tests. They are also relatively simple, repeatable, timely and inexpensive. There is still the disadvantage in that the stresses, strains and pressures are not explicit outputs of the experiments requiring the constitutive response to be inferred by performing computations and comparing the computed force-deflection results to the experiment. It appears that Hertzian indentation tests can be useful in inferring the constitutive response of high-strength ceramics.

Using Hertzian indentation to determine the ballistic dwell-penetration transition stress (or provide a ranking procedure) is less clear. It appears that the stress and strain fields produced from indentation are very similar to those produced from dwell, with the exception of the tensile radial stress. There appears to be very little radial tensile stress produced during dwell but significant radial tensile stress produced from indentation. It is not clear how this stress difference will affect the ability to correlate indentation response with interface defeat. There are several things that could be done experimentally that may provide insight into linking indentation and dwell. One possibility is to perform indentation tests where the loading is increased beyond the current (200 N) level to see if there is any force-displacement discontinuity that appears. If a discontinuity occurs it may be possible to correlate it to the dwell-penetration transition stress. It is also possible that there is no discontinuity from spherical indentation. If this is the case other evaluation approaches will be required. One possibility may be to use the energy absorbed during indentation as a ranking parameter. There is also the possibility of using different indenter shapes to produce different stress fields. It appears that the lack of tensile radial stress during dwell is probably due to the non-spherical shape of the projectile during dwell. A different indenter shape may produce radial stresses more similar to dwell. Computations would be helpful in determining what shapes to pursue. There are also several interesting things that could be explored computationally such as the effect of friction, determining the tensile strength from ring crack formation, the effect of machine compliance, mesh sensitivity to the failure process and the effect of damage softening. These effects will be topics for future work.

4.5. References

[4.1] C. E. Anderson, T. Behner, T. J. Holmquist, D. L. Orphal and M. Wickert, “Dwell, Interface Defeat, and Penetration of Long Rods Impacting Silicon Carbide,” Southwest Research Institute Technical Report 18.12544/008, April, 2009.

[4.2] T. J. Holmquist and G. R. Johnson, ”Characterization and Evaluation of Silicon Carbide for High-Velocity Impact,” *J. App. Phys*., 97:093502 (2005).

[4.3] G. R. Johnson, R. A. Stryk, T. J. Holmquist, and S. R. Beissel, “Numerical Algorithms in a Lagrangian Hydrocode,” Technical Report WL-TR-1997-7039, Wright Laboratory, June 1997.

[4.4] H. Hertz, “On the Contact of Rigid Elastic Solids,” *j.reine und angewandte Mathematik*, 92:156-171 (1882).

[4.5] K. L. Johnson, “Contact Mechanics,” Cambridge University Press, 1985.

5. GLASS PHASE CHANGES

5.1. Basis for Inquiry

Improving the understanding of the damage evolution of glass during a ballistic impact will enable property and ballistic improvements. One important damage mechanism in glass is high-stress induced densification. This subsection describes an initial effort to quantify such densification.

With means to perform controlled Hertzian indentation and access to a piezo-Raman spectroscopy system, the goal of this subtask was to initiate examination of the densification that may be occurring under a high-stress indent. Raman spectroscopy has been shown to be a useful method to quantify densification in glass [5.1], so interest existed to adapt that technique for use with candidate transparent armor glasses.

5.2. Preliminary Observations

A Hertzian indent was generated on a soda-lime silicate glass using a 250-µm diameter diamond indenter and a maximum force of 19.6 N. The indent produced a ring crack that was scanned along its diameter with a piezo-Raman system where an increase in peak position is indicative of a higher density [5.1]. The profile is shown in Fig. 5.1 where the highest peak positions in the middle of the indent indicate the area where the greatest amount of densification occurred which also corresponds to the location where the maximum Hertzian pressure was applied.

To examine this further, a 3-kg Knoop indent was put on the surface of the same glass, and the piezo-Raman system scanned across it too. In the bottom (middle) of the Knoop indent, the peak position shifting was more pronounced indicating an appreciable amount of densification had occurred.

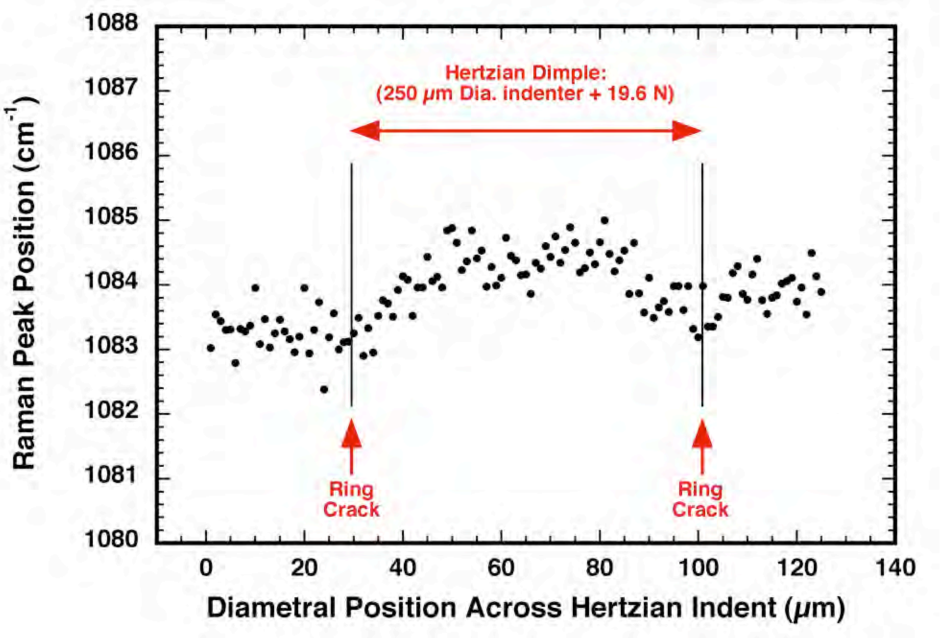

Figure 5.1. Raman peak position shifts across a Hertzian dimple on a soda lime glass. Higher valued positions constitute increases in density. The increase in density in the middle of the indent is estimated to be 2-3 %.

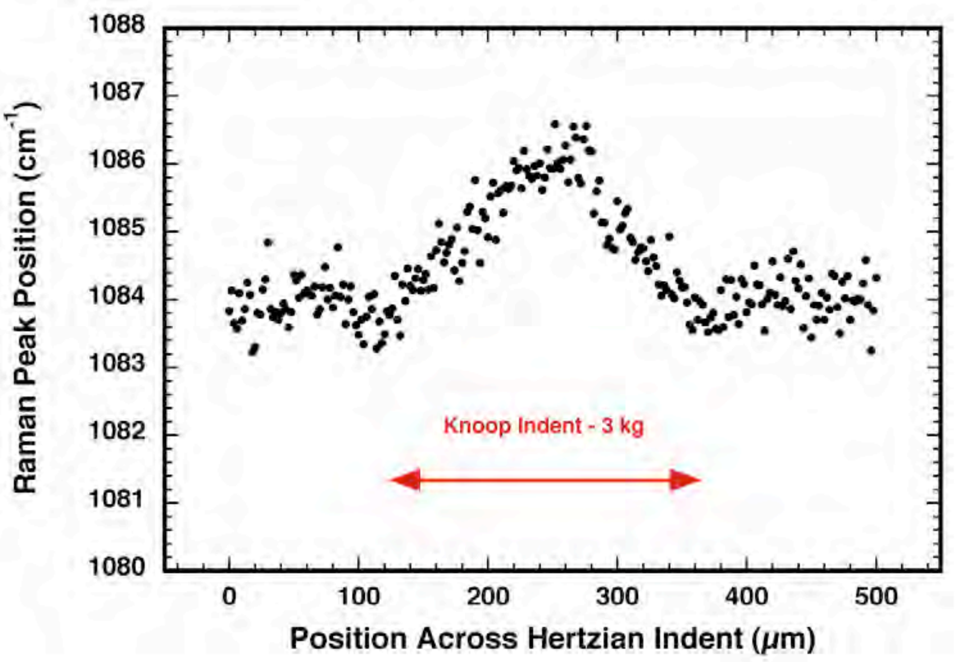

Figure 5.2. Raman peak position shifts across a 250-μm-wide 3-kg-Knoop-indent on a soda-lime glass. Higher valued positions constitute increases in density. The increase in density in the middle of the indent is greater than 2-3 %.

5.3. Summary

Raman spectroscopy has the potential to be a useful tool for the study of damage and densification in indented or ballistically impacted glass. Future studies to more confidently quantify densification would require the calibration of peak shift with applied stress for each indented glass. This could be accomplished with the positioning of a strain-gaged bend specimen under the piezo-Raman system, and the measurement of peak position as a function of applied stress.

5.4. References

[5.1] A. Perriot, D. VandemBroucq, E. Barthel, V. Martinez, L. Grosvalet, Ch. Martinet, and B. Champagnon, "Raman Microspectroscopic Characterization of Amorphous Silica Plastic Behavior, *J. Am. Ceram. Soc.*, 89:596-601 (2006).

6. CRUSH FRAGMENTATION OF GLASS

6.1. Basis for Inquiry

The goal of this subtask was to attempt to better understand high-energy-induced fragmentation behavior by relating stress state to produced particle size distribution. The understanding of such behavior is important to the understanding of the erosion of a projectile by a ceramic armor. The approach was to use crush testing of glass spheres; however, it became apparent that it was exceedingly difficult, if not impossible, to produce a valid fracture. Therefore, the work based on that approach was halted and an alternate plan is described.

Grady [6.1] has shown that the strain rate of shock failure is linkable to the produced fragment size and size distribution. To study a simple quasi-static case of this, the diametral compression of glass spheres was pursued. Very high compressive forces are necessary to crush ceramic spheres [6.2-6.6], and because of that, a lot of stored energy is in the sphere at the moment it fractures, which creates a fine-sized particle size distribution. The goal was to link the two.

6.2. Preliminary Observations

The test setup is shown in Fig. 6.1. Glass spheres were diametrally compressed between two steel push rods with countersinks in both. Vaseline was placed around the ball to retain the fragments. A valid test for this was defined as one that produces fracture of the glass sphere whose initiation is caused by an intrinsic flaw in, or on, the glass sphere. A finite element analysis of such a test is illustrated in Fig. 6.1. A vertically applied compressive load produces a first principal tensile stress around the sphere's equator. Fracture from Hertzian contact (a fixture-induced test invalidator) must be suppressed so that an intrinsic flaw causes fracture.

A conical countersunk seat on both push rods was first used, but it was found to cause fracture (and produce an invalid test). This occurred even when soft platens (folder paper) were used as a buffer between the glass ball and steel push rod. Sphere fractures with the conical countersinks in the push rods produced an "apple core" structure among all the fragments. This is shown in Fig. 6.2. The "apple core" itself was comprised entirely of very small fragments that seemingly stayed bonded by static electricity because it would fall apart with minimum handling [6.7]. The diameter of the top and bottom of the "apple core" structure was such that it was obvious this was where line loading had occurred between the sphere and the conical countersink on both sides of loading. Therefore, the continued use of a conical countersink was stopped, and a spherical countersink, with matched radius of curvature with the sphere, was pursued.

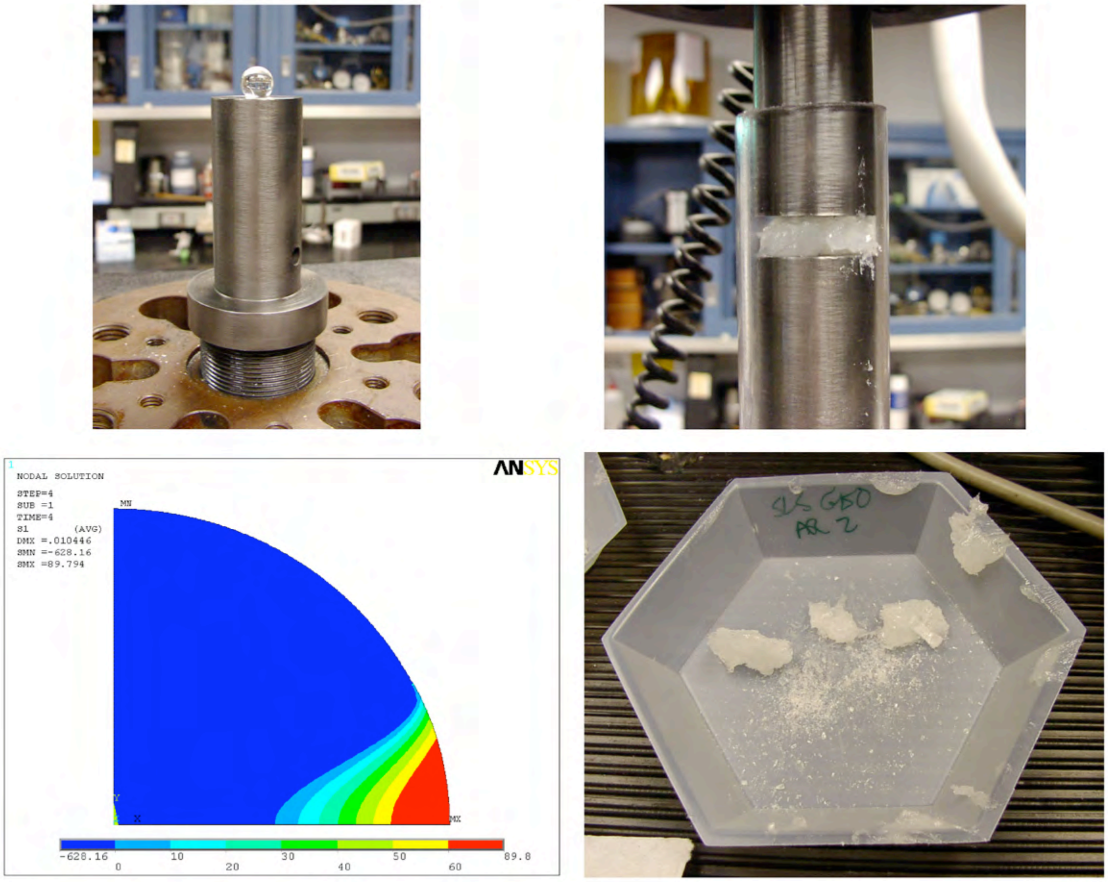

Figure 6.1. Various images regarding the crush testing of glass spheres. Upper images show the loading setup. Vaseline used to retain the fragments. The lower left shows where the tensile stress builds up in the (idealized) absence of Hertzian contact stresses. The lower right shows a crushed ball with Vaseline residue.

The use of a spherical countersink with steel push rods did not produce valid fractures either. An apple-core structure was still produced suggesting there was a circular line-load being applied on opposite sides of the glass sphere.

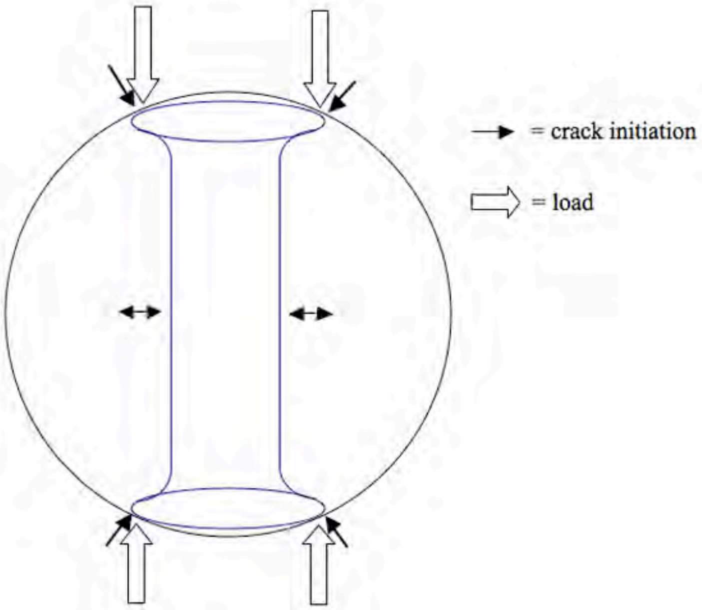

Figure 6.2. Though extensive fragmentation was produced, there was an "apple core" habit that suggested that fragmentation was initiated where the loading platen contacted the sphere. Such an event is an invalid test.

Achieving a valid test with spheres proved to be a formidable task, and it arguably was not achieved. Additionally, fractography may be the only way to confirm that Hertzian contact does not cause the fracture, and that in of itself, may not be achievable because there are many hundreds, if not thousands, of fragments (see Fig. 6.1) to explore to find the primary fracture initiation location. References 6.2-6.5, which involve the fracture of glass spheres, provide failure statistics; however, there is no confirmation that the produced results were not affected by their choices of fixturing. There seems to be an unsolvable crushing of glass sphere conundrum.

Such testing is indeed valuable, but a method must be devised to produce high-load (high-energy) fracture without the fracture being initiated by the test fixture. Namely, a test of the material must be derived, and not a test of the system. There are at least two approaches to remedy this. First, use finite element analysis to further refine the spherical countersink so that line loading is not produced. Perhaps a matched radius of curvature is not desired. Second, cease the consideration of using spheres and perhaps compress an alternative geometry instead, for example, thin glass disks.

6.3. References

[6.1] D. E. Grady, "Shock-Wave Compression of Brittle Solids," *Mech. Mat.,* 29:181-203 (1998).

[6.2] J. J. Gilvarry and B. H. Bergstrom, "Fracture of Brittle Solids. II. Distribution Function for Fragment Size in Single Fracture (Experimental),"*J. App. Phys., 32:*400-410 (1961).

[6.3] B. H. Bergstrom, C. L. Sollenberger, and W. Mitchell, Jr., "Energy Aspects of Single Particle Crushing," *Trans. Am. Instit. Min. Met Pet. Eng., 220:*367-372 (1961).

[6.4] B. H. Bergstrom, "Energy and Size Distribution Aspects of Single Particle Crushing," *Proc. 5th Symp. Rock Mechanics,* 155-72 (1962).

[6.5] B. A. Kschinka, S. Perrella, H. Nguyen, and R. C. Bradt, "Strengths of Glass Spheres in Compression," *J. Am. Ceram. Soc.,* 69:467-72 (1986).

[6.6] W. G. Luscher, J. R. Hellman, A. E. Segall, D. L. Shelleman, and B. E. Scheetz, "A Critical Review of the Diametral Compression Method for Determining the Tensile Strength of Spherical Aggregates," *J. Test. Eval.,* 35:1-6 (2007).

[6.7] W. L. Daloz, "Surface Treatment Effects on Compressive Strength of Glass Spheres," Ceramic Engineering B. S. Thesis, Kazuo Inamori School of Engineering, Alfred University, May 2007.

7. ADDITIONAL TESTING AND ANALYSIS

The descriptions within this section summarize ancillary FY09 efforts that primarily provide improved understanding of the tensile strength behavior in boron carbide and silicon carbide as a function of scale and the flaws that limit those failure stresses. The herein described findings are important because they show (1) there is no single failure stress value that should be used in ballistic models to describe all deflection or expanding cavity behaviors, and (2) generated data that can indeed be used to predict and model those behaviors.

This section has four parts. The first and second describe strength-size scaling in boron carbide and silicon carbide, respectively, the third discusses the interpretation of flaw size statistics in a silicon carbide, and the fourth considers diametral compression (a test gaining popularity for high rate testing).

7.1. Boron Carbide Strength-Size Scaling

The uniaxial tensile strength of a ceramic is one property of many used to describe and predict the response of an armor ceramic subjected to a ballistic impact. While elastic modulus and Poisson's ratio can each be represented by a size-independent, single value for a given ceramic, this is not the case for uniaxial tensile strength.

Ceramics exhibit uniaxial tensile strength-size-scaling and its management has been in practice for decades. An analogy of a "weakest link in a chain" is often used to describe that scaling. The uniaxial tensile strength is usually of greatest interest to a structural ceramic designer because it typically is at least an order of magnitude smaller than its compressive strength of the same volume. That asymmetry in strength is a consequence of how the direction of stress differently activates fracture of flaw populations [7.1-7.2]. The compressive strength of a ceramic is not considered in this study, so the use of "strength" hereafter implies tensile strength.

The two-parameter Weibull distribution [7.3] is typically used to represent that strength-size scaling, with the two parameters being characteristic strength and Weibull modulus. If competing strength-limiting flaws are operative, then a censored Weibull distribution is determined for each type using fractography. For simple test geometries and loading configurations (e.g., standardized bend tests), strength-size scaling can be enabled through established methods of integrating the volume, or surface area, or edge-length subjected to a first principal tensile stress (e.g., see Weil and Daniel [7.4]). For ceramic test configurations and components whose stress field cannot be analytically analyzed, their strength-size scaling can be determined with a combination of finite element analysis and integrated design and reliability software.

There are at least two cases where the tensile strength of an armor ceramic is used in modeling. In the first, tensile strength is used to predict the allowable deflection of a relatively thin (yet macrostructural) ceramic armor plate or structure subjected to an impact [7.5-7.7]. In the second, it is used in the modeling of an (microstructural scale) expanding cavity of damage in the ceramic under the interface between it and a projectile [7.8]. Being that these sizes of scale are quite different, and because polycrystalline ceramics are known to exhibit strength-size scaling, it stands to reason that using a single value of "tensile strength" for both cases could be both improper and inaccurate.

The changes in tensile strength of a hot-pressed boron carbide (B_4C) over a wide range of size are described in the present study from the macrostructural down to the microstructural scale. Boron carbide is often used as a personnel armor ceramic because of its low density. This application then demands it to be relatively thin for weight minimization, and that results in its tiling or plating being susceptible to structural deflection from a ballistic impact. That same ballistic impact can result in its microstructure undergoing damage describable by expanding cavity modeling.

7.1.1. Experimental

The evaluated boron carbide was a hot-pressed, commercially available grade. The test surfaces of the tiles were rotary ground and had a measured surface roughness (Ra) of 0.5 μm.

Equibiaxial flexure strength was measured using ring-on-ring and ball-on-ring tests. The failure stress for ring-on ring (S_{RoR}) of a square plate was calculated using [7.9]

$$S_{RoR} = \frac{3P}{2\pi t^2}\left[\left(1-\nu\right)\frac{{D_S}^2-{D_L}^2}{2D^2}+\left(1+\nu\right)\ln\frac{D_S}{D_L}\right] \tag{7.1}$$

and

$$D = \frac{0.5\left(l_1 + l_2\right)}{0.90961 + 0.12652\frac{t}{D_S} + 0.00168\ln\frac{0.5\left(l_1 + l_2\right) - D_S}{t}} \tag{7.2}$$

where P is the failure force, t is thickness, ν is Poisson's ratio, D_S is the support ring diameter, D_L is the loading ring diameter, and l_1 and l_2 are the widths of the plate. The failure stress for ball-on-ring (S_{BoR}) of a square plate using a 12.7 mm diameter WC ball was calculated using [7.10]

$$S_{BoR} = \frac{3P(1+\nu)}{4\pi t^2}\left[1 + 2\ln\left(\frac{D_S/2}{0.4384}\right) + \left[\frac{(1-\nu)D_S^2}{(1+\nu)D^2}\right]\left[1 - \left(\frac{0.4384^2}{D_S^2/2}\right)\right]\right] \quad . \tag{7.3}$$

Large square tiles (305 x 305 x 5.7 mm and 152 x 152 x 4.9 mm) were first tested. Smaller specimens, whose sizes are listed in Table 7.1, were then harvested from large fragments of the tested 305 mm square tiles. The thickness of the smaller specimens needed to be reduced from that of the original tiles to maintain valid bend testing according to ASTM C 1499 [7.9]. This was achieved by grinding one side of the original 5.7 mm thick tiles down to a thinner size but by continuing to test the one remaining original ground surface in tension in the flexure testing. Loading and supporting ring diameters are provided in Table 7.1 for the ring-on-ring testing. For the ball-on-ring test, a 12.7 mm diameter WC ball was used for the loading.

Hertzian (spherical) indentation testing was performed using silicon nitride (Si_3N_4), aluminum oxide (Al_2O_3), and tungsten carbide (WC) balls with different diameters. The details of the test and method are described in Section 1.2. The different ball materials were chosen because their range of elastic moduli bracket that of the B4C, they enable insight into the effects of elastic property mismatch between indenter and target material, they readily can initiate ring cracking, and because they are commercially available and relatively inexpensive. A listing of the diameters is shown in Table 7.1. The spheres were pressed against the as-ground B_4C tiles until ring crack initiation occurred. The initiation of the ring cracking event and its associated Hertzian compressive force were identified with the aid of an acoustic emission test system.

For the sake of simplicity, the existence of a frictionless contact surface was assumed for all Hertzian indentation testing, so the maximum (radial tensile) stress associated ring crack initiation (S_{RCI}) was calculated according to [7.11]:

$$S_{RCI} = (1 - 2\nu)\frac{P_{RCI}}{2\pi a^2} \tag{7.4}$$

where ν is the Poisson's ratio of the target, P_{RCI} is the compressive force needed to initiate ring cracking, and a is the Hertzian contact radius (calculation of the latter can also be found in Ref. 7.11). An elastic modulus of 450 GPa and a Poisson's ratio of 0.17 for the B_4C were used in the calculations. For the sphere materials, the elastic modulus and Poisson's ratio were measured with an resonance ultrasound spectroscope and were used in the Hertzian indentation stress calculations. An elastic modulus of 312 GPa and a Poisson's ratio of 0.276 were used for the Si_3N_4, 371 GPa and 0.238 for the Al_2O_3, and 629 GPa and 0.211 for the WC.

Table 7.1. Test configurations used to measure maximum tensile stress to failure. Types 1-5 are equibiaxial flexure tests and Type 6 are ring crack initiation tests.

Test Type Designator	**Test Method**	**Fixture Size (mm)**	**Tile Size (mm)**
1	Ring-on-Ring	140 on 280	305 x 305 x 5.70
2	Ring-on-Ring	70 on 140	152 x 152 x 4.90
3	Ring-on-Ring	15 and 35	45 x 45 x 2.48
4	Ring-on-Ring	6.35 on 15	20 x 20 x 1.33
5	Ball-on-Ring	12.7 on 15	20 x 20 x 1.33
6a-SN-300	Spherical or Hertzian Indentation	Si_3N_4 Ball : 3.00 mm ø	5.7 mm thick
6b-SN-600		Si_3N_4 Ball : 6.00 mm ø	
6c-SN-952		Si_3N_4 Ball : 9.52 mm ø	
6d-SN-1270		Si_3N_4 Ball : 12.70 mm ø	
6e-SN-2540		Si_3N_4 Ball : 25.40 mm ø	
6f-SN-3175		Si_3N_4 Ball : 31.75 mm ø	
6g-SN-4762		Si_3N_4 Ball : 47.62 mm ø	
6h-AO-635		Al_2O_3 Ball : 6.35 mm ø	
6i-AO-1270		Al_2O_3 Ball : 12.70 mm ø	
6j-AO-2540		Al_2O_3 Ball : 25.40 mm ø	
6k-WC-400		WC Ball : 4.00 mm ø	
6l-WC-800		WC Ball : 8.00 mm ø	
6m-WC-1270		WC Ball : 12.70 mm ø	
6n-WC-2540		WC Ball : 25.40 mm ø	

Commercial statistical software was used to fit the strengths in all sets listed in Table 7.2 to a two-parameter Weibull distribution using maximum likelihood estimation. These results adhere to ASTM C 1239 [7.12] for reporting Weibull statistics.

Lastly, the effective areas (k_A•A) of each of the ring-on-ring and ball-on-ring test configurations were determined through integration of each of their imposed stress gradients and the principal of independent action. The probability of failure (P_f) is then linkable to the effective area according to

$$P_f = 1 - \exp\left[-k_A \bullet A\left(\frac{S}{S_{OA}}\right)^m\right] \tag{7.5}$$

where S is stress, S_{OA} is a scaling parameter for surface (or area) type flaws, and m is Weibull modulus. For the same ceramic and strength-limiting flaw type, the maximum tensile stress scaling for the same probability of failure between specimens or components of different effective areas is calculated according to

$$S_B = \left(\frac{k_{AA} \bullet A_A}{k_{AB} \bullet A_B} \right)^{1/m} S_A \tag{7.6}$$

where S_A and S_B are the maximum tensile stress on the surfaces of specimens A and B, respectively, and $k_{AA} \bullet A_A$ and $k_{AB} \bullet A_B$ are the effective areas of specimens A and B, respectively. The effective area of the Hertzian radial tensile stress at the surface just beyond the Hertzian contact area is simply $\pi a^2/(m-1)$ for a frictionless contact surface as shown in Section 1.4.

7.1.2. Results and Discussion

The characteristic strength as a function of effective area for all the test sets are portrayed in Fig. 7.1 and listed in Table 7.2. Two domains are evident. Strength-size scaling exhibits one trend over an effective area range of 1 to ~40,000 mm^2 and another for effective areas less than 0.1 mm^2. A Weibull modulus of 9.3 represents the strength-size scaling for the 1 to ~40,000 mm^2 range whereby the characteristic strength for the 1 mm^2 is triple that for ~40,000 mm^2. There were higher Weibull moduli for the Hertzian ring crack initiation results (effective areas less than 0.1 mm^2) and characteristic strengths that were an order of magnitude or more greater than that for an effective area of ~ 40,000 mm^2.

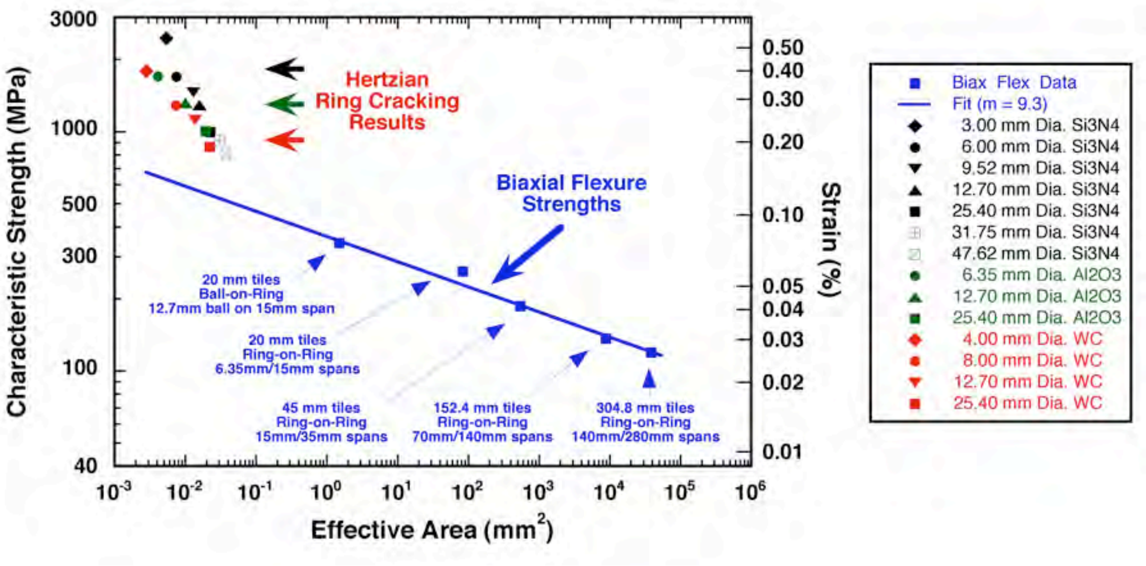

Figure 7.1. Characteristic strength of hot-pressed B_4C as a function of effective area. Weibull modulus of 9.3 fits the strength data measured using biaxial flexure. All other data generated with Hertzian ring crack testing.

Table 7.2. Characteristic strength, Weibull modulus, and effective area results for the B_4C testing.

Test Type Designator	**Number of Tests**	**Characteristic Strength [*] (MPa)**	**Weibull Modulus [*]**	**Effective Area [**] (mm^2)**
1	10	119 (112, 126)	10.5 (7.2, 18.6)	38383
2	4	137 [***]	14.8 ***	8770
3	18	187 (169, 205)	4.8 (3.5, 7.3)	540
4	21	260 (246, 275)	8.0 (6.0, 11.6)	83.9
5	22	343 (328, 358)	9.9 (7.3, 14.4)	1.51
6a-SN-300	23	2360 (2251, 2466)	9.3 (7.0, 13.5)	0.0054
6b-SN-600	24	1634 (1575, 1692)	11.6 (8.9, 16.4)	0.0075
6c-SN-952	21	1407 (1358, 1454)	12.9 (9.6, 18.7)	0.0130
6d-SN-1270	26	1245 (1207, 1283)	13.0 (10.1, 17.7)	0.0158
6e-SN-2540	29	959 (943, 975)	23.1 (18.1, 31.1)	0.0227
6f-SN-3175	18	890 (868, 911)	19.7 (15.0, 28.4)	0.0305
6g-SN-4762	24	777 (767, 786)	35.3 (27.0, 49.7)	0.0373
6h-AO-635	32	1683 (1650, 1716)	18.6 (15.0, 24.2)	0.0041
6i-AO-1270	26	1303 (1273, 1332)	17.5 (13.9, 23.5)	0.0100
6j-AO-2540	29	995 (975, 1014)	19.1 (15.6, 24.9)	0.0194
6k-WC-400	22	2235 (2176, 2290)	16.9 (12.8, 24.3)	0.0028
6l-WC-800	22	1604 (1546, 1660)	12.1 (9.2, 17.3)	0.0074
6m-WC-1270	34	1399 (1355, 1442)	11.2 (9.1, 14.5)	0.0137
6n-WC-2540	28	1076 (1055, 1096)	19.8 (15.4, 27.1)	0.0221
7 [∇]				94

[*] Uncensored maximum likelihood estimation. Values in parenthesis are +/- 95% likelihood ratio confidence bounds.

[**] Shown values based on a Weibull modulus of 9.3.

[***] Insufficient number of data points to estimate confidence bounds.

[∇] 4-Point-Bend, 3x4x50mm bar geometry, 20/40mm spans, transversely machined. Not tested in this study but shown here for comparison.

The seven orders of magnitude difference in effective areas is illustrated in Fig. 7.2 along with a description of the macrostructural and microstructural scale and potential flaws that can limit the strengths of the two different domains. Optical fractography showed that equibiaxial flexure strengths were limited by machining damage - specifically, relatively deep machining grooves that were located on the gage section. Surface grinding marks are evident in Test Type 5 (the smallest of the biaxial flexure test configurations). The primary fracture surface was always aligned with such local grinding grooves for all test specimens in Test Types 1-5. However, for the Hertzian indentation, the small sampled effective area (less than 0.1 mm^2) tended to only offer up strength-limiting flaws on the microstructural scale (e.g., relatively large grains, carbon inclusions, etc.).

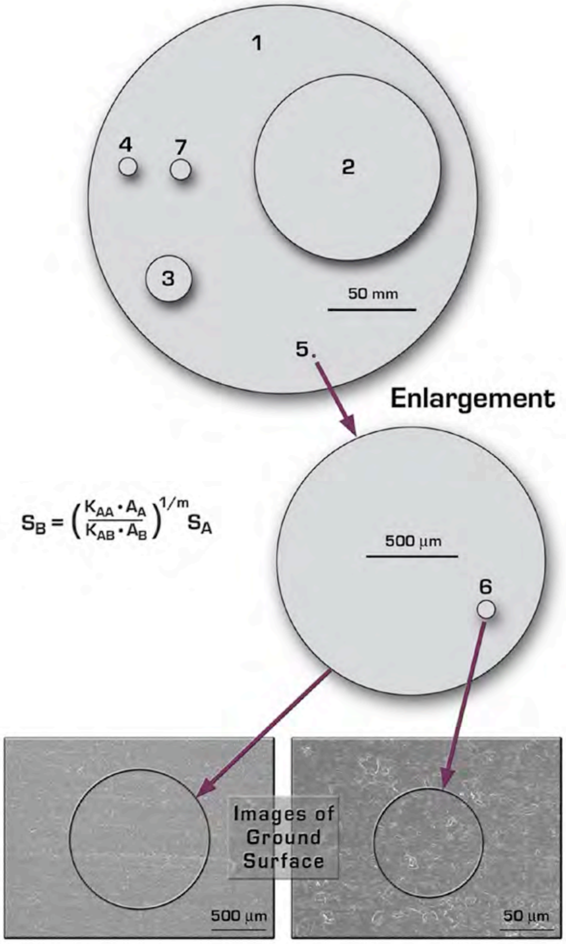

Figure 7.2. Relative effective areas sampled with the B_4C. Numbers in circles correspond to test types listed in Tables 7.1-7.2.

Though the flaws associated with Hertzian ring crack initiation are of course present during equibiaxial flexure strength testing too, the machining damage flaws are dominant because of their much larger size. Employing the Griffith criterion with all the measured maximum tensile stresses, a fracture toughness of 3.1 for B_4C, and a crack shape parameter (Y) of 1.5, strength-limiting flaw distributions can be estimated. Three distributions are shown in Fig. 7.3. The distributions for the equibiaxial and Hertzian indentation do not, or very minimally, overlap. The biaxial flexure and the Hertzian testing simply activate different strength-limiting flaw types because of the very different effective area scales of each sample. The grain size distribution of the B_4C, shown in Fig. 7.3, was determined using polished cross-sections and image analysis software. The grain size distribution overlaps with much of the distribution for the estimated flaw sizes for the Hertzian indentation, and because of that, is consistent with the Hertzian ring crack initiation being affected by microstructural-scale strength-limiting flaws.

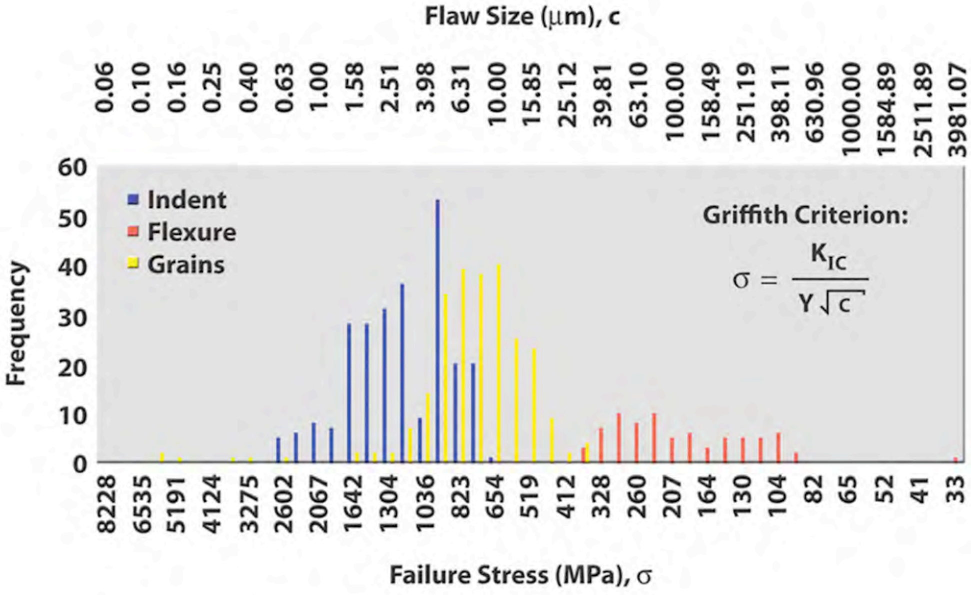

Figure 7.3. Maximum failure stress and estimated flaw size distributions for the tested boron carbide.

Suppressing bending stresses during a ballistic impact desirably increases the amount of available time that the ceramic has to interact with the projectile and increases the erosiveness of the event. Sherman [7.5-7.7] has considered such bending in detail with the modeling of an impacted aluminum oxide armor ceramic. For relatively thick tiles, impact-side damage (conical damage, which is relatable to Hertzian ring crack initiation) is more likely to be prevalent because the tile has relatively high stiffness, there is little outer-fiber deflection, and tensile stresses on the back of the tile do not get sufficiently high. As tile thickness decreases, the amount of outer-fiber deflection increases, developed tensile stresses increase, and crack initiation is more likely to occur.

Sherman [7.6] used a lone tensile stress of 400 MPa for aluminum oxide to predict crack initiation in a ballistically impacted tile. Not only is there likely to be variability about that deterministically used tensile stress value, but perhaps more significantly, the strength-size scaling results in this study show that the use of a single tensile stress in such modeling can be quite inaccurate without appropriate use of size. If two tiles made of the same ceramic have the same thickness but one is larger than the other, then crack initiation in the larger tile will be more likely to occur even if their applied tensile stress to both is the same.

Taking into account the tensile strength-size scaling of an armor ceramic using an appropriate value of tensile stress for a given size or effective area will result in more valid predictions of allowable tile deflection.

For an infinitely thick armor ceramic target, Satapathy and Bless derived [7.8] the static pressure required to open up a cavity (R_t) as,

$$R_t = Y\left[\frac{E/3Y}{1-(1-\nu)\sqrt{\frac{\sigma_f}{2Y}}}\right]^{2\alpha/3} \tag{7.7}$$

where Y is yield strength,[3] E is elastic modulus, ν is Poisson's ratio, α is a term representative of the pressure-shear behavior of the comminuted ceramic region, and σ_f is the tensile or failure strength. In Satapathy and Bless's paper, a tensile strength of 262 MPa was used for an aluminum oxide - about 1/3 less than what Sherman used in the tile deflection modeling.

What tensile or failure strength should be used for cavity expansion modeling? A relatively small volume of material is being subjected to a tensile stress analogous to the stress state associated with the initiation of a median crack under an indent. Because the Hertzian indentation sampled a small amount of material, flaws whose sizes were of the scale of the B_4C's microstructure caused the resulting ring crack initiations. While the equibiaxial flexure strength was limited by machining damage over large areas - an extrinsic flaw population, localized microstructural flaws - an intrinsic flaw population, limited the Hertzian ring crack initiation resistance.

The same intrinsic flaws that limited Hertzian ring cracking resistance would likely be operative in the relatively small volume of tensile-stressed material confining the expanding cavity. Therefore, because of observed strength-size scaling in this study, the high likelihood that such scaling exists for all polycrystalline ceramics, and the small amount of sampled volume associated with an expansion cavity, there is a high likelihood that the localized tensile stress of failure should have been much greater than the 262 MPa value that Satapathy and Bless used.

Summarizing Section 7.1

- Weibull strength-size-scaling in a rotary-ground, hot-pressed boron carbide was examined over effective areas ranging from approximately 10^{-3} to 10^{+5} mm^2. Equibiaxial flexure and Hertzian testing were used for the strength testing.
- Characteristic strength tripled when the effective area decreased from 40,000 to 1 mm^2, and increased by more than an order of magnitude for effective areas less than 0.1 mm^2. Machining damage limited strength as measured with equibiaxial flexure testing for effective areas greater than ~ 1 mm^2 and microstructural-scale flaws limited strength for effective areas less than 0.1 mm^2 for the Hertzian testing.
- The results show if a tensile strength of a ceramic is to be used in the modeling of ballistically-induced tile deflection or in expanding cavity modeling, then one should avoid the use of a deterministic value and preferably use a value commensurate with the amount of ceramic material subjected to a first principal tensile stress.

---

[3] It is worth noting here that "yielding" in ceramics is unlike classical yielding in metals. The yielding-like damage zone in ceramics is a consequence of confined high shear stresses that can cause plastic mechanisms but that typically also comprise intergranular and intragranular microcracking. This microcracking contribution does not occur in metals.

7.2. Silicon Carbide Strength-Size Scaling

Like for B_4C described in the previous subsection, the changes in tensile strength of hot-pressed silicon carbide (SiC) with two different surface conditions, and over a wide range of size, are described here from the macrostructural down to the microstructural scale. Silicon carbide is often used as a vehicular armor ceramic. This application demands weight minimization, which can result in its tiling or plating being susceptible to structural deflection from a ballistic impact. Additionally, ballistic impact can result in the target's microstructure undergoing damage describable by an expanding cavity model.

The evaluated silicon carbide was a commercially available hot-pressed grade, and two surface conditions were considered. One test surface was produced using a proprietary uniaxial grinding method and had a measured surface roughness (R_a) of 0.27 μm perpendicular to the grinding direction. The second test surface was uniaxial ground, then grit-blast for 2 minutes using alumina media, and had a R_a of 0.50 μm.

Two tile geometries (305 x 305 x 6.45 mm and 101.6 x 101.6 x 3.15 mm), identified in Table 7.3 as Test Types 1-2, were tested first. Smaller specimens, Test Types 3-5, were harvested from an extra Test Type 1 tile. The thicknesses of the Test Type 3-5 specimens needed to be reduced from that of the original tile to maintain valid bend testing according to ASTM C 1499 [7.9]. This was achieved by reducing the thickness by grinding one side of the original 6.45 mm thick tiles down to a thinner size (and by continuing to test the one remaining original ground surface in tension in the flexure testing). Loading and supporting ring diameters are provided in Table 7.3 for the ring-on-ring testing. For the ball-on-ring test (Test Type 5), a 12.7 mm diameter WC ball was used for the loading. The same equations described in Section 7.1 were used for the strength analysis here too.

Table 7.3. Test configurations used to measure maximum tensile stress to failure of SiC-N for both surface conditions. Types 1-5 are equibiaxial flexure and Types 6-8 are ring crack initiation.

Test Type Designator	**Test Method**	**Fixture Size (mm)**	**Tile Size (mm)**
1	Ring-on-Ring	140 on 280	305 x 305 x 6.45
2	Ring-on-Ring	45 on 90	101.6 x 101.6 x 3.15
3	Ring-on-Ring	15 on 35	50 x 50 x 2.64
4	Ring-on-Ring	6.35 on 15	25 x 25 x 1.18
5	Ball-on-Ring	12.7 (ball) on 9 (ring)	25 x 25 x 1.18
6	Spherical or Hertzian Indentation	Si_3N_4 Ball : 47.62 mm ø	6.45 mm thick
7		Si_3N_4 Ball : 12.70 mm ø	
8		Si_3N_4 Ball : 3.00 mm ø	

Hertzian (spherical) ring crack initiation testing was performed using varying diameter silicon nitride (Si_3N_4) balls (Test Types 6-8 in Table 7.3). The details of the test and method are described in Section 1.2. Silicon nitride balls were chosen because they are commercially available in various diameters, are relatively inexpensive, and can readily cause ring cracking in SiC. The spheres were pressed against the test surface for both surface-conditions until ring crack initiation occurred. The initiation of the ring cracking event and its associated Hertzian compressive force were identified with the aid of an acoustic emission test system.

The characteristic strength as a function of effective area for all the test sets are portrayed in Fig. 7.4 and listed in Tables 7.4 and 7.5. Though there were not consistent and significant strength differences between the two surface conditions, two domains were evident with both. Strength-size scaling exhibits one trend over an effective area range between ~ 0.1 to ~ 40,000 mm^2 and another for effective areas between ~ 0.001 to 0.1 mm^2 for both ground conditions. A Weibull modulus of 9.4 and 11.7 represents the strength-size scaling for the 0.1 to ~ 40,000 mm^2 range for the standard ground and grit-blasted surfaces, respectively, whereby the characteristic strength for 0.1 mm^2 is 3-4 times larger than that for ~ 40,000 mm^2. This is a very large difference in failure stress, and illustrates two things that are expected of polycrystalline ceramics; there is not a single strength value for the SiC tested and failure stress is clearly dependent on how much area is (tensile) stressed.

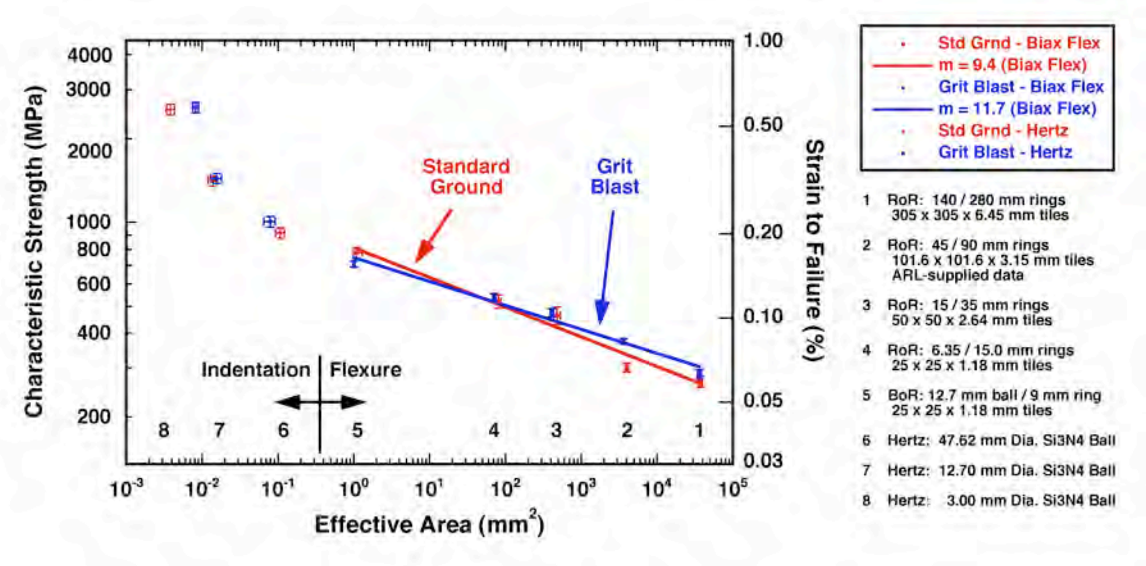

Figure 7.4. Characteristic strength of hot-pressed SiC as a function of effective area and with two different surface conditions.

The failure stress substantially increases for effective areas less than 0.1 mm^2, and its change is not fittable using Eq. 7.5 and the same Weibull moduli that were for effective areas greater than 0.1 mm^2. This suggests the dominant strength-limiting failure mode changed for the two domains. Optical fractography showed that machining damage consistently limited strength for Test Types 1-5. Data from Test Type 6 (Hertzian indentation with a 47.62 mm diameter

Si_3N_4 sphere) appears that it would also fit well to the regressed lines (i.e., Eq. 7.6) that go through data of Test Types 1-5; however, it could not be conclusively determined that machining damage was associated with Test Type 6 Hertzian ring crack initiation. Using the Griffith criterion with a fracture toughness of 4.49 MPa√m for this SiC [7.12] and a crack geometry value of 1.5, a Griffith flaw size of 4.6 μm is estimated for a characteristic strength of 1400 MPa (i.e., Test Type 7) and 1.4 μm is estimated for 2500 MPa (i.e., Test Type 8). The average grain size of this SiC is 3.25 μm with grain sizes in its distribution as large as 12-13 μm as shown in Section 1.3, so the failure stress associated with ring crack initiation of Test Types 7-8 are likely caused by the grains themselves or some "flaw" of the same scale of the SiC grains. This is a different strength-limiting flaw mechanism than what was active for larger effective areas, and is the reason why a single Weibull modulus in Eq. 7.6 does not fit characteristic strengths over the entire domain. Though the flaws associated with Hertzian ring crack initiation are present during equibiaxial flexure strength testing too, the machining damage flaws are so much more dominant because of their much larger size. Similar to this observation, such a change in strength-size-scaling was observed with a hot-pressed boron carbide as shown in Section 7.1, so this trend in changing dominant mechanism may be normal for polycrystalline ceramics.

Table 7.4. Characteristic strength, Weibull modulus, and effective area results for the standard ground condition of SiC-N.

Test Type Designator	**Number of Tests**	**Characteristic Strength * (MPa)**	**Weibull Modulus ***	**Effective Area ** (mm^2)**
1	14	268 (256, 279)	12.2 (8.8, 19.3)	37423
2	39	301 (289, 312)	8.6 (7.0, 11.1)	4011
3	18	463 (430, 496)	6.6 (4.7, 10.2)	477
4	23	519 (490, 548)	7.6 (5.8, 10.7)	81.4
5	20	776 (740, 812)	9.6 (7.0, 14.5)	1.09
6	26	876-954 £	15.9	0.093-0.122 ¢
7	22	1350-1470 £	20.1	0.012-0.016 ¢
8	21	2435-2652 £	13.9	0.0034-0.0043 ¢
9 ***				94.0

* Uncensored maximum likelihood estimation. Values in parenthesis are +/- 95% likelihood ratio confidence bounds.

** Shown values based on a Weibull modulus of 9.4.

*** 4-Point-Bend, 3x4x50mm bar geometry, 20/40mm spans, transversely machined. Not tested in this study but included here for comparison.

£ Lower value for coefficient of friction = 0, higher value for infinite friction.

¢ Lower value for coefficient of friction = ∞, higher value for zero friction.

Table 7.5. Characteristic strength, Weibull modulus, and effective area results for the grit blast condition of SiC-N.

Test Type Designator	**Number of Tests**	**Characteristic Strength * (MPa)**	**Weibull Modulus ***	**Effective Area ** (mm^2)**
1	14	285 (274, 296)	14.3 (9.9, 23.6)	36554
2	32	373 (365, 382)	16.2 (12.6, 22.0)	3618
3	18	473 (457, 490)	13.8 (9.9, 21.2)	410
4	20	540 (525, 555)	16.2 (12.2, 23.6)	71.5
5	28	708 (690, 724)	16.1 (12.3, 22.4)	1.00
6	27	962-1048 £	25	0.065-0.092 ¢
7	28	1378-1501 £	18.5	0.013-0.018 ¢
8	18	2478-2699 £	7.4	0.0075-0.0090 ¢
9 ***				91.4

* Uncensored maximum likelihood estimation. Values in parenthesis are +/- 95% likelihood ratio confidence bounds.

** Shown values based on a Weibull modulus of 11.7.

*** 4-Point-Bend, 3x4x50mm bar geometry, 20/40mm spans, transversely machined. Not tested in this study but included here for comparison.

£ Lower value for zero coefficient of friction, higher value for ∞ friction.

¢ Lower value for ∞ coefficient of friction, higher value for zero friction.

The same issues discussed in Section 7.1 regarding the uncertain use of a single failure stress or deflection or cavity expansion apply here in Section 7.2 too for SiC.

Additionally though, shock wave measurements of this SiC exhibit strength-size-scaling that have been attributed to a strain-rate-dependent effect. However, the results from the herein described work are in agreement with those shock wave results. Namely, this infers that that shock-wave size-scaling effect could be caused by a material strength-size-scaling effect and not a strain-rate dependent effect [7.13]. This examination will be further pursued in future work by the authors.

Summarizing Section 7.2

- Quasi-static Weibull strength-size-scaling of a hot-pressed silicon carbide having two surface conditions (uniaxial ground and uniaxial ground followed by grit blasting) was examined over effective areas ranging from approximately 4 x 10^{-3} mm^2 to 4 x 10^4 mm^2.
- Characteristic strength was found to substantially increase with decreased effective area for both ground conditions. Weibull moduli of 9.4 and 11.7 well-represented strength-size-scaling for the two ground conditions between an effective area range of 10^{-1} and 4 x 10^4 mm^2 , and machining damage was observed to be the dominant flaw type over that range.

- For effective areas less than 10^{-1} mm^2, the characteristic strength increased rapidly for both ground surface conditions as effective area decreased further indicating that microstructural-scale flaws started to act as strength-limiting flaw types.
- Such strength-size-scaling should be considered when considering what failure stresses should be used for modeling ballistic-induced tile deflection, when modeling an expanding cavity in a target material, and potentially assessing dynamic strength.

7.3. Flaw Size and Strength Statistics

A lot of strength testing has been performed in this project. From that, fractography is often used to estimate the strength limiting flaw size. But can one go in the opposite direction? Namely, if a flaw size distribution was quantified, then could a strength distribution and size scaling be predicted? Such analysis would be great for material development. It turns out that Jayatilaka and Trustrum considered such analysis approximately 30 years ago [7.1-7.2].

Such analysis is predicated on an ability to quantify potential flaw sizes. This is not a trivial thing to do in structural ceramics. A research group at Nagaoka University [7.14] has developed an elegant way to accomplish this. It involves thin sectioning the ceramic material, and then using low-magnification transmitted optical microscopy. The low magnification enables large areas and volumes to be sampled - this was difficult to accomplish with a scanning electron microscope. The same method was used with SiC-N.

The specimen preparation consisted of the following. One side of several 20 x 20 x 1 mm plates of SiC-N was metallographically polished. The opposite side to the polishing was then surface ground to produce plates of ~ 100 µm thickness. A specially designed vacuum chuck was used to hold the plates down (this is an enabling piece of hardware because it circumvents the conventional use of crystal bond to hold down a workpiece). The ground side of the ~ 100 µm thick tiles were then hand polished down to approximately 30-50 µm. Transmitted light would pass through the 30-50-µm thick plates. Low-magnification (50x was sufficient) pictures were taken of the microstructures shown by the transmitted light.

Flaws (typically large carbon inclusions) were counted and measured, and interpreted using the method of Jayatilaka [7.1]. The results are shown in Fig. 7.5. Flaws as large as many tens of microns were identified - flaws that are an order of magnitude larger than the mean size of the microstructure's grains. Combining the method developed at Nagaoka University with Jayatilaka's method produces an estimated Weibull modulus of 3.8 for SiC-N. This value is lower than the Weibull moduli shown in Fig. 7.4; however, machining damage produced the Weibull moduli in Fig. 7.4 whereas the carbon inclusion flaws quantified in Fig. 7.5 are different, and are more relevant to the small effective areas sampled by Hertzian indentation in Fig. 7.4. This method has potential to help with the development of armor ceramics; namely, its use could aid in the continuing desire to both strengthen them and reduce their scatter in strength.

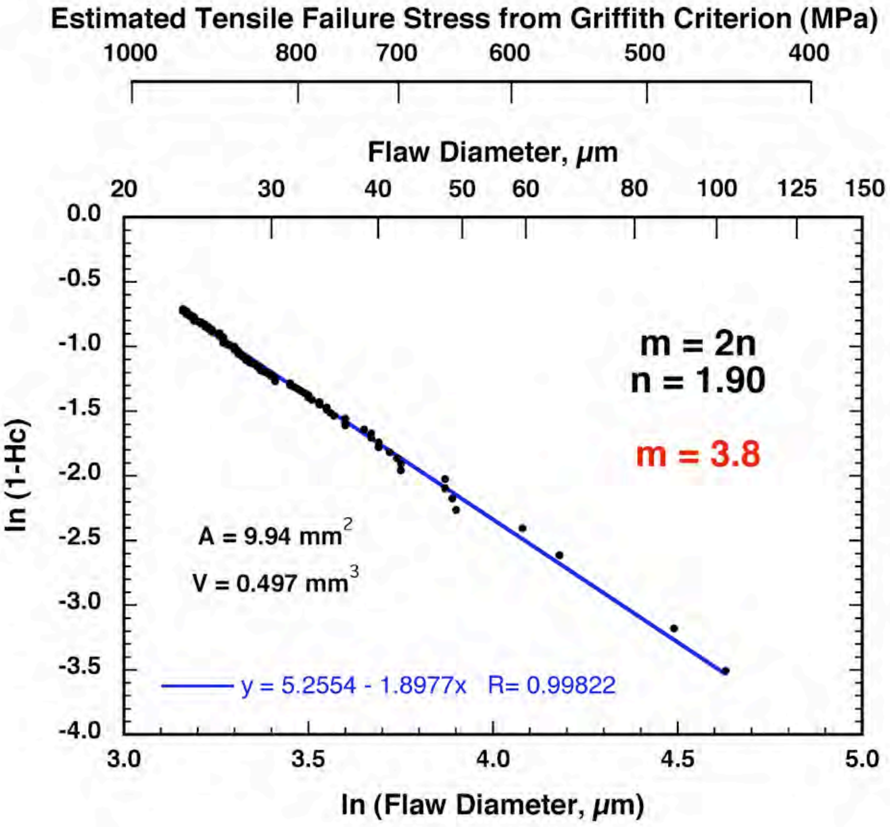

Figure 7.5. Predicted Weibull modulus from the quantification of the largest flaws after Jayatilaka and Trustrum [7.1].

Summarizing Section 7.3

- The intrinsic flaw sizes that limit strength in SiC-N are carbon inclusions. Their size can be upwards of an order of magnitude larger than the mean SiC grain size.
- The combination of transmitted light optical microscopy of thin sections of ceramics (after Nagaoka University work) and the method of Jayatilaka is a very useful way to quantify flaw populations in SiC.

7.4. Effective Size Analysis of the Diametral Compression (Brazil) Test Specimen

This subtask considered the finite element analysis (FEA) simulation and Weibull effective size analysis for the diametral compression (DC) or Brazil specimen loaded with three different push-rod geometries. Details of this examination can be found in Ref. [7.15]. Those three geometries were a flat push rod, a push rod whose radius of curvature is larger than that for the DC specimen, and a push rod whose radius of curvature matches that of the DC specimen. Such established effective size analysis recognizes that the tensile strength of structural ceramics is typically one to two orders of magnitude less than its compressive strength. Therefore, because fracture is much more apt to result from a tensile stress than a compressive one, this traditional analysis only considers the first principal tensile stress field in the mechanically loaded ceramic component for the effective size analysis.

The effective areas and effective volumes were computed as a function of Weibull modulus using commercially available integrated design and reliability software. Particular attention was devoted to the effect of mesh sensitivity and localized stress concentration. The effect of specimen width on the stress state was also investigated. The effects of push-rod geometry, the use of steel versus tungsten carbide (WC) push-rods, and considering a frictionless versus no-slip interface between push-rod and specimen on the maximum stresses, where those stresses are located, and the effective area and effective volume results are described.

Of the three push-rod geometries, it was concluded that the push rod (made from WC rather than steel) whose radius of curvature matches that of the DC specimen is the most apt to cause fracture initiation within the specimen's bulk rather than at the loading interface. Therefore, its geometry is the most likely to produce a valid diametral compression strength test. However, the DC specimen remains inefficient in terms of its area and volume efficiencies; namely, the tensile strength of only a few percent of the specimen's entire area or volume is sampled.

Summarizing Section 7.4

- Given the high probability that a valid (or invalid) test cannot be proven by ceramic fractographic practices suggest that this (quasi-static) test method and specimen is questionable for use with relatively strong structural ceramics. And if it is questionable for use for quasi-static testing of structural or armor ceramics, then its dynamic testing will likely be as questionable.

7.5. References

[7.1] A. De S. Jayatilaka and K. Trustrum, "Fracture of Brittle Materials in Uniaxial Compression," *J. Mat. Sci.*, 13:455-457 (1978).

[7.2] A. De S. Jayatilaka and V. K. N. Nanayakara, "Compression Failures in Brittle Materials: Relating Observations to a Theoretical Model," *J. Mat. Sci.*, 16:1726-1728 (1981).

[7.3] W.A. Weibull, "A Statistical Theory of the Strength of Materials," *Ingeniors Ventenskaps Akademien Handlinger*, 151:5-45 (1939).

[7.4] N. A. Weil and I. M. Daniel, "Analysis of Fracture Probabilities in Nonuniformly Stressed Brittle Materials," *J Am. Cer. Soc.*, 47:268-274 (1964).

[7.5] D. Sherman and D. G. Brandon, "The Ballistic Failure Mechanisms and Sequence in Semi-Infinite Supported Alumina Tiles," *J. Mat. Res.*, 12:1335-43 (1997).

[7.6] D. Sherman and T. Ben-Shushan, *Int. J. Impact Eng.*, "Quasi-Static Impact Damage in Confined Ceramic Tiles," 21:245-265 (1998).

[7.7] D. Sherman, "Impact Failure Mechanisms in Alumina Tiles on Finite Thickness Support and the Effect of Confinement," *Int. J. Impact Eng.*, 24:315-328 (2000).

[7.8] S. Satapathy and S. Bless, "Calculation of Penetration Resistance of Brittle Materials Using Spherical Cavity Expansion Analysis," *Mech. Mat.*, 23:323-330 (1996).

[7.9] ASTM C 1499, "Standard Test Method for Monotonic Equibiaxial Flexure Strength of Advanced Ceramics at Ambient Temperatures," Vol. 15.01, 2008, ASTM, West Conshohocken, PA.

[7.10] G. de With and H. H. M. Wagemans, "Ball-on-Ring Test Revisited," *J. Am. Cer. Soc.*, 72:1538-1541 (1989).

[7.11] K. L. Johnson, *Contact Mechanics*, 1985, Cambridge University Press, Cambridge, UK.

[7.12] ASTM C 1239, "Standard Practice for Reporting Uniaxial Strength Data and Estimating Weibull Distribution Parameters for Advanced Ceramics," Vol. 15.01, 2008, ASTM, West Conshohocken, PA.

[7.13] D. E. Grady, unpublished work.

[7.14] H. Abe, M. Naito, T. Hotta, N. Shinohara, and K. Uematsu, "Flaw Size Distribution in High-Quality Alumina," *J. Am. Cer. Soc.*, 86:1019-21 (2003).

[7.15] O. M. Jadaan and A. A. Wereszczak, "Effective Size Analysis of the Diametral Compression (Brazil) Test Specimen," ORNL-TM-2009/100, April 2009.

ACKNOWLEDGEMENTS

Research performed under Work For Others funded by U.S. Army Tank-Automotive Research, Development and Engineering Center, under contract DE-AC-00OR22725 with UT-Battelle, LLC.

The authors wish to express sincere appreciation to D. Templeton and F. Rickert of the U.S. Army Research, Development and Engineering Command - Tank-Automotive and Armaments Command for sponsoring this work. P. Patel of the US Army Research Laboratory is thanked for his very generous supply of glass tiles. Many individuals contributed to this overall body of work as evidenced by the manuscript co-authors listed in Appendix I, but gratitude is particularly expressed to the following individuals for their technical contributions in FY09: P. Patel, D. Harper, W. Daloz, K. Johanns, M. Lance, H. -T. Lin, S. Waters, O. Jadaan, J. Swab, M. Ragan, J. LaSalvia, J. Campbell, G. Thompson, D. Grady, and G. Quinn. Lastly, the authors thank P. Blau and J. Hemrick for their review of this report and helpful comments.

APPENDIX I:
LIST OF PUBLICATIONS

This listing includes manuscripts that the Principal Investigator (Wereszczak) authored or co-authored, those were published in FY09 or are in press or in internal review (at the time of this writing), and that were fully or partially sponsored by TARDEC.

1. A. Wereszczak, D. C. Harper, C. E. Duty, and P. Patel, "Glass Strengthening via High-Intensity Plasma-Arc Heating," in press, *Journal of the American Ceramic Society*, 2009.
2. A. Wereszczak, W. L. Daloz, K. T. Strong, Jr., and O. M. Jadaan, "Effect of Indenter Elastic Modulus on Hertzian Ring Crack Initiation in Silicon Carbide," in review, *International Journal of Applied Ceramic Technology*, 2009.
3. A. Wereszczak, T. P. Kirkland, K. T. Strong, Jr., J. Campbell, J. C. LaSalvia, and H. T. Miller, "Size-Scaling of Tensile Failure Stress in Hot-Pressed SiC," in review, *International Journal of Applied Ceramic Technology*, 2009.
4. T. J. Holmquist and A. A. Wereszczak, "Using Hertzian Indentation to Understand the Strength and Ballistic Resistance of Silicon Carbide," in review, *International Journal of Applied Ceramic Technology*, 2009.
5. R. L. Yeckley, J. C. LaSalvia, and A. A. Wereszczak, "Development of SiAlON Armor Ceramics," in review, *International Journal of Applied Ceramic Technology*, 2009.
6. O. M. Jadaan, A. A. Wereszczak, K. E. Johanns, and W. L. Daloz, "Weibull Effective Area for Hertzian Ring Crack Initiation Stress," in review, *International Journal of Applied Ceramic Technology*, 2009.
7. A. Wereszczak, T. P. Kirkland, K. T. Strong, Jr., O. M. Jadaan, and G. A. Thompson, "Size-Scaling of Tensile Failure Stress in Boron Carbide," accepted for publication, *Advances in Applied Ceramics*, 2009. [Invited]
8. J. J. Swab, J. Tice, A. A. Wereszczak, and R. Kraft, "Fracture Toughness of Advanced Structural Ceramics: Applying ASTM C1421," in review, *Journal of the American Ceramic Society*, 2009.
9. A. Wereszczak, K. E. Johanns, and O. M. Jadaan, "Hertzian Ring Crack Initiation in Hot-Pressed Silicon Carbide," *Journal of the American Ceramic Society*, 92:1788-1796 (2009).
10. X. Nie, W. C. Chen, A. A. Wereszczak, and D. T. Templeton, "Effect of Loading Rate and Surface Conditions on Flexural Strength of Borosilicate Glass," *Journal of the American Ceramic Society*, 92:1287-95 (2009).
11. K. T. Strong, Jr., A. A. Wereszczak, W. L. Daloz, and O. M. Jadaan, "Indenter Elastic Modulus and Hertzian Ring Crack Initiation," *Ceramic Engineering and Science Proceedings*, [5] 30:83-90 (2009).
12. ORNL/TM-2009/100 Report: "Effective Size Analysis of the Diametral Compression (Brazil) Test Specimen," O. M. Jadaan and A. A. Wereszczak, April 2009.

APPENDIX II: LIST OF PRESENTATIONS

This listing includes presentations that the Principal Investigator (Wereszczak) gave in FY09 and that were fully or partially sponsored by TARDEC.

1. "Strengthening of Soda-Lime Silicate Glass Using High-Intensity Plasma-Arc Heating," *Corning Glass*, Corning, NY, 21 Jul 2009.

2. "Flaws and Mechanical Response in Polycrystalline Armor Ceramics," *US Army TARDEC Transparent Armor Materials Working Group Meeting,* University of Mississippi, Oxford, MS, 07 May 2009.

3. "Quasi-Static Characterization and Analysis," *US Army TARDEC Transparent Armor Materials Working Group Meeting*, University of Mississippi, Oxford, MS, 06 May 2009.

4. "Hertzian Indentation of Si_3N_4 Using Si_3N_4 Balls," 5th Annual Fulrath Symposium, *2009 International Ceramics Exhibition*, Tokyo, Japan, 08 Apr 2009. [Invited and obligation as part of receiving Fulrath Award]

5. "Hertzian Indentation of Si_3N_4 Using Si_3N_4 Balls," *Nagaoka University of Technology*, Nagaoka, Japan, 07 Apr 2009.

6. "Strength of Bismuth Telluride," *33rd International Conference on Advanced Ceramics and Composites*, Daytona Beach, FL, 22 Jan 2009.

7. "Hertzian Indentation With Si_3N_4 Balls on a Flat Si_3N_4 Target," *33rd International Conference on Advanced Ceramics and Composites*, Daytona Beach, FL, 20 Jan 2009.

8. "C-Sphere Flexure Strength of Bearing-Grade Silicon Nitride Balls," MST2008, Pittsburgh, PA, 07 Oct 2008. [Invited and obligation as part of receiving Fulrath Award]

APPENDIX III:
LIST OF INVENTION DISCLOSURES

This listing includes invention disclosures that the Principal Investigator (Wereszczak) submitted to ORNL in FY09 and that were fully sponsored by TARDEC.

1. *Permanent Multifunctional Patterning of Glass Surfaces Using Infrared Heating*, A. A. Wereszczak, and D. C. Harper, Invention Disclosure Number 200902260, DOE S-115,296, May 2009.

2. *Surface and Edge Strengthening of Glass Using Arc Lamp Heating*, A. A. Wereszczak, and D. C. Harper, Invention Disclosure Number 200902256, DOE S-115,292, May 2009.

APPENDIX IV:
LIST OF RELATED AWARDS AND PROFESSIONAL ACTIVITIES

This listing includes an award given to the Principal Investigator (Wereszczak) and professional activities whose partial sponsorship of TARDEC enabled in FY09.

- Richard M. Fulrath Award Winner, American Ceramic Society, 2008.

- Chair, Engineering Ceramics Division, American Ceramic Society, 2008-2009.

- Symposium Co-Organizer, *Ceramic Armor, 33rd International Conference on Advanced Ceramics and Composites*, Daytona Beach, FL, January 18-23, 2009.

- Guest Associate Editor, special edition on Ceramic Armor, *International Journal of Applied Ceramic Technology*, to be published in 2010.